Title
Impedance Spectroscopy for Surface and Fracture Wounds: Sensor Development and Clinical Application

Author
Lin, Monica Christine

Publication Date
2018

Peer reviewed|Thesis/dissertation

Impedance Spectroscopy for Surface and Fracture Wounds:
Sensor Development and Clinical Application

by

Monica Christine Lin

DISSERTATION

Submitted in partial satisfaction of the requirements for the degree of

DOCTOR OF PHILOSOPHY

in

Bioengineering

in the

GRADUATE DIVISION

of the

UNIVERSITY OF CALIFORNIA, SAN FRANCISCO

AND

UNIVERSITY OF CALIFORNIA, BERKELEY

Approved:

[redacted]

.....

Committee in Charge

Acknowledgements

There are so many people who supported me through this journey, and I feel so fortunate to have had the opportunity to be mentored by and work with so many talented individuals.

Firstly, I must acknowledge Professor Michel Maharbiz, who served as my research mentor and dissertation committee chair. His encouragement, both in avenues of research and of professional development, have made a huge impact on not only the technical work presented here, but also on my personal growth as a scientist and engineer. I cannot thank him enough. I also want to recognize the other two members of my dissertation committee – Professors Jeffrey Lotz and Ralph Marcucio. I did a research rotation with Professor Lotz my first year of graduate school, and he continued to play an important role in my work in the field of orthopedics. Professor Marcucio has been a wonderful mentor, serving as a leader of the research group at the Orthopaedic Trauma Institute in San Francisco General Hospital, which I worked very closely with.

I want to thank all the members of the Maharbiz Lab, both former and current. Each of them has played an important part in my graduate school experience, and I am so grateful for all the time we shared together. Many thanks to: Amy Liao, who I shared much of this journey with; David Piech, Camilo Diaz-Botia, Travis Massey, Konlin Shen, and Tom Zajdel, who gave me advice at all hours of the day and helped me with Nanolab procedures; Bochao Lu, Alyssa Zhou, Arda Ozilgen, Oliver Chen, KyoungTae Lee, and Mauricio Bustamante, who were always there with a friendly smile; Maruthi Yogeesh, Wei Li, and Soner Sonmezoglu, who's experience was much appreciated; Daniel Cohen, who helped me get my footing when I first joined the group; DJ Seo, Joshua van Kleef, Veda Krishnan, Peter Ledochowitsch, Brian Pepin, and Stefanie Garcia, who have been sorely missed since they graduated; and Richard Lossing, Kim Ly, and Huo Chao Kuan, who play vital roles in the Berkeley Sensor and Actuator Center (BSAC) and Swarm Lab at

Berkeley. I also want to thank the many undergraduates who worked with me, including Daniel Grubb, Joshua Chen, Kaylee Mann, David Ni, Eleane Jao, Dilveen Goraya, Reia Cho, and others; they all made important contributions to the work discussed in this thesis.

I am so grateful to the Orthopaedic Trauma Institute at the San Francisco General Hospital (UCSF). The research group there has been my second lab family, and they have graciously welcomed me. The second half of my dissertation is based on a collaboration with Professor Chelsea Bahney, Professor Safa Herfat, and Dr. Meir Marmor. They have been the most incredible collaborators, and I feel so lucky to have worked with these dedicated scientists and clinicians. Many thanks to: Frank Yang and Diane Hu, who helped guide my project; Sarah Almubarak, Sarah Wong, Sloane Brazina, Tiffany Shao, and Risa Takenaka, who came to my rescue whenever I needed help with mouse surgeries; Alexis Lainoff, Daniel Clark, Kevin Rivera, Heather Richbourg, and Jiun Chang, fun labmates with whom I could always share a laugh; Yotvat Marmor, Marta Linde-Medina, JJ Moon, Jaselle Perry, and Donna Poscablo, who helped train me on a number of technical procedures; and Gina Baldoza and Anna Lissa Wi, who's tireless efforts keep the lab running.

I had the great fortune of working with a number of great collaborators, and would like to acknowledge their contributions to the work in this thesis. Sarah Swisher in Professor Vivek Subramanian's group was a senior graduate student and unbelievable mentor to me in my early years of graduate school. Sarah as well as Yasser Khan and Felippe Pavinatto in Professor Ana Claudia Aria's group were critical to various engineering and materials aspects of the pressure ulcer research. Dr. David Young, Dr. Elisabeth Leeflang, Dr. Lauren Ritz, and Dr. Claire Graves provided important clinician perspectives and helped conduct our animal and clinical studies. Professor Shuvo Roy, Dr. Michael Harrison, Elizabeth Gress, and Dillon Kwiat at UCSF Surgical Innovations also frequently offered support and expertise. Christina Bulman and Chelsea Bidlow

in Professor Judy Sakanari's group and Ndi Emmanuel in Professor Fidelis Cho-Ngwa's group were integral to the onchocerciasis work, and I am so grateful to them for giving me the opportunity to conduct meaningful research in Cameroon. Alfred Li at the UCSF CCMBM Bone Imaging Research Core helped me take X-rays and analyze μCT scans for my work in fracture monitoring, and Dezba Coughlin worked tirelessly to support my research through the Center for Disruptive Musculoskeletal Innovations (CDMI). I am also grateful for the funding I received from the National Science Foundation through the Graduate Research Fellowship Program.

I want to thank a number of other individuals in the UC Berkeley – UCSF Graduate Program in Bioengineering. Mark Sena in Professor Jeffrey Lotz's group and Janine Lupo in Professor Sarah Nelson's group were my mentors during my first year research rotations. I am grateful to my qualifying exam committee – Professors Steve Conolly, Shuvo Roy, and Rich Schneider – who helped me craft a research proposal and made sure I had the tools to tackle it. The graduate program would not run without administrators Kristin Olson and SarahJane Taylor, and I really appreciate all the work they do for us, often behind-the-scenes. I also want to thank Professors Tamara Alliston and John Dueber, who were chair and co-chair of the Executive Committee when I was involved with program leadership, and Professor Chris Diederich, who was the Retreat Committee faculty member when I was on the planning team; I look up to them as examples of excellent leaders. To my fellow classmates in the Bioengineering Association of STudents (BEAST), I am so grateful for your friendship and cherish so many great memories from our time together.

Finally, I want to extend my greatest thanks and appreciation to my family. My mom and dad have been my support system all my life, and I am so grateful for the education they provided me. My younger brother and I have shared so many of life's experiences together, and he's been by my side through it all. I would not be where I am today without the love and support of my family.

Impedance Spectroscopy for Surface and Fracture Wounds:
Sensor Development and Clinical Application

Monica Christine Lin

Abstract

Wearable sensors and instrumented implants have wide-ranging clinical applications, and their continued development in recent years has led to advances in personalized healthcare. Innovations in electronics and trends in mobile health are extending the capabilities of traditional medical practice. For a number of clinical conditions, there remains a lack of standardized methods for assessing patients, with physicians often relying on subjective physical examinations that can differ depending on medical training and experience. The work in this thesis focuses on developing objective tools using electrical impedance spectroscopy (EIS) to monitor surface and fracture wounds. EIS measures the frequency-dependent opposition to the flow of electrical current, and has been used to quantitatively characterize cellular changes. This work begins by examining pressure ulcers, tissue damage caused by prolonged pressure on the skin, which are commonly analyzed using photographs and ruler measurements. Prevention efforts involve nursing staff repositioning patients every few hours to relieve pressure on a particular area, which is highly time and labor intensive. A "smart bandage" was designed to non-invasively detect and monitor pressure ulcers by identifying changes in tissue health. By utilizing EIS over a flexible electrode array, visually intuitive maps were produced to determine areas with tissue damage and areas at risk for further injury. To extend this technology to deep tissue injuries, this work also details development of an instrumented implant to monitor bone fracture healing. X-ray radiographs are the most common method of assessing fracture repair, but are only useful at later stages because they rely on mineralization of tissue. Microscale sensors were designed and built to locally

measure healing fractures in rodent models, and EIS was employed to robustly track longitudinal differences in healing trends. Advancements in miniaturized and flexible electronics have enabled these kinds of physiological monitoring devices, which can guide clinical decision-making and facilitate early intervention. By instrumenting items like bandages and fracture fixation implants already widely used in hospital settings, this work demonstrates that EIS technology can be integrated into current health management strategies with minimal disruption to clinical workflows.

Table of Contents

List of Tables

List of Figures

Chapter 1: Introduction

1.1 Wearable sensors and instrumented implants for clinical applications

Wearable and implanted sensors have expanded the field of digital health through various biomedical applications. They have been used to monitor, track, and record clinically-relevant information about patients to improve their health. Innovations in mobile and electronic healthcare are augmenting the capabilities of traditional physiological monitoring devices in many branches of medicine, including cardiopulmonary, vascular, endocrine, neurology, nephrology, dermatology, rehabilitation, orthopedic, etc[1,2]. These smart sensors may be used both for preventative measures as well as to follow the progression of disease and aid in treatment decisions. They have not only led to advances in personalized healthcare, but studies have also shown that providing patients with objective feedback about their health can improve patient outcomes as they are more likely to comply with clinical recommendations[1]. Furthermore, smart sensors allow individuals to participate more actively in their healthcare, even remotely in non-clinical settings. Recent developments in engineering are responsible for better network software, system architecture, hardware fabrication, power management, signal processing, cloud computing, machine learning and security[2]. This has led to a decrease in costs, as packaging and fabrication methods have achieved production scale and communication technology has improved to provide much higher rates of data transfer[3]. This has expanded the scope of medical conditions that can benefit from advanced physiological measurements.

The first wireless wearable devices were developed using accelerometers, gyroscopes, and pressure-sensitive textiles combined with Internet-based communications. Recent progress has seen these sensors become smaller and more flexible, enabling them to be woven into clothing or

built on ultrathin substrates for placement on the body.[2] Many wearable devices, particularly those for commercial use, involve accelerometers. Triaxial accelerometers can detect movement and posture, as well as identify physical activities to evaluate mobility status of patients[4]. Gyroscopes can also be used in conjunction with accelerometers to increase accuracy of these types of measurements[5]. Wristbands are a common form factor that can include sensors to detect seizures for epileptic patients[6], or collect photoplethysmograms to monitor blood pressure for hypertension patients[7]. Noninvasive glucose sensors have also been developed to diagnose and control diabetes[8,9]. In addition, wearable sensors can enable physiological monitoring of heart rate, respiratory rate, blood oxygen saturation, and muscle activity[10]. These can have applications in areas like continual rehabilitation, as patients are no longer confined to a hospital setting. Flexible sensors have further eased compatibility of these electronic systems with daily life. They allow for non-invasive devices to be adhered to the body or integrated into clothing. This long-term contact enables a number of physical and electrical measurements such as breathing rate, skin temperature, electrocardiography, electroencephalography, and electromyography to be collected and analyzed as trends over time[11]. Measurements like these not only provide basic vital signs monitoring and analysis of activity levels, but can also allow for non-invasive diagnosis and monitoring of surface wounds.

While wearable sensors have become largely ubiquitous due to lower regulatory hurdles, implantable devices are on the rise due to improvements in micro-electro-mechanical systems (MEMS) technology, wireless communications, and digital electronics[12]. Cardiac pacemakers were one of the first fully implantable health devices. They were created in the 1960s, and implantable devices since then have improved to incorporate programmable circuitry and better tissue integration to promote device longevity.[3] Implantable sensors most commonly measure

parameters such as force, torque, pressure, and temperature[13], and can enhance the function of existing implants by providing quantitative data. For example, implantable strain sensors have been developed that can attach to commercial internal fixation bone plates that are used to fix tibia fractures[14,15]. Implantable sensors have also been integrated into cardiac resynchronization therapy devices, which can continuously monitor the status of heart failure patients[16]. For tissue engineers, real-time measurements of strain, pressure, pH, temperature, oxygen tension, and specific biomarkers would significantly improve evaluation of mechanisms of healing or lack of healing. These represent important environmental cues that may regulate cell migration, differentiation, proliferation, and apoptosis[17]. For the field of regenerative medicine and others, integration with native tissue is a critical factor. Batteryless devices have been developed that integrate various sensors in an implanted module paired with external readers to monitor conditions like gastroesophageal reflux disease[18] and heart failure[19]. Ongoing work to miniaturize electronics and reduce biocompatibility issues has especially driven the use of sensors to monitor deep injuries of internal physiological systems.

To develop smart sensors based on clinical needs, collaboration between clinicians and engineers is critical. In a number of medical disciplines, there remains a lack of standardized methods for diagnosing patients and assessing treatment outcomes. Traditionally, physicians have often relied on subjective physical examinations and qualitative patient questionnaires, which can result in an incomplete and potentially inaccurate picture of a patient's status. Advances in engineering have facilitated gathering of a whole host of new information, and interdisciplinary teams can define unmet clinical needs and address them in a targeted way. Smart sensors can not only address some of the challenges in the clinic by providing objective, quantitative information to patients and their

physicians, but they can enable longitudinal tracking at much higher temporal resolution than conventionally available.

1.2 Impedance spectroscopy

Electrical impedance spectroscopy (EIS) measures the electrical properties of a material as a function of frequency. It describes the passive ability to oppose (or impede) the flow of electrical current, and combines resistive, capacitive, and inductive components. Tissue can be modeled as a combination of electrical components. Plasma cell membranes act as capacitors, with their phospholipids giving them dielectric characteristics. Intracellular and extracellular environments consist of conductive liquids, or electrolytic solutions.[20] Tissue may thus be considered primarily a conductor or a dielectric, depending on the frequency (Fig. 1.1). At lower frequencies, most tissues are predominantly electrolytic conductors. At higher frequencies, dielectric properties that reflect storage of electrical energy may dominate.[21] Complex impedance Z can be expressed in polar form as

$$Z = |Z|e^{j\theta} \qquad (1.1)$$

with magnitude $|Z|$ and phase angle θ, or in Cartesian form as

$$Z = R + jX \qquad (1.2)$$

with resistance R and reactance X.

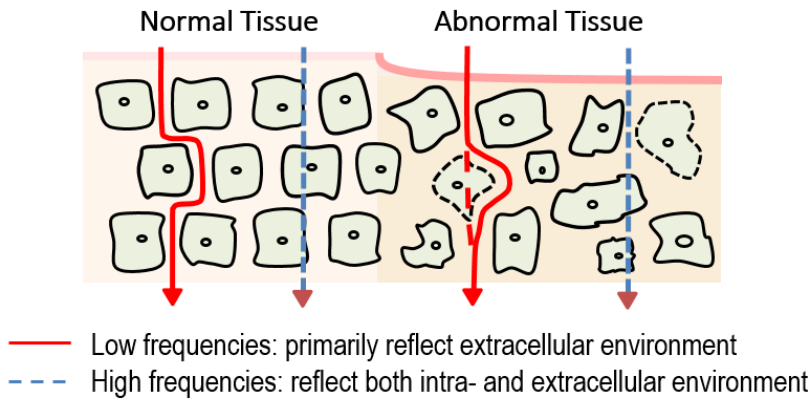

Figure 1.1 – Diagram of signal traveling through normal and abnormal tissue
In an impedance measurement, low frequency current primarily reflects the extracellular environment as the cell membrane appears highly resistive. High frequency current will tend to reflect both intra- and extracellular environment as the cell membrane drops in impedance.

Electrical measurements have been used in clinical applications starting from the late 1800s. Electrocardiograms were first recorded from the heart in 1887[22] and brought into clinical use in 1905[23]. Electroencephalograms recorded bioelectric signals from the brain beginning in 1940, and pacemakers and defibrillators were introduced in the 1960s.[21,22,24] Since then, a number of studies have measured dielectric properties of cells during apoptosis and taken real-time measurements of biomass[25–27]. EIS has been used to characterize different biological tissues[28–31], and more recently has been applied to specific clinical applications. Gastrointestinal, musculoskeletal, respiratory, and cardiovascular conditions have been examined using EIS to increase understanding of a variety of afflictions[20,32]. In particular, numerous studies have explored the use of EIS to perform early detection of cancer in different organs, including skin, breast, cervix, esophagus, bladder, and colon[20,33–35].

Impedance can be measured with 2, 3, or 4 electrodes. In a 4-point measurement, one electrode pair carries the current while the other pair picks up the corresponding potential difference[21]. This separates the main current-carrying wires from those used to measure voltage, eliminating possible inaccuracy due to resistance of the leads. A 3-point measurement reduces the number of wires

needed and can be comparable in accuracy if all 3 measurement wires are similar. However, in the case of measuring tissue, 4-point measurements are not necessarily reliable because the electrode-to-tissue contact is not ideal. An accurate 3- or 4- point measurement relies on all electrodes making excellent electrical contact with the device under test (DUT), and is typically used in industrial applications. For clinical applications explored in this thesis, 2-point measurements were found to produce less variation as they allowed for more reliable regulation of the signal output level.

1.3 Dissertation outline

This dissertation describes work to design and build smart sensors and instrumented implants to address important medical problems. The research presented focuses on the utilization of impedance spectroscopy to detect and monitor surface and fracture wounds, particularly the development of sensors and their clinical applications. By working closely with both engineers and clinicians, sensors were successfully fabricated and tested in various *ex vivo* and *in vivo* models, informing continued development towards clinical translation.

In Chapter 2, a flexible electrode array is demonstrated as an effective way to non-invasively detect pressure ulcers. This chapter covers the development of the array, measurement hardware and software, as well as analysis algorithms. Results describe the observed outcomes of a pressure-induced injury model in rats, and establish the ability of impedance to identify tissue damage *in vivo*. Chapter 3 describes the use of the electrode array in Chapter 2 applied to a clinical trial of human patients, detailing optimization for clinical use and early results from the first five patients. Additional applications are also covered at the end of this chapter, including adaptation of this device to perform non-invasive diagnosis of onchocerciasis (a parasitic disease in sub-Saharan Africa). Next, this thesis examines the use of EIS to develop an instrumented implant. Chapter 4

explores impedance as a method to monitor bone fracture healing, highlighting the ability of this technology to distinguish isolated tissues dominant in fracture healing. An *ex vivo* mouse study shows that impedance correlates significantly to tissue compositions of heterogeneous fracture calluses. In Chapter 5, impedance spectroscopy technology is integrated into external fixators and bone plates. These smart implants are used to monitor fracture repair longitudinally in individual mice *in vivo*, and results are compared with traditional methods of assessment.

1.4 References

1. Appelboom, G. *et al.* Smart wearable body sensors for patient self-assessment and monitoring. *Arch. Public Health* **72,** 28 (2014).

2. Dobkin, B. H. & Dorsch, A. The Promise of mHealth: Daily Activity Monitoring and Outcome Assessments by Wearable Sensors. *Neurorehabil. Neural Repair* **25,** 788–798 (2011).

3. Koydemir, H. C. & Ozcan, A. Wearable and Implantable Sensors for Biomedical Applications. *Annu. Rev. Anal. Chem.* **11,** 127–146 (2018).

4. Yang, C.-C. & Hsu, Y.-L. Development of a Wearable Motion Detector for Telemonitoring and Real-Time Identification of Physical Activity. *Telemed. E-Health* **15,** 62–72 (2009).

5. Luinge, H. J. & Veltink, P. H. Measuring orientation of human body segments using miniature gyroscopes and accelerometers. *Med. Biol. Eng. Comput.* **43,** 273–282 (2005).

6. Lockman, J., Fisher, R. S. & Olson, D. M. Detection of seizure-like movements using a wrist accelerometer. *Epilepsy Behav.* **20,** 638–641 (2011).

7. Lin, H. *et al.* Noninvasive and Continuous Blood Pressure Monitoring Using Wearable Body Sensor Networks. *IEEE Intell. Syst.* **30,** 1–1 (2015).

8. Zhang, J., Hodge, W., Hutnick, C. & Wang, X. Noninvasive Diagnostic Devices for Diabetes through Measuring Tear Glucose. *J. Diabetes Sci. Technol.* **5,** 166–172 (2011).

9. Zanon, M. *et al.* Non-invasive continuous glucose monitoring: improved accuracy of point and trend estimates of the Multisensor system. *Med. Biol. Eng. Comput.* **50,** 1047–1057 (2012).

10. Patel, S., Park, H., Bonato, P., Chan, L. & Rodgers, M. A review of wearable sensors and systems with application in rehabilitation. *J. NeuroEngineering Rehabil.* **9,** 21 (2012).

11. Rodgers, M. M., Pai, V. M. & Conroy, R. S. Recent Advances in Wearable Sensors for Health Monitoring. *IEEE Sens. J.* **15,** 3119–3126 (2015).

12. Darwish, A. & Hassanien, A. E. Wearable and Implantable Wireless Sensor Network Solutions for Healthcare Monitoring. *Sensors* **11,** 5561–5595 (2011).

13. Implantable Sensors Make Medical Implants Smarter. Available at: https://www.asme.org/engineering-topics/articles/bioengineering/implantable-sensors-make-medical-implants-smarter. (Accessed: 17th August 2018)

14. Pelham, H. *et al.* Implantable strain sensor to monitor fracture healing with standard radiography. *Sci. Rep.* **7,** 1489 (2017).

15. Wachs, R. A. *et al.* Elementary Implantable Force Sensor. *Adv. Biosens. Bioelectron.* **2,** (2013).

16. Shasha Liu, P. & Tse, H.-F. Implantable sensors for heart failure monitoring. *J. Arrhythmia* **29,** 314–319 (2013).

17. Klosterhoff, B. S. *et al.* Implantable Sensors for Regenerative Medicine. *J. Biomech. Eng.* **139,** 0210091–02100911 (2017).

18. Cao, H. *et al.* An implantable, batteryless, and wireless capsule with integrated impedance and pH sensors for gastroesophageal reflux monitoring. *IEEE Trans. Biomed. Eng.* **59,** 3131–3139 (2012).

19. Troughton, R. W. *et al.* Direct Left Atrial Pressure Monitoring in Severe Heart Failure: Long-Term Sensor Performance. *J Cardiovasc. Transl. Res.* **4,** 3–13 (2011).

20. González-Correa, C.-A. Clinical Applications of Electrical Impedance Spectroscopy. in *Bioimpedance in Biomedical Applications and Research* 187–218 (Springer, Cham, 2018). doi:10.1007/978-3-319-74388-2_10

21. S. Grimnes & O.G. Martinsen. *Bioimpedance and Bioelectricity Basics*. (Elsevier, 2015). doi:10.1016/C2012-0-06951-7

22. Sykes, A. H. A D Waller and the electrocardiogram, 1887. *Br. Med. J. Clin. Res. Ed* **294,** 1396–1398 (1987).

23. Aquilina, O. A brief history of cardiac pacing. *Images Paediatr. Cardiol.* **8,** 17–81 (2006).

24. Williams, D. The Electro-Encephalogram in Acute Head Injuries. *J. Neurol. Neurosurg. Psychiatry* **4,** 107–130 (1941).

25. B. Kell, D., Markx, G. H., Davey, C. L. & Todd, R. W. Real-time monitoring of cellular biomass: Methods and applications. *TrAC Trends Anal. Chem.* **9,** 190–194 (1990).

26. Markx, G. H. & Davey, C. L. The dielectric properties of biological cells at radiofrequencies: applications in biotechnology. *Enzyme Microb. Technol.* **25,** 161–171 (1999).

27. Patel, P. & Markx, G. H. Dielectric measurement of cell death. *Enzyme Microb. Technol.* **43,** 463–470 (2008).

28. Stoy, R. D., Foster, K. R. & Schwan, H. P. Dielectric properties of mammalian tissues from 0.1 to 100 MHz; a summary of recent data. *Phys. Med. Biol.* **27,** 501 (1982).

29. Jongschaap, H., Wytch, R., Hutchison, J. & Kulkarni, V. Electrical impedance tomography: a review of current literature. *Eur. J. Radiol.* **18,** 165–174 (1994).

30. Dean, D. A., Ramanathan, T., Machado, D. & Sundararajan, R. Electrical impedance spectroscopy study of biological tissues. *J. Electrost.* **66,** 165–177 (2008).

31. Gabriel, S., Lau, R. & Gabriel, C. The dielectric properties of biological tissues: II. Measurements in the frequency range 10 Hz to 20 GHz. *Phys Med Biol* **41,** 2251–2269 (1996).

32. Fors, H., Gelander, L., Bjarnason, R., Albertsson-Wikland, K. & Bosaeus, I. Body composition, as assessed by bioelectrical impedance spectroscopy and dual-energy X-ray absorptiometry, in a healthy paediatric population. *Acta Paediatr.* **91,** 755–760 (2002).

33. Turgunova, N. *et al.* Bioimpedance spectroscopy for clinical assessment of tissues and the irradiated cancer tumors. in *2012 7th International Forum on Strategic Technology (IFOST)* 1–4 (2012). doi:10.1109/IFOST.2012.6357805

34. Da Silva, J. E., De Sá, J. M. & Jossinet, J. Classification of breast tissue by electrical impedance spectroscopy. *Med. Biol. Eng. Comput.* **38,** 26–30 (2000).

35. Murdoch, C. *et al.* Use of electrical impedance spectroscopy to detect malignant and potentially malignant oral lesions. *Int. J. Nanomedicine* **9,** 4521–4532 (2014).

Chapter 2: Flexible electrode array for detection of pressure ulcers *in vivo*

This chapter is adapted from the following journal article with permission from:

Sarah L. Swisher, Monica C. Lin*, Amy Liao*, Elisabeth J. Leeflang, Yasser Khan, Felippe J. Pavinatto, Kaylee Mann, Agne Naujokas, David Young, Shuvo Roy, Michael R. Harrison, Ana Claudia Arias, Vivek Subramanian, Michel M. Maharbiz. Impedance sensing device enables early detection of pressure ulcers in vivo. *Nature Communications* **6,** 6575 (2015). doi: 10.1038/ncomms7575

S.L.S., M.C.L., and A.L. designed and built the control hardware. E.J.L. wrote the animal protocol, with input from M.C.L. and A.L. Y.K. and F.J.P. designed and built the printed flexible electrode arrays. K.M. designed and implemented the control software. S.L.S, M.C.L., A.L. and E.J.L. carried out the experiments. A.N. performed histological analysis. S.L.S analyzed the impedance data. D.Y., S.R., and M.R.H. contributed to the experimental design and medical analysis. A.C.A., V.S., and M.M.M. contributed to hardware design, experimental design, and data analysis. The work in this chapter was funded by the National Science Foundation under grant EFRI-1240380.

This chapter also includes content adapted from the following theses with permission from:

Sarah L. Swisher. Synthesis, Characterization, and Applications of Solution-processed Nanomaterials: From Thin-film Transistors to Flexible "Smart Bandages". (2016).

Amy Liao. Instrumenting Flexible Substrates for Clinical Diagnosis and Monitoring. (2018).

2.1 Abstract

When enough pressure is applied to a localized area of the body for an extended period of time, the resulting loss of blood flow and subsequent reperfusion to the tissue causes cell death and a

pressure ulcer develops. Preventing pressure ulcers is challenging because the combination of pressure and time that results in permanent tissue damage can vary widely between patients. Further complicating prevention efforts, the underlying tissue damage is often severe by the time a surface wound becomes visible. Currently, no method exists to detect early tissue damage and enable intervention to minimize further injury. This chapter presents a flexible, electronic device that non-invasively maps pressure-induced tissue damage, even when such damage cannot be visually observed. Measurements of impedance spectroscopy across flexible electrode arrays *in vivo* on a rat model revealed that their frequency spectra are correlated in a robust way with the state of the underlying tissue across multiple animals and wound types. These results demonstrate the feasibility of an automated, non-invasive "smart bandage" for early monitoring and diagnosis of pressure ulcers, improving patient care and outcomes.

2.2 Introduction

Chronic skin wounds place a significant burden on the healthcare economy, with an estimated $25 billion spent on treatment in the United States alone[1]. Diabetes, obesity, and elderly age are a few risk factors that increase a patient's propensity for injury. Pressure ulcers are a type of chronic wound that develops from sustained pressure on a local region, typically over bony prominences such as the back of the head, shoulders, sacrum, or heels[1-4]. The pressure causes ischemia, or loss of blood supply, which can injure the skin and result in necrosis. Subsequent reperfusion after prolonged pressure is removed can trigger further damage due to oxidative stresses. However, the amount of pressure and time required to cause damage varies between patients[1-4], depending on age, area on the body, amount of fat in the region, comorbidities, etc. This makes them difficult to predict and thus prevent in patients undergoing lengthy surgical procedures or those who are bound to wheelchairs or hospital beds, as pressure ulcers can develop in as little as 2 hours[2-4].

Currently, prevention efforts most commonly involve nursing staff visually examining high-risk areas on patients and manually repositioning them every 1-2 hours to relieve pressure[3-5]. This places an immense burden on nursing staff, and may not be the ideal frequency of turning for individual patients. For some, turning every 2 hours may be too frequent and unnecessary, instead disrupting the patient's normal activities or sleep. For others, it may not be frequent enough, producing slow but steady tissue damage. Pressure-sensitive mats or beds are available in some hospitals, but besides the high expense, they only measure instantaneous pressure. Because progressive ischemia-reperfusion cycles at a given location are what determine ulcer development, this solution is again ineffective at addressing the diversity in the patient population.

Previous studies have modeled and measured electrical changes in cells and tissue and revealed correlations between cell types and their electrical properties[6-19]. Cells can be represented by electrical components, with double-layer cell membranes separating highly ionic intra- and extracellular fluids. The cell membrane acts as a barrier to charge flow, and can be modeled as electrical capacitors or constant phase elements. The ion-rich media inside and outside the cell can be modeled as resistors. As biological structures become damaged, change in cell number, or vary in cell type, detectable changes in the impedance spectrum may occur.

By utilizing impedance spectroscopy on the skin at high-risk locations for development of pressure ulcers, tissue health can be measured directly. This chapter discusses the development of a flexible, electronic device that non-invasively maps pressure-induced tissue damage, and can detect injury that is not visually observed. Electrode arrays are fabricated and used on a skin ischemia model in rats *in vivo*, describing correlations between impedance and the state of the underlying tissue. These quantitative measurements can provide objective information to physicians about tissue health to help inform clinical decisions of care.

2.3 Methods

2.3.1 Impedance measurement system

To measure impedance of surface wounds, an impedance sensing system was designed with four major components: a flexible electrode array, a control board, an LCR meter, and a laptop (Fig. 2.1). The flexible electrode array was placed in contact with the skin of interest, and custom control hardware routed signal to the selected electrode pair. A microcontroller (ATtiny828-MU-ND, 8-bit AVR) on the control board was programmed with a specified sequence of electrode pairs, and routed test signal from the LCR meter to each pair. Electrode pairs were selected using five 32-channel multiplexors (Analog Devices ADG732BCPZ-ND). The control board was powered by four AA batteries and power was regulated by a dual +/- low noise low drop out (LDO) regulator (Linear Technologies LT3032EDE#PBF-ND). The microcontroller also triggered the LCR meter to take measurements, which were in turn recorded on a laptop. A custom graphic user interface was implemented in Python to allow for easy operation of the system. Impedance magnitude (|Z|) and phase angle (θ) were measured using a Keysight Technologies E4980AL 20Hz-1MHz Precision LCR meter. Measurements were taken at a series of frequencies from 100 Hz to 1 MHz using a 100 mV sine wave output signal.

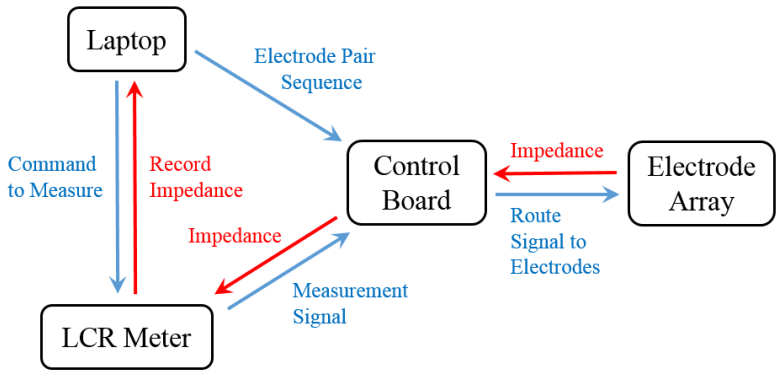

Figure 2.1 – Impedance measurement system overview
Block diagram depicting the flow of signal and information in the impedance measurement system. Commands originate from the laptop to direct impedance measurements between a specific set of electrode pairs on the array, and the impedance measurement is relayed back.

For each sample, impedance was first measured over the electrode array on an area of healthy skin to serve as a baseline reference, and then on an area where pressure-induced damage was created. To build a precise map of the measurement area, impedance measurements were taken across each nearest-neighbor pair of electrodes (72 pairs) at four frequencies: 1, 15, 50, and 100 kHz. In addition, 11 pairs scattered across the array were also selected for measurement over a set of 12 frequencies ranging from 100 Hz to 1 MHz to understand frequency response at higher resolution.

Damage to the printed gold lines or the insulation layer of the flexible electrode arrays were sometimes observed after repeated use, likely due to rubbing on the skin as well as the cleaning process for the arrays between each measurement. The arrays were tested periodically (at least once before and after wound measurements) by submerging the array in a saltwater solution of 100 g/L sodium chloride and measuring impedance between each pair. If $|Z|$ between any two electrodes measured $< 100\ \Omega$, the pair was considered 'shorted'; if $|Z|$ was greater than 50 $k\Omega$ (approximately twice the expected value), the pair was considered 'open'. All analysis first removed data from all electrode pairs that failed the saltwater test.

Impedance data was analyzed using a suite of custom MATLAB scripts, and utilized the Statistics, System Identification, and Control System toolboxes. To create visually-intuitive heat maps of the measurement area (Fig. 2.2), raw data ($|Z|$ and θ) at each frequency was filtered, averaged, interpolated between spatially neighboring measurements, and colored according to value. To extract frequency response trends, further post-processing was done to fit transfer functions to the Bode plots and compare the response curves for healthy vs. damaged tissue. 15 kHz was identified as the frequency at which the largest spread in data occurred between these two types. To create a damage threshold, impedance measurements at 15 kHz were compared between healthy and

damaged tissue across all samples. Both impedance magnitude and phase angle were considered to minimize the false positive rate and enable robust classification across all animals.

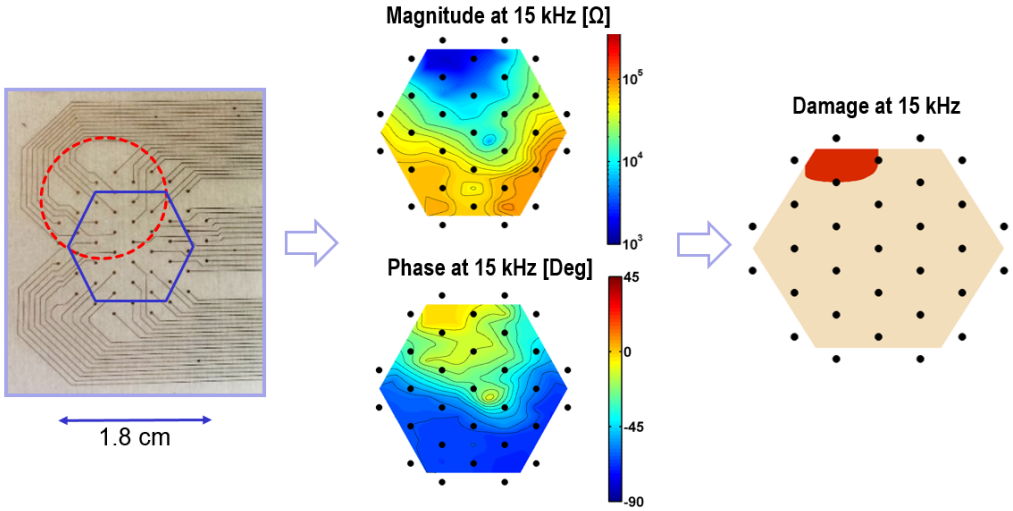

Figure 2.2 – Impedance data analysis and damage detection
Digital photographs are taken of the array placed on tissue and marked to define where the electrode measurement area (blue hexagon) is relative to the wound (red dashed circle). Impedance magnitude and phase are plotted on a color scale according to the location of the electrode pair across which each measurement was taken. A damage threshold is applied to classify tissue as wounded and plotted in red on a corresponding spatial map.

2.3.2 Ink-jet printed flexible electrode array

Flexible electrode arrays were used to allow for highly conformal contact with the skin in various areas on the body, adapting to different topographies. The fabrication of these array boards was led by Yasser Khan and Felippe Pavinatto in Ana Arias' group using an ink-jet printing process on planarized polyethylene naphthalate (PEN) substrates (DuPont) (Fig. 2.3A)[20]. A Dimatix Materials Printer (DMP-2800) used Harima gold nanopaste ink (model NPG-J) with 30 µm drop spacing to print circuit traces (0.5-1 µm thickness) and pads. Printed features were cured first with a slow ramp annealing step (30°C to 230°C with 0.7°C/min ramp) followed by a constant temperature bake (230°C for 60 min) to remove excess solvent and fuse the gold nanoparticles[21]. An amorphous fluoropolymer (Cytop CTX-809A) coating was then spun over the printed features

at 1200 rpm to achieve a 100 nm thick film as insulation. Electrode vias were then opened using oxygen plasma etching.

This flexible electrode array consisted of 55 electrodes (500 µm diameter) arranged in a hexagonal pattern designed to optimize spatial resolution across the tissue surface. Electrodes were spaced 0.1 inch apart and covered a measurement area 0.7 inches across. To ensure proper electrical contact with the skin[22], a conductive electrode gel (SignaGel, Parker Laboratories, Inc) was applied selectively to each electrode. A stencil was made by patterning a thin polydimethylsiloxane (PDMS) sheet, and a glass slide was used to carefully apply hydrogel evenly over the stencil. This resulted in a small amount of hydrogel over each electrode, which minimized contact impedance with the skin.

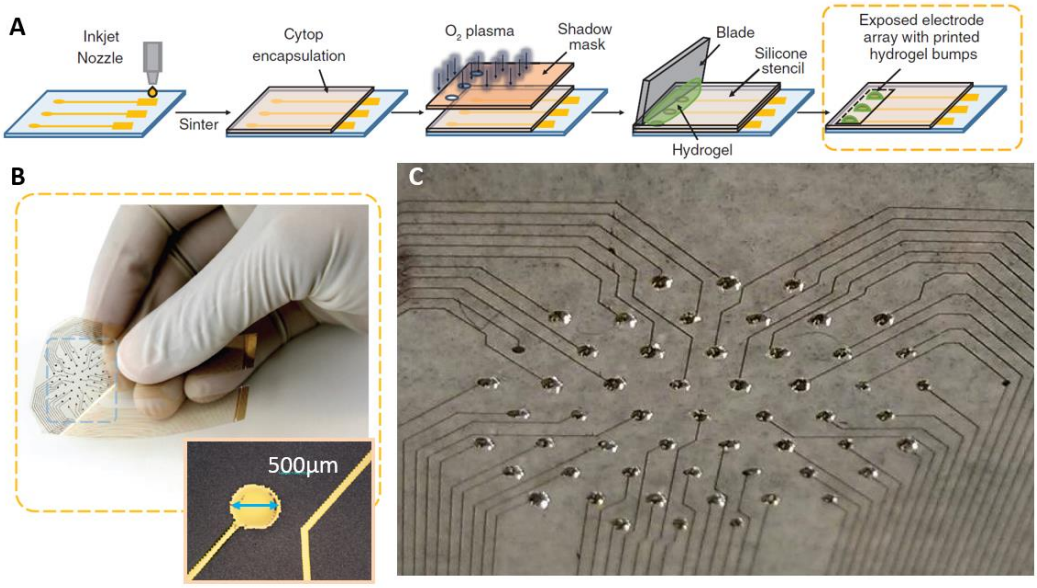

Figure 2.3 – Fabrication of flexible electrode arrays
(A) Fabrication flow for the ink-jet printed flexible electrode array. **(B)** An ink-jet printed array, with a hexagonal configuration of 55 equally-spaced gold electrodes. **(C)** Hydrogel bumps were placed selectively on each electrode to ensure adequate electrical contact with the skin.

2.3.3 Rat model for pressure ulcers

All procedures were approved by the University of California San Francisco (UCSF) Institutional Animal Care and Use Committee (IACUC). 12 wildtype Sprague-Dawley rats (male, 8 weeks old,

250-300 g) underwent a procedure to simulate pressure-induced tissue damage. Rats were first anesthetized with isoflurane mixed with oxygen, hair on the back was shaved and removed using Nair, and the area was cleaned with mild detergent and isopropyl alcohol. The skin over the back of the rat was gently tented up and placed between two round, flat magnets (12 mm diameter x 5 mm thick, 2.4 g weight, 1000 G magnetic force) over the spine (Fig. 2.4A-B)[23]. Approximately 5 mm thickness of skin was left between the magnets, creating around 50 mmHg of pressure, for either 1 hour (N=11) or 3 hours (N=9) to create minimal or severe damage, respectively. Most rats received both the 1 hour and 3 hour pressure treatments on different areas of the back after being allowed to adequately recover from the first treatment. Rats were able to return to normal activity within minutes of placing the magnets and removing the isoflurane anesthetic. After the indicated time, rats were again placed under isoflurane anesthesia and magnets were removed. Impedance measurements were taken over the wounded area immediately after magnet removal and for the subsequent 2 days, placing the rats under isoflurane anesthesia each time.

Fluorescence angiography was used to confirm that magnets created mild and severe tissue damage in our pressure ulcer model by detecting blood flow in the area of injury after the magnets were removed. Indocyanine green (ICG), a fluorescent dye, was injected into the rat tail vein, briefly binding to plasma proteins confined in the vascular system. Using a Novadaq SPY near-infrared imaging system, high blood flow appeared bright while low blood flow appeared darker. Increased fluorescence reflecting reactive hyperemia was observed immediately after relieving pressure[24,25], with reduced blood flow apparent after a few hours (Fig. 2.4C). Fluorescence angiography was also performed on days 2, 3, and 9 to track changes in perfusion over time.

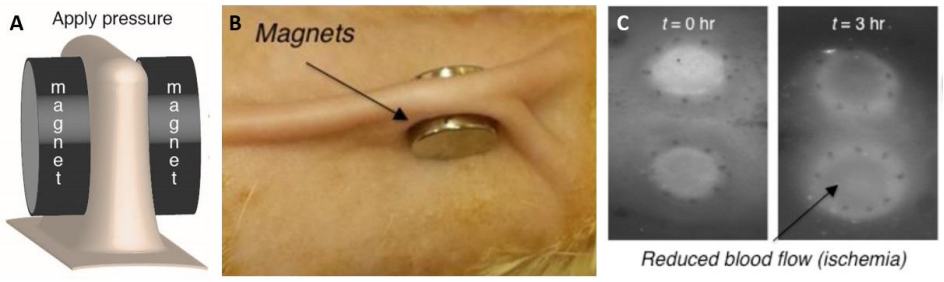

Figure 2.4 – Rat model for pressure-induced damage
(A) Diagram of skin tented between two round magnets that create a pressure wound. **(B)** Photograph of magnets clamping a piece of skin on the back of a shaved rat. **(C)** Fluorescence angiography images depicting reactive hyperemia (bright spots) immediately following magnet removal.

To ensure that electrode arrays were applied similarly to all rats, a standard protocol was set and followed (Fig. 2.5). A thin PDMS stencil was first aligned and placed on the flexible array board to allow for selective application of hydrogel to each electrode of the array. The hydrogel ensured adequate electrical contact between each electrode and the skin of the rat. After removing the stencil, the array was placed carefully on the area of the rat's back to be measured, registration marks were stained onto the skin to outline the position of the array, and the array was secured in place with a transparent Tegaderm TM dressing. Finally, a piece of Coban TM self-adherent wrap was placed around the body of the rat to apply even pressure to the array against the rat's skin.

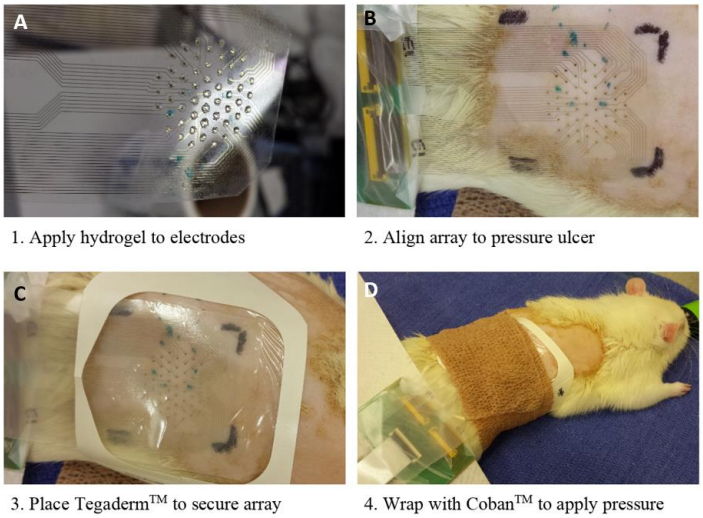

Figure 2.5 – Mounting electrode arrays to rats
(A) Hydrogel was first applied selectively to each electrode. **(B)** The array was aligned to the pressure ulcer so about half the electrode pairs were over the injury and half were over healthy skin. **(C)** A Tegaderm™ bandage was used to secure the array to the animal. **(D)** Coban™ wrap was used around the animal to apply even pressure for measurement.

2.3.4 Skin samples for histology

Rats were sacrificed the day of surgery and 1, 2, and 8 days post-injury for histology. The full thickness of skin was excised around the area of injury, immediately fixed in 10% neutral buffered formalin for 24-72 hours. Tissue was then transferred to 70% ethanol, embedded in paraffin wax, and sectioned at 5 μm thickness. Sections were stained with hematoxylin and eosin and examined for damage to cell membrane and other tissue structures.

2.4 Results

2.4.1 Rat model leads to three observed outcomes

To understand how impedance data collected on the skin reflected tissue health, fluorescence angiography, visual inspection, and histology were employed to confirm the overall and cellular state of the tissue. Fluorescence angiography provided information about perfusion in the area where the magnets were placed compared to the surrounding skin (Fig. 2.6). Immediately after removal of the magnets, both the 1 hour and 3 hour ischemia cases showed reactive hyperemia, reflected in a bright circle where the magnets had just been removed. As the tissue is being reperfused during this period, reactive oxygen species and free radicals are produced and further damage the tissue. In the 1 hour cases, after day 1, tissue perfusion between the treated area and the healthy area appeared similar, with no clear signs of increased or decreased blood flow where the magnets had been. In the 3 hour cases, after waiting 3 hours after the magnets are first removed, decreased perfusion is evident in the center of the treated area, surrounded by a ring of hyperemia. This persisted for the subsequent days, with the pressure-treated area remaining darker than the surrounding untreated skin.

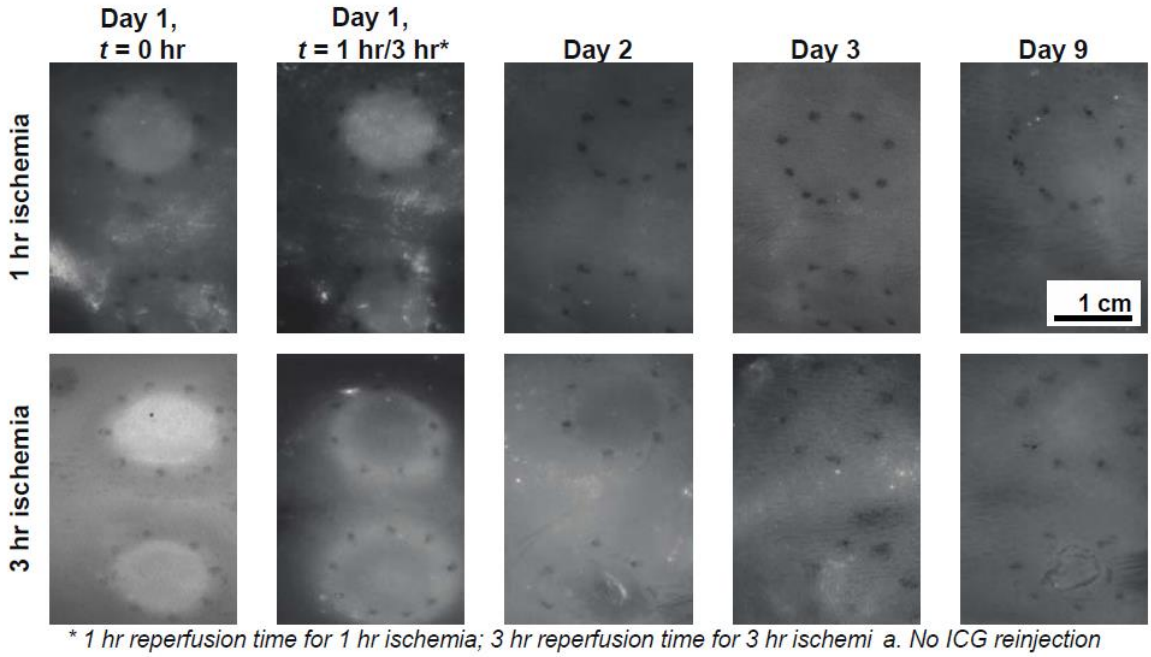

Figure 2.6 – Angiography for 1 and 3 hour ischemia cases over time

Fluorescence angiography for 1 hour (top row) and 3 hour (bottom row) treatment of magnet-induced pressure. Perfusion was measured on Day 1 immediately after magnet removal (t = 0 hr), and after reperfusion (t = 1 hr/3 hr), then measured again on days 2, 3, and 9. In rats with 1 hour ischemic injuries, increased perfusion was seen at the site of magnet application on the first day, but no difference from healthy skin was observed starting from day 2. In rats with 3 hour ischemic injuries, high levels of fluorescence again indicated increased perfusion where the magnets were. In the days following, all tissues exhibited a central area of decreased perfusion consistent with the onset of visible tissue injury.

In addition, all samples were photographed at every measurement time point and visually examined for damage. As seen in Fig. 2.7, three outcomes of the pressure ulcer model were observed. In samples that received 3 hours of pressure using the magnets, tissue damage was clear. The pressure-treated area typically experienced discoloration and often scabbing. On the other hand, samples that received 1 hour of pressure showed no visual signs of damage, with the treated skin looking very similar to the untreated area around it. Yet the tissue damage maps analyzed from impedance data demonstrate a more nuanced result. In 3 hour cases, impedance data confirmed tissue damage specifically in the region where the magnets were. These cases were considered to have suffered irreversible damage. In about half of the 1 hour cases, the impedance data did not identify any tissue damage over the measurement area, suggesting that no tissue

damage had occurred. In the remaining 1 hour cases, impedance did identify areas of tissue damage in the pressure-treated region despite a lack of visual evidence, and was labeled reversible damage as the relief of pressure led to reversal of the observed changes. To confirm the true state of the tissue, histology images were examined for biological signs of tissue damage, and results matched the outcome of the impedance data and analysis. In the 3 hour cases, histological evidence pointed to a loss of epidermis and ulceration, while there was little focal hyperkeratosis (abnormal thickening of the outer layer of skin) in the 1 hour cases with no substantial damage. In the reversible damage cases, hyperkeratosis and hypergranulosis (thickening of the stratum granulosum) were evident, indicating the beginning of tissue damage, but of much lower severity than in the irreversible case.

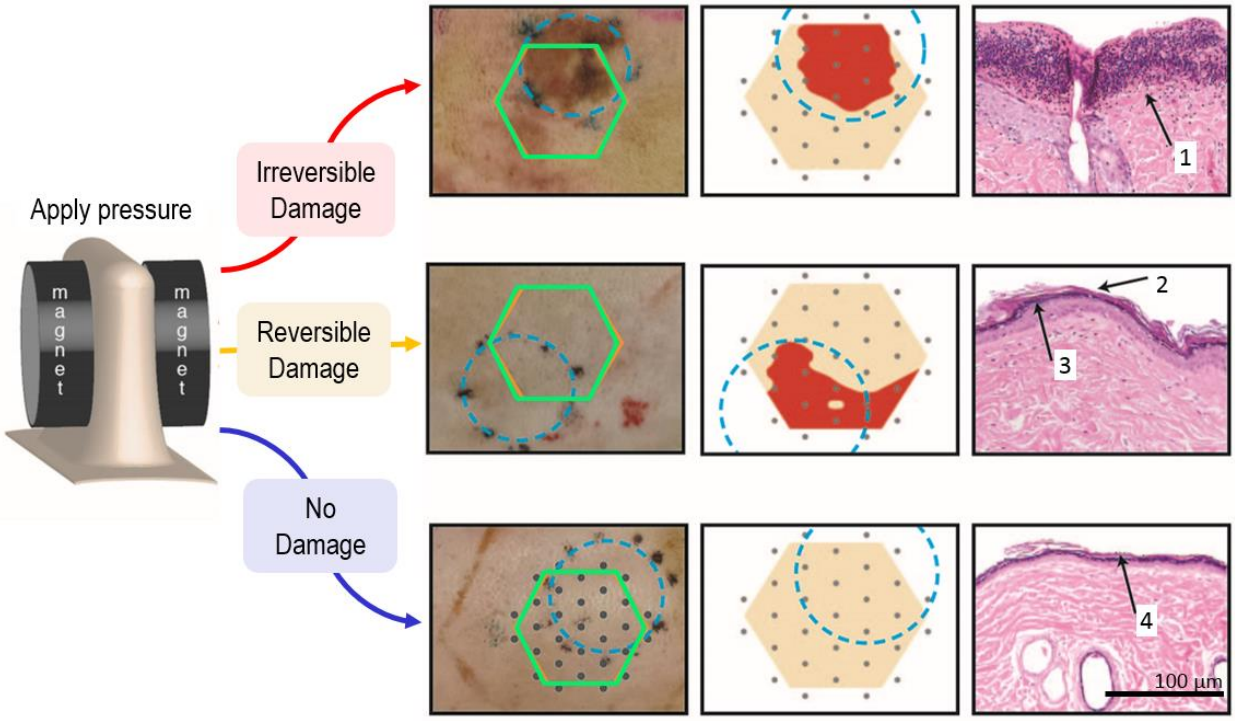

Figure 2.7 – Three observed outcomes of the rat pressure ulcer model
Magnets were used to create a pressure ulcer model on rats *in vivo*, and three outcomes were observed. Irreversible damage was visually and electrically clear, and confirmed by loss of epidermis (1) in histological images. Reversible damage was detected electrically but not visually, with histological evidence of hyperkeratosis (2) and hypergranulosis (3). No damage was observed in a number of rats, with no damage detected visually or electrically, with only focal hyperkeratosis (4) seen in histological images.

2.4.2 Electrode array identifies tissue damage

In the 3 hour ischemia group (N=9), the impedance spectra for areas developing pressure ulcers were clearly distinguishable from spectra for areas without damage by day 3 or earlier (Fig. 2.8A). Impedance magnitude was lower in wounded areas, as tissue damage often involves cell death leading to the ion-rich cell cytoplasm leaking out into the extracellular matrix. Phase angles closer to zero were observed over these same areas, consistent with the breakdown of cell membranes. By examining the impedance spectra (Fig. 2.8B), transfer functions can be fit to the frequency response curves, and parameters like poles and zeroes can be extracted. The dominant pole for wounded tissue was identified at a lower frequency than that of healthy tissue. By comparing data across all samples, a threshold was identified to limit inaccurate classification. Electrode pairs with $|Z| < 6\ k\Omega$ and $-30° \leq \theta \leq -10°$ at 15 kHz were labeled as damaged tissue. The phase threshold in particular helped limit animal-to-animal skin impedance variation, improving tissue classification. Results shown in Fig. 2.8A-B are for a single rat, but similar results were observed across all animals in this study. Repeatability across wounds on many animals was determined by combining all electrode pairs into two groups: pairs that fell in the magnet region, and pairs outside of it. In the 3 hour group especially, the reduction in impedance magnitude and less negative phase angle is clear.

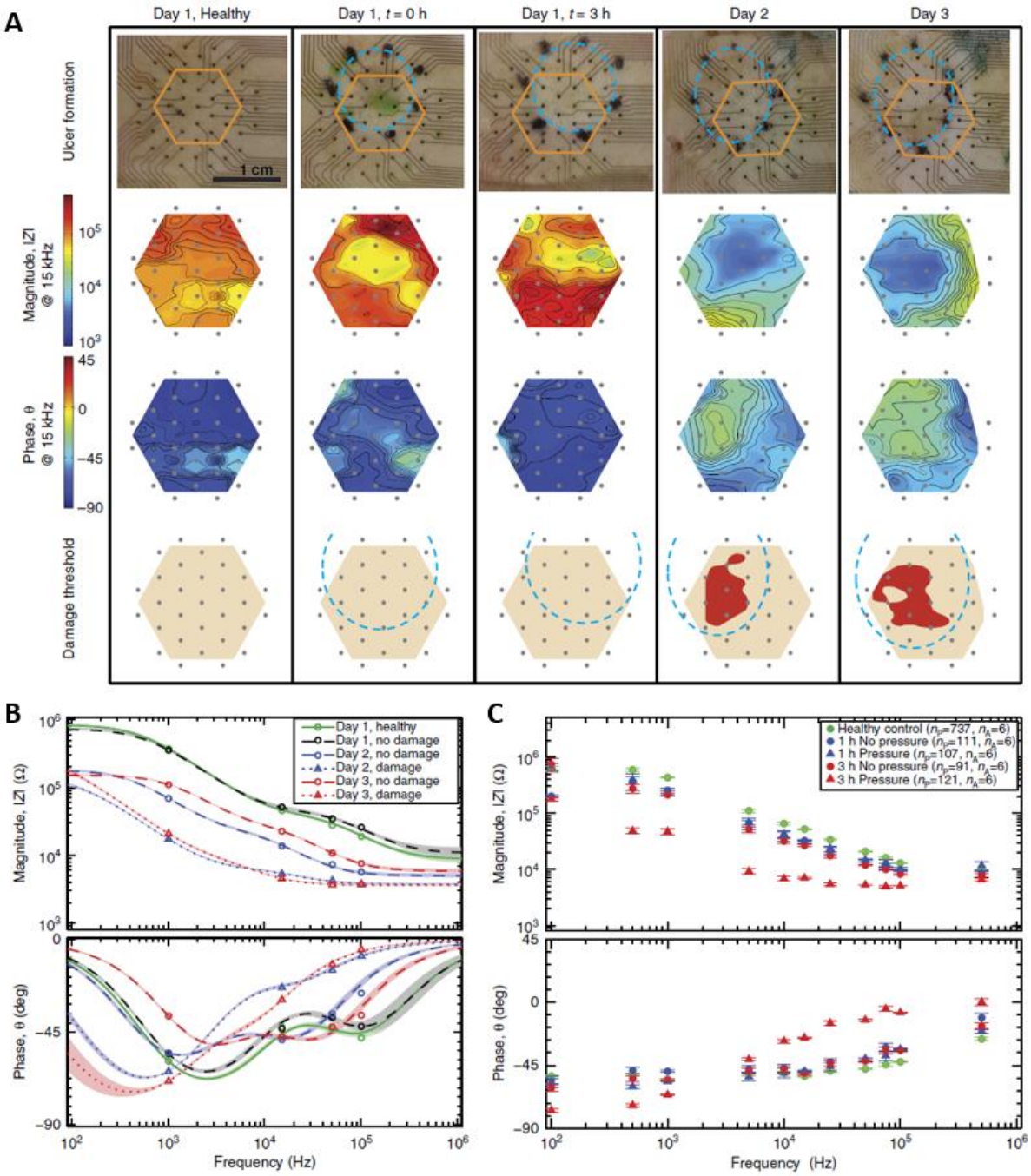

Figure 2.8 – Impedance spectrum identifies tissue damage

(A) Progression of a representative example of irreversible tissue damage created with a 3 hour ischemia cycle over days 1-3. *Row 1:* The orange hexagon denotes the measurement area of the electrode array, and the dashed blue circle indicates the position of the pressure-induced damage. *Rows 2-3:* Impedance magnitude and phase angle at 15 kHz, with data depicted in spatial heat maps. *Row 4:* A damage threshold was determined using impedance data, and red areas indicate areas of tissue damage on the map. (**B)** Impedance spectra for the wound in (A), with differences clearly observed between damaged and undamaged skin. **(C)** Impedance spectra for locations experiencing pressure or no pressure measured on day 3 and averaged over all animals in the study. The measurements over areas experiencing 3 hours of pressure are clearly differentiated from the others.

2.4.3 Impedance detects visually imperceptible damage

Because impedance can directly measure electrical properties of tissue, a hypothesis was formed that EIS may be able to detect early tissue damage before a severe pressure ulcer forms. Using a 1 hour ischemia cycle (N=11), mild and reversible damage was created in just over half of the cases. This was to be expected, as variation between animals can explain the differences in time necessary to create lasting tissue damage. The skin appeared slightly white during the reperfusion cycle immediately following magnet removal, but no visible ulcer developed after monitoring for 9 days. Using the same damage threshold applied to the 3 hour cases, tissue damage was observed the day following pressure treatment but receded after day 3 (Fig. 2.9A). Analysis of the frequency response plots again indicates that damaged tissue can be clearly separated from healthy tissue (Fig. 2.9B).

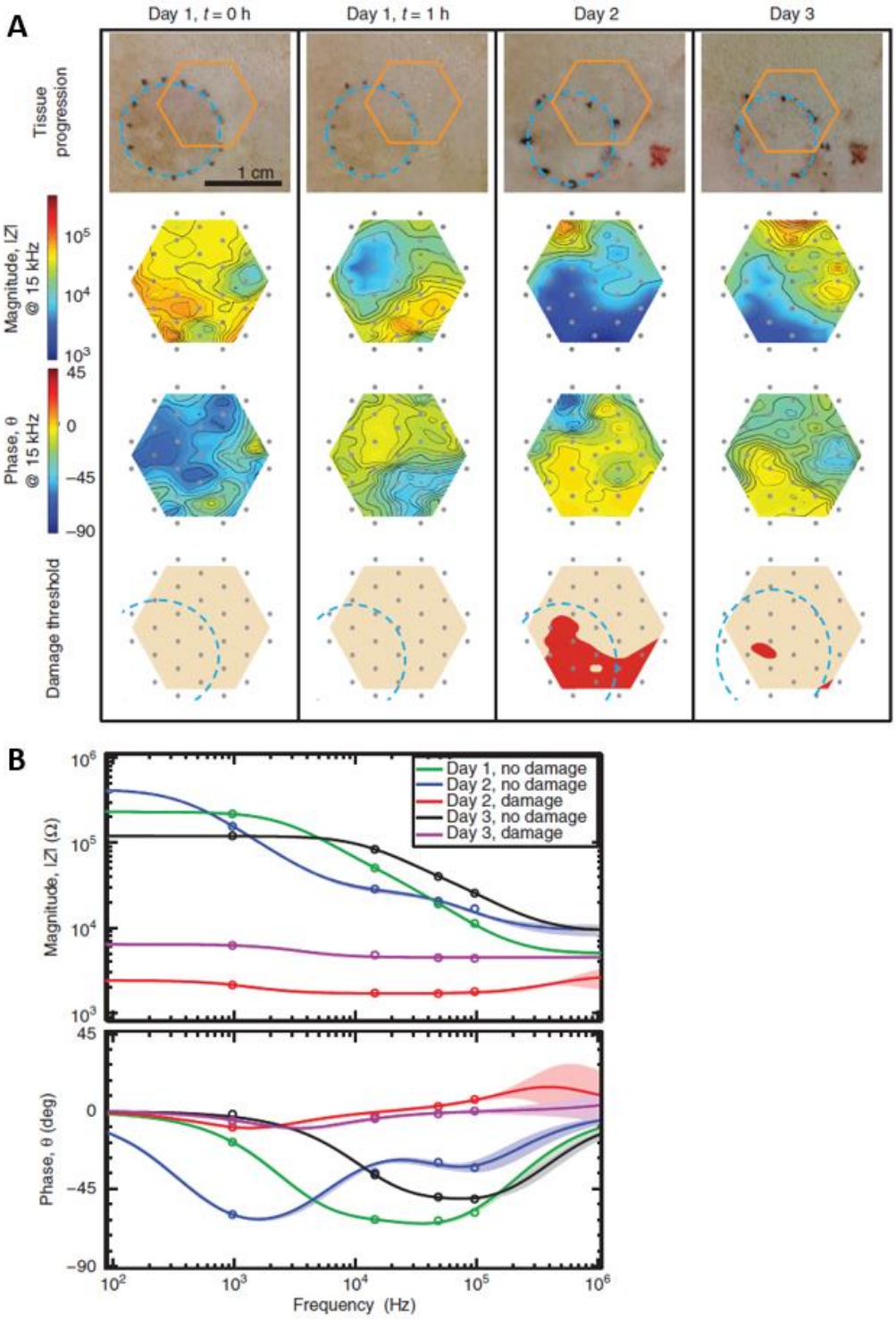

Figure 2.9 – Impedance identifies reversible pressure damage

(A) Progression of reversible pressure damage created with a 1 hour ischemia cycle shown over days 1-3. Description of rows match those in Fig. 2.8A. **(B)** Bode plots showing impedance magnitude and phase as a function of frequency in 'no damage' and 'damage' regions on days 1-3. The damaged regions are clearly distinct from the non-damaged regions.

2.4.4 Changes in tissue structure linked to impedance changes

Examination of histological sections (Fig. 2.10) by a pathologist supports impedance results that reflect cellular changes due to pressure-induced tissue damage. The skin samples from the 1 hour ischemia group showed little to no evidence of skin ulceration, with mostly normal skin alongside some orthokeratosis (formation of an anuclear layer) and compact hyperkeratosis (small amount of thickening in the outermost layer of the epidermis). However, skin samples from the 3 hour ischemia group showed ample evidence of tissue damage and ulceration. Lesions showed loss of epidermis, overlying necroinflammatory debris with serum crust (scabbing), and inflammation composed of lymphocytes and neutrophils. The inflammatory reactions even infiltrated deeper dermal layers, skeletal muscle, and fascia in some cases.

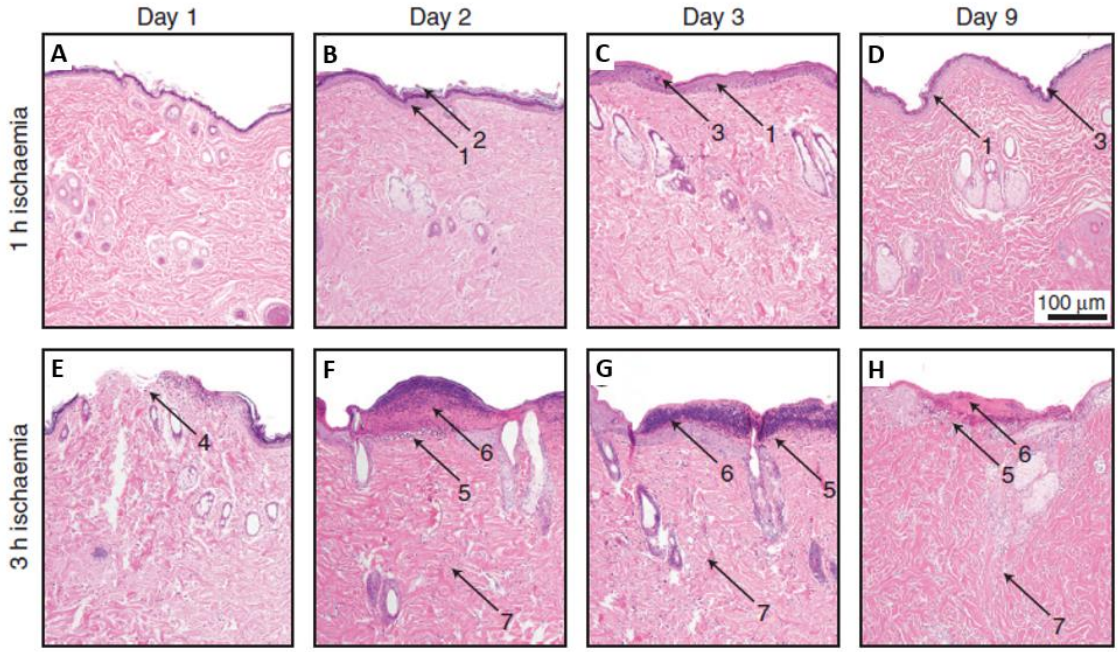

Figure 2.10 – Histology of skin samples
Skin samples were collected for histology on days 1, 2, 3 and 9, and processed with hematoxylin and eosin staining. Samples **(A-D)** were taken from animals in the 1-hour pressure treatment group, while samples **(E-H)** were taken from animals in the 3-hour pressure treatment group. All images were taken with 100x magnification. **(A)** Normal-looking dermis and epidermis. **(B)** No signs of ulceration. Normal epidermis (1) with orthokeratosis (2). **(C-D)** No signs of ulceration. Normal epidermis (1) with compact hyperkeratosis (3). **(E)** Early small ulcer (4). **(F-H)** Loss of epidermis (5) and necroinflammatory debris (scab, 6) with inflammation (7) and inflammatory cells (neutrophils and lymphocytes, 8) deeper in the dermis.

2.5 Conclusion

A smart bandage was developed using a flexible electrode array to non-invasively detect and monitor pressure-induced tissue damage in a rat model *in vivo*. The device could clearly differentiate between damaged tissue and healthy tissue, as confirmed by visual inspection and histological evidence. Importantly, this method and the calculated damage parameter were able to detect mild, reversible tissue damage that was visually imperceptible. Commercial development of a smart bandage could dramatically impact the standard of care for pressure ulcers. By providing an early detection mechanism for pressure damage by directly measuring tissue health, healthcare providers would be empowered with quantitative data that could personalize care and direct prevention and treatment strategies for individual patients. Variations in wound severity observed even in this rat model further support the use of an electrical measurement rather than current methods that rely on secondary parameters such as applied pressure. If pressure damage is identified early, pressure ulcer formation may be able to be prevented entirely by immediately addressing the area of concern. This would greatly reduce health care costs and improve patient well-being.

2.6 References

1. Sen, C. K. *et al.* Human skin wounds: a major and snowballing threat to public health and the economy. *Wound Repair Regen.* **17,** 763–71 (2009).

2. Bauer, J. D., Mancoll, J. S. & Phillips, L. G. in *Grabb Smith's Plast. Surg.* (Thorne, C. H.) 722–729 (Lippincott Williams & Wilkins, 2007).

3. Ayello, E. & Lyder, C. A New Era of Pressure Ulcer Accountability in Acute Care. *Adv. Skin Wound Care* **21,** 134–140 (2008).

4. Wong, V. Skin blood flow response to 2-hour repositioning in long-term care residents: a pilot study. *J. Wound. Ostomy Continence Nurs.* **38,** 529–37 (2011).

5. Reddy, M., Gill, S. S. & Rochon, P. A. Preventing pressure ulcers: a systematic review. *JAMA* **296,** 974–84 (2006).

6. Song, B. *et al.* Application of direct current electric fields to cells and tissues in vitro and modulation of wound electric field in vivo. *Nat. Protoc.* **2,** 1479–89 (2007).

7. Dabros, M. *et al.* Cole-Cole, linear and multivariate modeling of capacitance data for on-line monitoring of biomass. *Bioprocess Biosyst. Eng.* **32,** 161–73 (2009).

8. Rahman, A. R. A., Register, J., Vuppala, G. & Bhansali, S. Cell culture monitoring by impedance mapping using a multielectrode scanning impedance spectroscopy system (CellMap). *Physiol. Meas.* **29,** S227–39 (2008).

9. Linderholm, P. *et al.* Two-dimensional impedance imaging of cell migration and epithelial stratification. *Lab Chip* **6,** 1155–62 (2006).

10. Kell, D. B. & Woodward, A. M. Nonlinear dielectric spectroscopy of biological systems: principles and applications. *Nonlinear Dielectr. Phenom. Complex Liq.* 335–344 (2004).

11. Lukaski, H. C. & Moore, M. Bioelectrical impedance assessment of wound healing. *J. Diabetes Sci. Technol.* **6,** 209–12 (2012).

12. Kalvøy, H. *et al.* Impedance-based tissue discrimination for needle guidance. *Physiol. Meas.* **30,** 129–40 (2009).

13. Heileman, K., Daoud, J. & Tabrizian, M. Dielectric spectroscopy as a viable biosensing tool for cell and tissue characterization and analysis. *Biosens. Bioelectron.* **49C,** 348–359 (2013).

14. Jones, A., Rowland, J. J., Woodward, A. M. & Kell, D. B. An instrument for the acquisition and analysis of the nonlinear dielectric spectra of biological samples. *Trans. Inst. Meas. Control* **19,** 223–230 (1997).

15. Harris, C. M. *et al.* Dielectric permittivity of microbial suspensions at radio frequencies: a novel method for the real-time estimation of microbial biomass. *Enzyme Microb. Technol.* **9,** 181–186 (1987).

16. Kyle, U. G. *et al.* Bioelectrical impedance analysis--part I: review of principles and methods. *Clin. Nutr.* **23,** 1226–43 (2004).

17. Patel, P. & Markx, G. H. Dielectric measurement of cell death. *Enzyme Microb. Technol.* **43,** 463–470 (2008).

18. Markx, G. H. & Davey, C. L. The dielectric properties of biological cells at radiofrequencies: Applications in biotechnology. *Enzyme Microb. Technol.* **25,** 161–171 (1999).

19. Kell, D. B., Markx, G. H., Davey, C. L. & Todd, R. W. Real-time monitoring of cellular biomass: methods and applications. *Trends Anal. Chem.* **9,** 190–194 (1990).

20. Khan, Y. *et al.* Inkjet-Printed Flexible Gold Electrode Arrays for Bioelectronic Interfaces. *Advanced Functional Materials* **26,** 1004–1013 (2016).

21. Fuller, S. B., Wilhelm, E. J. & Jacobson, J. M. Ink-jet printed nanoparticle microelectromechanical systems. *J. Microelectromechanical Syst.* **11,** 54–60 (2002).

22. McAdams, E. T., Jossinet, J., Lackermeier, a & Risacher, F. Factors affecting electrode-gel-skin interface impedance in electrical impedance tomography. *Med. Biol. Eng. Comput.* **34,** 397–408 (1996).

23. Stadler, I., Zhang, R.-Y., Oskoui, P., Whittaker, M. S. & Lanzafame, R. J. Development of a simple, noninvasive, clinically relevant model of pressure ulcers in the mouse. *J. Invest. Surg.* **17,** 221–7 (2004).

24. Herrman, E. C., Knapp, C. F., Donofrio, J. C. & Salcido, R. Skin perfusion responses to surface pressure-induced ischemia: implication for the developing pressure ulcer. *J. Rehabil. Res. Dev.* **36,** 109–20 (1999).

25. Peirce, S. M., Skalak, T. C. & Rodeheaver, G. T. Ischemia-reperfusion injury in chronic pressure ulcer formation: a skin model in the rat. *Wound Repair Regen.* **8,** 68–76 (2000).

Chapter 3: Translation of impedance device to monitor pressure ulcers in patients

This chapter is adapted largely from the following conference paper with permission from:

Amy Liao*, Monica C. Lin*, Lauren C. Ritz, Sarah L. Swisher, David Ni, Kaylee Mann, Yasser Khan, Shuvo Roy, Michael R. Harrison, Ana Claudia Arias, Vivek Subramanian, David Young, Michel M. Maharbiz. Impedance sensing device for monitoring ulcer healing in human patients. in *IEEE Engineering in Medicine and Biology Conference.* 5130–5133 (2015). doi:10.1109/EMBC.2015.7319546

A.L., M.C.L., and S.L.S. designed and built the control hardware. Y.K. contributed to design of the flexible electrode arrays. D.N. and K.M. programmed the control software, with input from A.L., M.C.L., and S.L.S. A.L., M.C.L., and L.C.R. collected data on human patients, and D.Y. aided in clinical interpretation. S.R., M.R.H., A.C.A., V.S., and M.M.M. contributed to the experimental design and prepared supporting grants. This work was funded by the National Science Foundation under grant EFRI-1240380.

Section 3.7.2 includes work done in collaboration with Judy Sakanari, Fidelis Cho-Ngwa, Christina Bulman, Ndi Emmanuel, and Amy Liao. M.C.L. and C.B. collected the data, and MC.L. and A.L. performed data analysis. M.C.L. and A.L. developed the measurement system, and C.B. and N.E. conducted the biological assays. J.S. and F.C.N. contributed to experimental design and prepared supporting grants. This work was funded by a Gates Foundation Grand Challenge Grant.

This chapter also includes content adapted from the following thesis with permission from:

Amy Liao. Instrumenting Flexible Substrates for Clinical Diagnosis and Monitoring. (2018).

3.1 Abstract

Chronic skin wounds affect millions of people each year and take billions of dollars to treat. Ulcers are a type of chronic skin wound that can be especially painful for patients and are tricky to treat because current monitoring solutions are subjective. An impedance sensing tool has been developed to objectively monitor the progression of healing in ulcers, and a clinical trial has begun to evaluate the safety and feasibility of our device to map damaged regions of skin. Impedance data has been collected on five patients with ulcers, and impedance was found to correlate with tissue health. A damage threshold was applied to effectively identify certain regions of skin as "damaged tissue".

3.2 Introduction

Chronic skin wounds significantly threaten public health and the economy, costing an estimated $25 billion per year to treat. Pressure ulcers are a particularly morbid type of chronic wound – they affect over 2.5 million patients and cost approximately $11 billion per year in the United States alone[1]. Pressure ulcers are formed by constant pressure or rubbing applied to an area of skin, often over a bony prominence, that results in breakdown of the skin. Bedridden patients who are diabetic, obese, or elderly are at particularly high risk of developing pressure ulcers, and can incur these injuries simply from lying in the same position for the duration of a long surgery[1-3]. Other ulcers can also be formed from a variety of additional factors, including excessive rubbing or irritation, edema, and having a compromised immune system. These kinds of chronic wounds require that patients attend frequent doctor visits, often weekly or more often, to monitor the ulcer and undergo treatment. Monitoring of an ulcer can be very subjective and dependent on clinical experience, revealing the need for an objective tool that can help direct and standardize patient care.

A number of groups have studied electrical changes in cells and tissues *in vivo* and *in vitro*, and have correlated electrical properties with cell types[4-7]. A cell can be represented electrically as a combination of resistances and capacitances. Cytoplasm within the cell and extracellular fluid are ion-rich mediums that can be modelled as resistors, while the cell membrane can be modelled as a capacitor. Previous studies have examined the dielectric response of cell suspensions and tissues. Distinct dispersions, step changes in the complex permittivity of the material, are associated with particular molecular-level processes[8]. When utilized *in vivo*, impedance spectroscopy can detect subtle changes in tissue type and tissue health, enabling objective assessment and providing unique insight into the condition of a wound[6,9].

Pressure ulcers are classified on a scale from I to IV based on the severity of tissue damage (Fig. 3.1)[10,11]. Stage I describes a localized area of erythema (superficial reddening), while Stage II indicates a pressure injury with partial-thickness skin loss (dermis is exposed). When full-thickness skin loss is evident (adipose is visible), a pressure injury falls under Stage III. Finally, when tissue loss is evident as well (soft tissue such as muscle and ligaments, or bone, is exposed), an ulcer is categorized as Stage IV. 42% of Stage I ulcers progress to a more severe ulcer stage[12], so effective diagnostic and monitoring techniques would greatly improve treatment of patients.

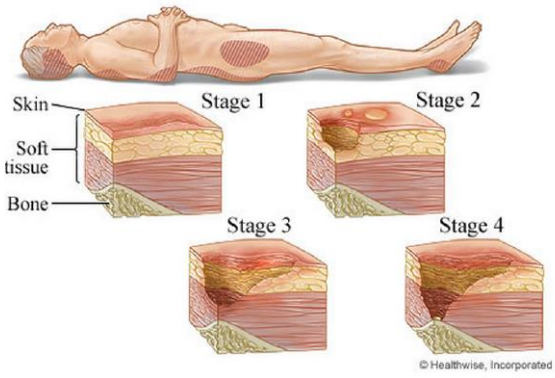

Figure 3.1 – Pressure ulcer formation and stages
Areas on the body at high-risk of developing pressure ulcers are highlighted, and diagrams depicting increasing degree of injury through the 4 stages are shown. Image source: http://www.webmd.com/skin-problems-and-treatments/four-stages-of-pressure-sores

This chapter uses the device described in Chapter 2 and applies it to a clinical trial to evaluate its safety and feasibility to map ulcers and understand relevant impedance profiles in human patients. To translate this device to patients, hardware and software had to be optimized for use on humans and by clinic staff. Data collected on five patients with Stage I, II, and III ulcers are presented.

3.3 Optimization of device design for clinical use

3.3.1 Flexible electrode array

The flexible electrode arrays used in this study were fabricated commercially to ensure robustness, using copper on polyimide, plated with electroless nickel immersion gold (Tramonto Circuits, Stillwater, MN). Two versions of the array were utilized in the clinical study – one that covered a circular area 0.7 inches in diameter, and another that covered a circular area 2 inches in diameter (Fig. 3.2A-B). The 0.7-inch board had 300 µm diameter pads spaced 2.54 mm apart, while the 2-inch board had 635 µm diameter pads spaced 7.333 mm apart. Selection of which array to use was based upon size and anatomical location of the ulcer on each patient.

In order to minimize contact impedance, SignaGel (Parker Laboratories Inc., Fairfield, NJ), a highly conductive electrode gel, was selectively applied to each electrode (Fig. 3.2C). To do this reproducibly, HT-6240 thin silicone rubber sheets (Stockwell Elastomerics, Philadelphia, PA) were patterned with small holes to use as a stencil over which to blade-coat the gel.

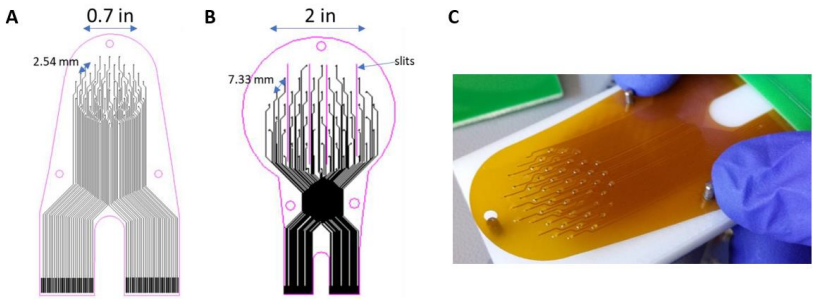

Figure 3.2 – Commercially-fabricated flexible electrode arrays
(A-B) Circuit board layouts for 0.7 and 2 inch array boards. **(C)** 0.7 inch array board with hydrogel applied selectively to each electrode.

3.3.2 Hardware improvements

Similar to the rat study presented in Chapter 2, impedance magnitude (|Z|) and phase (θ) were measured using a Keysight Technologies E4980AL 20 Hz to 1 MHz Precision LCR meter. 2-point impedance measurements were taken by applying a 100 mV constant voltage sine wave output signal with a frequency of 100 Hz to 1 MHz. The control hardware allowed each electrode on the array to be independently selected, enabling the measurement of impedance between any two electrodes. A microcontroller on the board was programmed to make pairwise measurements between all nearest neighbor electrodes over a range of frequencies, routing test signal from the LCR meter to each pair of selected electrodes. Taking into account feedback from clinical collaborators, a few changes were implemented to optimize the control board for clinical use. Connectors on the board were replaced to enable easy and more robust set up of the system, selecting different connectors as necessary for the electrode array, Pololu programmer, LCR meter, and battery to prevent potential confusion. The four AA batteries originally used to power the control board were also removed, instead drawing power from the laptop through a USB connection that was already in place for communication with the microcontroller. The new control board also saw a reduction in size to roughly 2 x 2 inches.

3.3.3 Data analysis

User interface software was specially developed for use by clinical personnel in the study. For each patient, at least two sets of impedance measurements were taken, one set on healthy skin to serve as a baseline, and one set on the ulcer. Each set contained a measurement across each of 72 nearest-neighbor electrode pairs on the array at four frequencies (1, 15, 50, and 100 kHz), as well as a measurement across each of 11 select pairs on the array at 12 frequencies ranging from 100 Hz to 1 MHz. After a set of measurements was taken, a simple button press could trigger the

plotting of visually intuitive maps of the measurement area. A nurse or physician could quickly examine these maps to understand the severity of an ulcer.

A number of custom MATLAB scripts were written to analyze the impedance data. To create the visually intuitive maps, the data was first filtered and averaged, then a simple interpolation was applied to smooth out the graphs. Additional post-processing was done to extract more frequency-dependent information from the data. Transfer functions were fit to the Bode plots, and fits were compared between the different types of tissue present in and around an ulcer. A contrast optimization process identified 15 kHz as the frequency at which the largest spread in impedance existed between healthy tissue and ulcerous tissue.

3.4 Clinical study

3.4.1 Patient selection

A clinical trial was conducted at two locations: St. Mary's Wound Clinic and the Laguna Honda Hospital in San Francisco, CA. The study population included males and females between 18 to 80 years of age and that required weekly wound assessments by a physician or registered nurse. Each patient had to have an ulcer between Stages I and III as defined by the National Pressure Ulcer Advisory Panel (NPUAP) classification[11]. Ulcers were to be located on common pressure points including the sacrum, ischium, trochanters, heels, and elbows. For practicality, injuries in locations with minimal hair were selected.

Patients with stage IV pressure ulcers were excluded due to the extreme topography of the ulcers, which would make proper placement of the device difficult. While the back of the head is an anatomical area that often develops ulcers in high-risk patients, wounds in this location would require shaving the head and were thus excluded from this study.

The five patients presented here had ulcers ranging from stage I to stage III on their leg, foot, or sacrum, and shaving was not necessary. Patients included two males and three females from ages 57 to 70. The flexible array board was adhered to the patient using Versatel^{TM} contact layer wound dressings, which caused no irritation to the patient.

3.4.2 Observed wound tissue

Tissue impedance was measured between 10^2 and 10^6 Hz across every nearest neighbor pair in the electrode array using a 100 mV_{RMS} constant voltage test signal generated by the LCR meter. For each patient, two measurements were taken: 1.) on "healthy" skin in an area adjacent to the ulcer and 2.) at the border of the ulcer. Wounded tissue in the ulcer was categorized as granulation tissue, slough, or necrotic tissue (Fig. 3.3) in a single-blinded fashion by a surgical resident using digital photographs. Damaged tissue that did not fit into one of those 3 types was lumped into a general "ulcer" category. Granulation tissue forms on the surface of wounds, and is a highly vascularized tissue that appears moist and bumpy. Slough is a thick, fibrous tissue and consists of fibrin, pus, and other proteinaceous materials that require debridement to facilitate healing of the wound. Necrotic tissue typically appears a red to dark brown color, consisting of dead cells and debris, often like a scab.

Figure 3.3 – Observed wound tissues
The different types of tissue observed in pressure ulcers measured for this study include granulation tissue, necrotic tissue, and slough. Healthy tissue was also measured in surrounding areas.

3.5 Results

3.5.1 Skin layers dominate impedance measurements

Human skin is a complex organ made up of three distinct layers including the epidermis, dermis, and subcutis. Each layer of the skin will have a characteristic impedance spectrum determined by its structure, moisture level, etc. When impedance measurements are taken, current penetrates the tissue, traveling from one electrode to the other. The depth of this penetration depends on the current frequency, electrode spacing, and the intra-and extracellular properties of the tissue being measured[5]. Low frequency current reflects primarily the extracellular space because it does not penetrate the capacitive cell membrane. High frequency current more easily crosses the membrane and moves deeper through the tissue. While low frequency current may capture information about the resistivity of the ionic fluid in tissue, high frequency current may provide information about deeper layers of skin (Fig. 3.4A). Electrode spacing can also have a large effect on current path, as electrodes spaced further apart can allow current to penetrate more deeply (Fig. 3.4B).

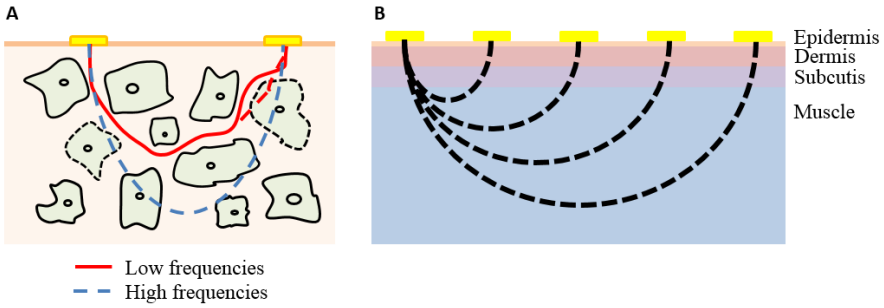

Figure 3.4 – Current penetration depth
(A) Schematic illustrating how low and high frequency current travel through tissue. **(B)** Diagram illustrating penetration depth as a function of electrode spacing.

The understand the effects of electrode spacing on EIS measurements taken over human skin, impedance data was collected between electrodes spaced a 0.1, 0.2, 0.3, 0.4, and 0.5 inches apart on normal, healthy skin on the forearms of 3 subjects. Impedance magnitude should rise proportionally with increasing electrode spacing if tissue is homogeneous. However, impedance

measurements (Fig. 3.5) reflected very little difference regardless of electrode spacing. These results suggest that the same set of tissue was being measured irrespective of electrode spacing. Studies have described the tissues that make up skin (epidermis, dermis, and subcutaneous fat) as having much higher impedance than the underlying muscle tissue[13]. This could lead to the skin layers dominating contribution to impedance values. If tissue is damaged, the relative impedances of the three skin layers to the underlying muscle may shift and result in electrode spacing having a larger impact on EIS measurements. In addition, high contact impedance between the electrodes and skin could also explain the negligible effect of electrode spacing.

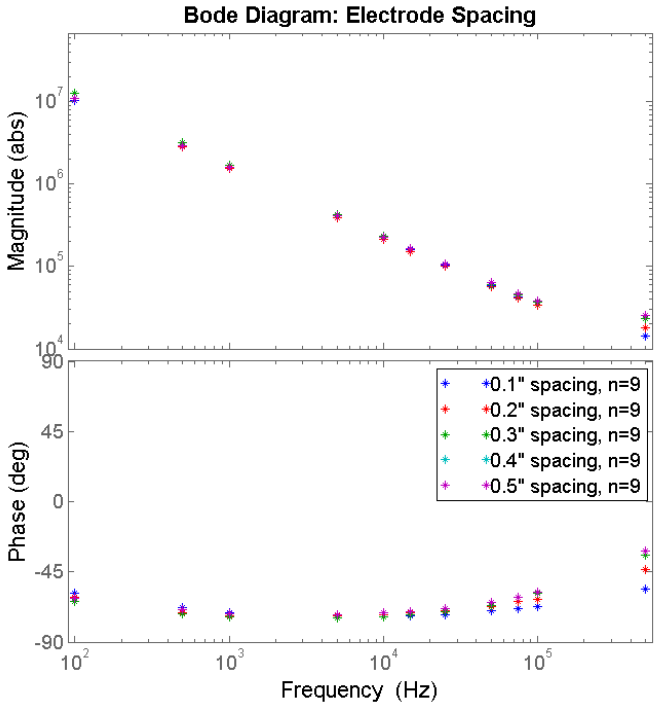

Figure 3.5 – Impedance of healthy skin as a function of electrode spacing
Impedance magnitude and phase do not change significantly with respect to electrode spacing, indicating that the skin layers dominate due to higher impedance of the epidermis, dermis, and subcutis layers relative to the underlying muscle.

3.5.2 Impedance correlates with tissue health

EIS data collected in all 5 patients (Fig. 3.6) indicated that the impedance magnitude of granulation tissue within an ulcer region was consistently lower than the healthy tissue on that same patient.

Correspondingly, phase angle was closer to 0°, reflecting a more resistive measurement in granulation tissue. Impedance of slough tissue appeared to have similar impedance values. Both granulation and slough tissue often appear moist and involve cellular break down, leading to the changes in impedance observed. Necrotic tissue on the other hand resulted in a |Z| value at or above that of normal healthy tissue. As necrotic tissue tends to be a dry scab-like tissue, it is expected to have higher |Z| than the other ulcerous tissue.

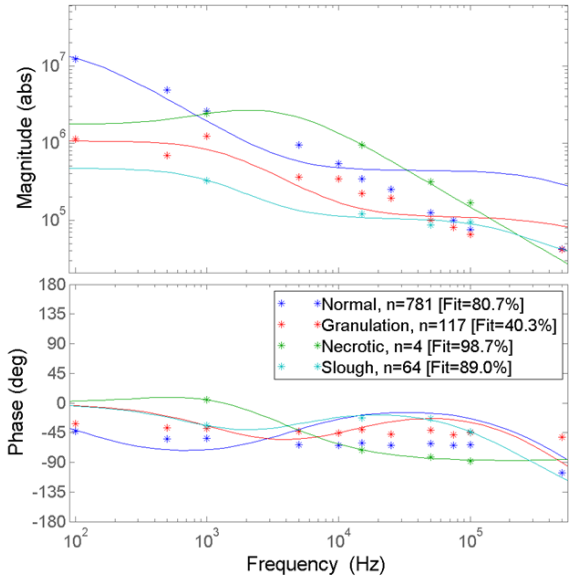

Figure 3.6 – Wound tissues differ in frequency response
Impedance magnitude and phase are plotted as a function of frequency, averaged across all pairs for all 5 patients. Thresholds set at $|Z| < 100\ k\Omega$ and $-30° < \theta < 10°$ at 15 kHz were able to robustly identify damaged tissue.

3.5.3 Thresholding algorithm predicts tissue damage

By combining analysis of all impedance data at all frequencies for the 5 patients in this study, the spread in |Z| and θ across tissue types was found to be largest at 15 kHz. Thresholds were determined at this frequency to robustly identify damaged tissue while minimizing false positives: $|Z| < 100\ k\Omega$, $-30^o < \theta < 10^o$. Electrode pairs that measured values falling in this range were classified as measuring damaged tissue, which included granulation and slough tissue. There were not enough data points to identify a robust threshold for necrotic tissue. Both |Z| and θ were

included in the damage threshold to reduce variation between patient skin types. After applying this threshold, spatial maps were created to enable physicians to rapidly assess wound size and location (Fig. 3.7).

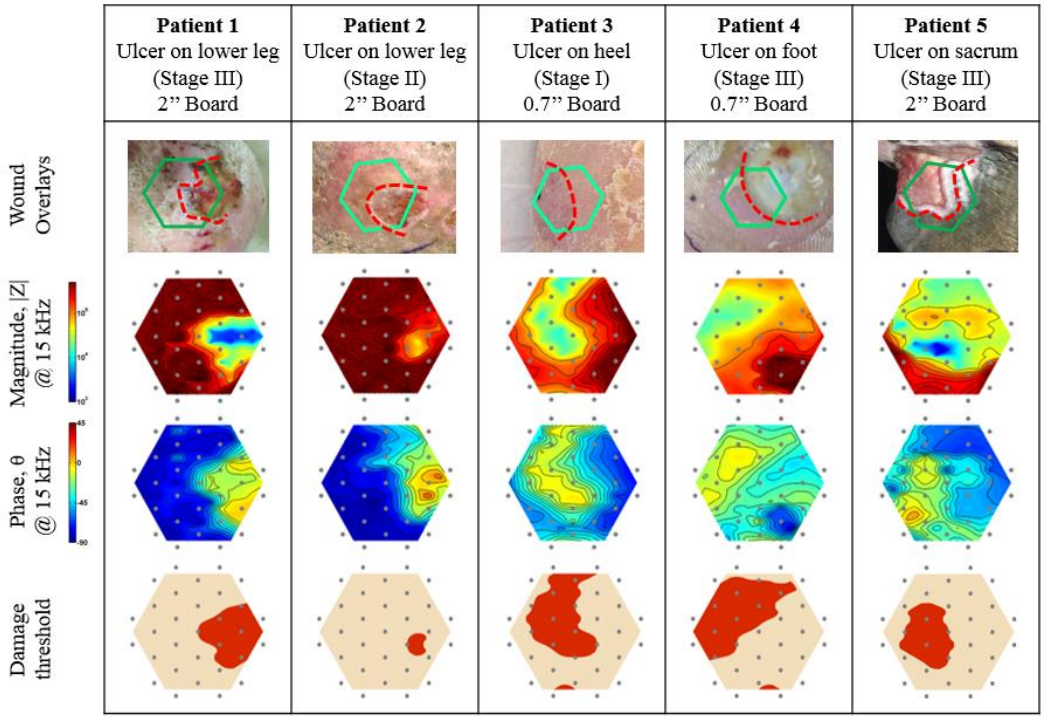

Figure 3.7 – Heat maps and damaged tissue identification for 5 patients
The top row provides digital photographs of each of the pressure ulcers measured, with a green hexagon outlining the measurement area and the dashed red line outlining the wound border. Impedance magnitude and phase plotted on a color scale for each of the 5 patients. A damage threshold identified location of tissue damage on the skin; its location is indicated on the bottom row.

3.6 Conclusion

Translation of an impedance measurement system for use on human patients involved optimizing flexible electrode arrays for conformal contact with the skin, miniaturizing hardware for ease-of-use, and simplifying software for operation by clinical staff. The smart bandage presented here demonstrates a non-invasive sensor for monitoring pressure ulcers. The device was able to differentiate between several different tissue types, including healthy skin, granulation tissue, slough, and necrotic tissue. By directly measuring tissue health, it can provide more accurate quantitative information than traditional subjective methods about patient wounds under the care

of nursing staff in a hospital setting. By providing an objective measure of wound health, impedance can help drive treatment decisions for patients.

To commercialize this system as a medical device, further optimization is necessary to enhance utility. Wireless functionality will eliminate the need to tether patients to a laptop, and thus greatly improve portability. This would also enable more frequent measurements over time, and could facilitate a full-scale clinical trial that tracks longitudinal progress of patients with pressure ulcers requiring constant care. Assessing tissue health at early stages is also of particular interest to clinicians, as it may enable prevention of pressure ulcer formation. Ultimately, these types of tools can ease the burden on nursing staff for prevention efforts and arm physicians with additional information to guide treatment.

3.7 Other applications

3.7.1 Open surface wounds

This device was designed to take non-invasive measurements of impedance on the surface of the skin, and can be applied to other applications. While pressure ulcers are a chronic wound of major concern, other open wounds such as abrasions, open sores, and lacerations may also be appropriate applications of this technology.

To demonstrate this, an open wound was created by surgically excising a small patch of skin (roughly 1 cm in diameter) from the back of a rat using a scalpel (N=1). EIS measurements were taken using a flexible array board on days 1, 2, 3, and 5 to track the progress of wound healing. Impedance data plotted in spatial maps was able to not only determine the border of the wound, but also differentiate between the changing states of the wound over healing time. Initially on day 1, impedance in and around the wound was much lower than the untouched skin further away, as

the wound exudate created a moist environment of highly ionic fluid. Due to cell membrane breakdown, the wound bed appeared to be more conductive and less capacitive, as evidenced by lower |Z| and less negative θ. By day 3 a scab had formed, which was characterized by much higher |Z| due to the dry nature of tissue and presence of high resistance fibrin plugs. θ in this case also become more capacitive, likely driven by poor contact due to the hard and bumpy surface of the scab.

By making minor changes to instrumentation, this device could also be used to measure potential differences across each set of electrodes. This could be configured to create a map of voltage and endogenous electric fields across the wound. In addition, electric fields have been shown to direct cell migration[14-17]. Electrical stimulation could be applied across the electrode array, which some studies have shown may aid in the healing process[18]. This device could be adapted to monitor the endogenous field, apply an external field, and assess the resultant response, providing important evidence regarding electrical stimulation for healing of chronic wounds.

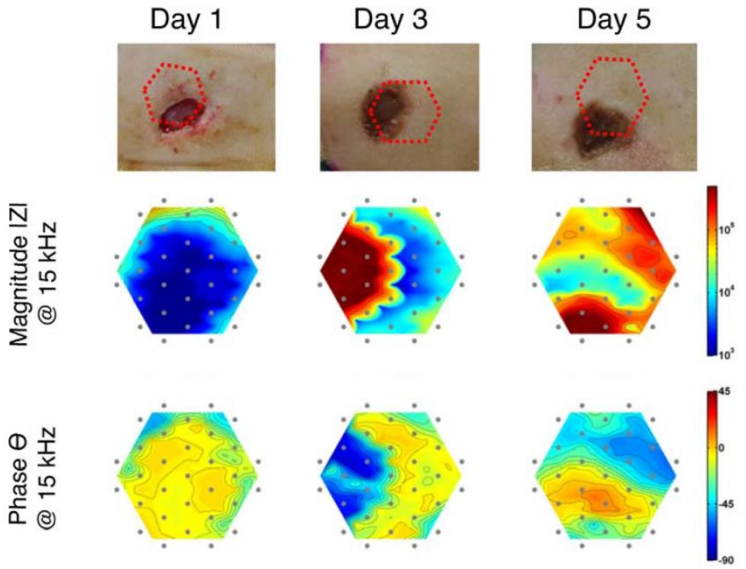

Figure 3.8 – Impedance tracks wound border
Impedance measurements taken over an electrode array placed at the border of an open, excisional wound. Photographs show where the measurement area is relative to the wound, and impedance magnitude and phase data plotted as heat maps indicate the ability of impedance to track the wound over time.

3.7.2 Non-invasive diagnosis of onchocerciasis

Point-of-care diagnostics for use in developing nations is another area that this impedance measurement system can be applied to. In particular, for diseases like onchocerciasis that currently rely on painful surgical biopsies for diagnosis, a non-invasive modality would be hugely beneficial. This proof-of-concept study was done in collaboration with Judy Sakanari (UCSF), Fidelis Cho-Ngwa (University of Buea, Cameroon), Christina Bulman (UCSF), Ndi Emmanuel (University of Buea, Cameroon), and Amy Liao (UC Berkeley).

Onchocerciasis, or river blindness, is a parasitic disease caused by infection of the filarial *Onchocerca volvulus* worm. Approximately 25 million people are infected, predominantly in sub-Saharan Africa[19]. Symptoms include severe itching, bumps under the skin, and in severe cases, blindness[20]. Infected blackflies pass the disease to humans through repeated bites, where adult worms produce microfilariae (embryonic larvae) that move throughout the skin, eyes, and other organs. Symptoms are caused by the microfilariae, which induce inflammatory responses when they die, causing severe itching and other skin changes in infected people. Eye lesions may develop that eventually lead to visual impairment, and nodules under the skin form around the adult worms.[19,20] Unfortunately, no vaccine exists, so early diagnosis and treatment are critical to controlling this disease.

Current methods of diagnosis include painful skin snips to test for microfilariae, as well as surgical removal of nodules to check for adult worms[19]. Unfortunately this method also results in unnecessary surgery for some, as nodules can end up being benign ganglion (swelling) or lipomas (fatty lumps). The recommended treatment for onchocerciasis by the World Health Organization is ivermectin[20], which must be administered every 6 months because the medication kills the larvae

but not the adult worms. In addition, severe side effects have been found in patients who are also infected with the *Loa loa* parasite[19], another disease found in this geographic region.

Here, the overall goal was to develop a non-invasive tool to determine viability of adult *Onchocerca voluvus* worms in nodules, which would aid in diagnosis and assessment of disease state. In addition, this technology could be applied toward epidemiological surveillance following mass drug administration of a macrofilaricide. This would greatly support efforts to identify new treatment options with fewer side effects. To complete a proof-of-concept study, Monica Lin and Christina Bulman traveled to the University of Buea in Cameroon to examine *Onchocerca ochengi* infections in cows as a model for the human disease. *O. ochengi* is an excellent surrogate species for *O. volvulus*[21], and is found in cows in west Africa.

Infected cow hides were obtained from the local abattoir and checked for nodules. Commercially fabricated 0.7 and 2 inch diameter flexible electrode arrays were placed over nodules, taking measurements from both the muscle-side of the skin as well as the shaved outside of the skin. Impedance data at 15 kHz was plotted as a spatial heat map (Fig. 3.9), and clearly differentiates the nodule from the surrounding skin. The nodule appears to have a higher impedance magnitude and phase angle closer to 0, indicating that the nodule is less conductive and more resistive than typical skin. Following impedance tests, each nodule was excised from the cow skin (Fig. 3.10A) and worm viability was assessed using an MTT assay, a colorimetric assay for determining metabolic activity of cells[22]. In live cells, NADPH oxidoreductases reduce the tetrazolium dye (MTT, 3-[4,5-dimethylthiazol-2-yl]-2,5 diphenyl tetrazolium bromide) to the insoluble dye formazan, which is purple in color. Nodules containing live worms turned dark purple following the assay (Fig. 3.10B), while dead worms did not exhibit any color change. In the proof-of-concept study, nearly all worms were found to be alive. Future work can involve testing worms at varying

levels of viability including live and active, live but moribund, and dead. With further validation, this technology could be incorporated into point-of-care devices to help healthcare workers determine worm viability in a non-invasive way.

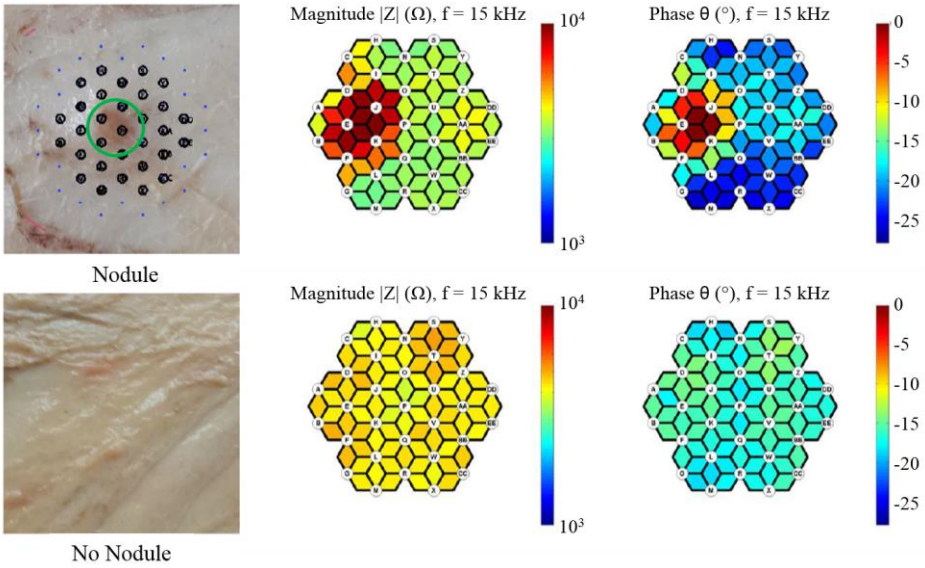

Figure 3.9 – Impedance map identifies nodule
Impedance magnitude and phase are plotted at 15 kHz in a spatial heat map. The nodule is easily identified relative to the surrounding skin, which shows a uniform baseline measurement.

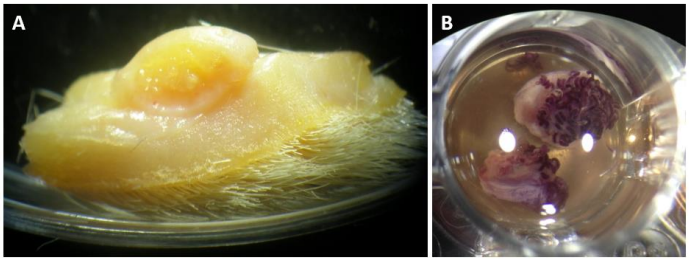

Figure 3.10 – Excised nodules tested with the MTT assay
(A) Nodules were excised following impedance measurements. When nodules are dissected, the adult worm is visible. **(B)** A nodule examined with the MTT assay turns deep purple, indicating that it is alive.

3.8 References

1. Sen, C. K. *et al.* Human skin wounds: a major and snowballing threat to public health and the economy. *Wound Repair Regen.* **17,** 763–71 (2009).

2. Ayello, E. & Lyder, C. A New Era of Pressure Ulcer Accountability in Acute Care. *Adv. Skin Wound Care* **21,** 134–140 (2008).

3. Wong, V. Skin blood flow response to 2-hour repositioning in long-term care residents: a pilot study. *J. Wound. Ostomy Continence Nurs.* **38,** 529–37 (2011).

4. Rigaud, B., Morucci, J. P. & Chauveau, N. Bioelectrical impedance techniques in medicine. Part I: Bioimpedance measurement. Second section: impedance spectrometry. *Crit Rev Biomed Eng* **24,** 257–351 (1996).

5. Grimnes, S. & Martinsen, O. G. *Bioimpedance and Bioelectricity Basics*. (Elsevier, 2015). doi:10.1016/C2012-0-06951-7

6. Lukaski, H. C. & Moore, M. Bioelectrical impedance assessment of wound healing. *J. Diabetes Sci. Technol.* **6,** 209–12 (2012).

7. Kell, D. B., Markx, G. H., Davey, C. L. & Todd, R. W. Real-time monitoring of cellular biomass: Methods and applications. *TrAC Trends in Analytical Chemistry* **9,** 190–194 (1990).

8. Markx, G. H. & Davey, C. L. The dielectric properties of biological cells at radiofrequencies: applications in biotechnology. *Enzyme Microb. Technol.* **25,** 161–171 (1999).

9. Dean, D. A., Ramanathan, T., Machado, D. & Sundararajan, R. Electrical impedance spectroscopy study of biological tissues. *J. Electrost.* **66,** 165–177 (2008).

10. Black, J. *et al.* National Pressure Ulcer Advisory Panel's updated pressure ulcer staging system. *Dermatol Nurs* **19,** 343–349; quiz 350 (2007).

11. The National Pressure Ulcer Advisory Panel - NPUAP. NPUAP Pressure Injury Stages. Available at: http://www.npuap.org/resources/educational-and-clinical-resources/npuap-pressure-injury-stages/. (Accessed: 20th August 2018)

12. Bruin Biometrics. (2013). *Pressure Ulcers: An Overview of a Painful Problem*.

13. Gabriel, S., Lau, R. & Gabriel, C. The dielectric properties of biological tissues: II. Measurements in the frequency range 10 Hz to 20 GHz. *Phys. Med. Biol.* **41,** 2251–2269 (1996).

14. Nuccitelli, R. "A Role for Endogenous Electric Fields in Wound Healing," *Curr. Top. Dev. Biol.*, vol. 58 (2003).

15. Song, B., *et al.* "Application of direct current electric fields to cells and tissues in vitro and modulation of wound electric field in vivo.," *Nat. Protoc.*, **2**, 1479–89 (2007).

16. Li, L., *et al.* "Electric fields guide migration of epidermal stem cells and promote skin wound healing.," *Wound Repair Regen.*, **20**, 840–51 (2012).

17. Cohen, D. J., Nelson, W. J., & M. M. Maharbiz, "Galvanotactic control of collective cell migration in epithelial monolayers.," *Nat. Mater.*, **13**, 409–17 (2014).

18. Isseroff, R. R. & Dahle, S. E. "Electrical Stimulation Therapy and Wound Healing: Where Are We Now?," *Adv. Wound Care*, **1**, 238-243 (2012).

19. CDC-Centers for Disease Control and Prevention. CDC - Onchocerciasis. (2017). Available at: https://www.cdc.gov/parasites/onchocerciasis/index.html. (Accessed: 21st August 2018)

20. World Health Organization. Onchocerciasis (river blindness). *World Health Organization* Available at: http://www.who.int/news-room/fact-sheets/detail/onchocerciasis. (Accessed: 21st August 2018)

21. Trees, A. J., Graham, S. P., Renz, A., Bianco, A. E. & Tanya, V. Onchocerca ochengi infections in cattle as a model for human onchocerciasis: recent developments. *Parasitology* **120 Suppl,** S133-142 (2000).

22. van Meerloo, J., Kaspers, G. J. L. & Cloos, J. Cell sensitivity assays: the MTT assay. *Methods Mol. Biol.* **731,** 237–245 (2011).

Chapter 4: Impedance spectroscopy to analyze tissue composition in bone fractures

This chapter is reprinted from the following journal article with permission from:

Monica C. Lin, Frank Yang, Safa T. Herfat, Chelsea S. Bahney, Meir Marmor, Michel M. Maharbiz. New opportunities for fracture healing detection: Impedance spectroscopy measurements correlate to tissue composition in fractures. *Journal of Orthopaedic Research* **35,** 2620–2629 (2017).

M.C.L., S.T.H., C.S.B., M.M., and M.M.M. designed the research study, and M.C.L., F.Y., S.T.H., and C.S.B. contributed to data acquisition. M.C.L. analyzed the data and drafted the manuscript, while S.T.H., C.S.B., M.M., and M.M.M. provided conceptual advice and critically revised the paper. M.C.L., S.T.H., C.S.B., M.M., and M.M.M. prepared supporting grants. The work in this chapter was funded by the National Science Foundation under grant EFRI-1240380 and an NSF/University Cooperative called the Center for Disruptive Musculoskeletal Innovations under grant IIP-1361975, and aided by a grant from the Orthopaedic Trauma Association.

4.1 Abstract

Accurate evaluation of fracture healing is important for clinical decisions on when to begin weight-bearing and when early intervention is necessary in cases of fracture nonunion. While the stages of healing involving hematoma, cartilage, trabecular bone, and cortical bone have been well characterized histologically, physicians typically track fracture healing by using subjective physical examinations and radiographic techniques that are only able to detect mineralized stages of bone healing. This exposes the need for a quantitative, reliable technique to monitor fracture healing, and particularly to track healing progression during the early stages of repair. The goal of

this study was to validate the use of impedance spectroscopy to monitor fracture healing and perform comprehensive evaluation comparing measurements with histological evidence. Here we show that impedance spectroscopy not only can distinguish between cadaver tissues involved throughout fracture repair, but also correlates to fracture callus composition over the middle stages of healing in wild-type C57BL/6 mice. Specifically, impedance magnitude has a positive relationship with % trabecular bone and a negative relationship with % cartilage, and the opposite relationships are found when comparing phase angle to these same volume fractions of tissues. With this information, we can quantitatively evaluate how far a fracture has progressed through the healing stages. Our results demonstrate the feasibility of impedance spectroscopy for detection of fracture callus composition and reveals its potential as a method for early detection of bone healing and fracture nonunion.

4.2 Introduction

Approximately 15 million fracture injuries occur each year in the United States. Up to 20% of patients experience impaired healing under normal conditions[1], significantly burdening the healthcare system[2]. Current methods for assessing fracture union are not sensitive enough: physicians rely on subjective physical examinations and radiography techniques that only detect densely mineralized tissue.[3–5] Improved monitoring of fracture healing could inform clinical decisions on when to begin weight-bearing or enable earlier diagnosis of nonunion. There remains an unmet clinical need for a quantitative, reliable method to monitor fracture healing and particularly to distinguish between the early stages of healing.

Fractures heal through a combination of direct (intramembranous) and indirect (endochondral) bone formation. Repair begins with a pro-inflammatory phase that produces a hematoma in response to the trauma (Stage 1). To stabilize the fracture gap, local osteochondral progenitors

differentiate into bone and cartilage according to the mechanical microenvironment.[1,6] In areas of high stability (e.g. along bone ends), progenitors form bone directly. However, the majority of new bone forms indirectly through a cartilage intermediate (Stage 2) due to instability between the bone ends. This cartilage callus becomes mineralized and is converted into trabeculated bone (Stage 3). In the final phase of healing, trabecular bone remodels to form cortical bone (Stage 4).[1,7,8] These stages of healing can be well characterized histologically, but standard radiographic techniques like X-ray are unable to visualize healing until bone becomes densely mineralized in Stage 4[9,10].

Electrical impedance spectroscopy (EIS) measures the frequency-dependent opposition to the flow of electrical current, and has resistive and reactive features. The heavily ionic intra and extra-cellular environment contributes to the resistive component of the response, while double-layered cell membranes contribute capacitive (reactive) effects. Low-frequency features generally arise from extracellular components, while high-frequency features reflect both intra- and extracellular environment. Here, we make measurements of impedance magnitude ($|Z|$) and phase angle (θ), where $|Z|$ reflects the magnitude of the combined components, of which tissue conductivity is often a dominant term. θ provides information about how resistive or capacitive the measurement is (0° is fully resistive, 90° is fully capacitive). Impedance has been used to characterize many biological tissues[11–14], including bone[15–17]. Because EIS can capture changes in dielectric properties and a healing fracture is dominated by different tissues, it may be able to uniquely complement a technique like X-ray that relies on tissue mineralization by providing quantitative local information about the fracture callus, particularly at early stages. In addition, prior work has used EIS to track differences over healing time between fracture and control groups[18–22]. While this data is promising, these studies are limited to fractures treated via external fixation using long metal pins as electrodes. These results as well as other work involving non-invasive measurements[23–25] suffer

from limited dynamic range due to noise from surrounding soft tissue. Furthermore, all studies were limited in their tissue analysis and did not correlate impedance measurements to histological characterization. More work is necessary to validate EIS for assessing fracture healing. Our study investigates the use of internally-placed electrodes (here in an *ex vivo* setting) as a future, highly sensitive approach for *in vivo* assessment.

The goals of this study were to correlate EIS with histologically characterized fracture tissue and understand potential barriers to integrating this technology with standard bone plates. We have previously designed an impedance measurement system to study skin health[26], and are now applying this technique to monitor fracture healing[27]. In this paper, we present a set of *ex vivo* studies to complete proof-of-concept validation that EIS can distinguish between individual fracture tissues and between simulated fracture stages in cadaver models. Since we envision this device being introduced during surgical fixation, we tested whether measurements taken adjacent to metal implants are reliable. Lastly, we used a murine fracture model and took measurements across heterogeneous fracture calluses dissected out at different points during healing to correlate impedance with callus composition. We hypothesized that EIS could accurately distinguish the tissues involved in fracture repair and provide critical data on the progression of healing.

4.3 Methods

4.3.1 Impedance measurement system

Two-point impedance measurements were taken using an Agilent E4980AL Precision LCR Meter at the following frequencies (Hz): 20, 40, 60, 80, 100, 250, 500, 750, 1k, 5k, 10k, 15k, 25k, 50k, 75k, 100k, 500k, 1M. In the cadaver study, 1 MHz measurements were removed due to poor electrical contact and high parasitic capacitance associated with large metal pins. A custom user

interface and control hardware was used to step through the frequencies with a 1V sine wave signal, recording |Z| and θ.

4.3.2 Cadaver study

Specimen Preparation:

A cadaveric leg was obtained through the UCSF Willed Body Program. Specific tissues were dissected out, stored in saline, and placed in a freezer. Specimens were thawed 24 hours prior to experimentation.

Isolated Tissue Measurements:

Tissues representing each fracture stage were dissected from the cadaver, including blood, cartilage from the meniscus, trabecular bone from the proximal tibia, and cortical bone from the tibia mid-diaphysis. Impedance measurements were taken across each tissue using two gold-plated surface electrodes (300 μm diameter). A 570g weight was placed on each tissue to ensure consistent contact with electrodes. Each set of measurements entailed 5 impedance readings at 18 frequencies (20 Hz to 1 MHz). For each tissue type, 5 sets of measurements were taken and presented as mean ± standard deviation. Transfer functions describing how tissue manipulates input signal into output signal were fit to the frequency response curves.

Simulated Fracture:

To mimic a clinical fracture in a cadaveric model, we created a comminuted fracture using a bone chisel and drilling external fixator pins bi-cortically to hold the system in place (0.4cm gap). Cartilage and trabecular bone (volume ~1.8cm^3) were individually inserted into the fracture gap, and measurements taken across the fracture using the two stainless steel pins as electrodes (2.7cm apart). A mixed-state was created by interspersing ~0.5cm^3 pieces of cartilage and trabecular bone, and inserting this amalgamation into the fracture. 5 sets of measurements were taken in each

condition and data presented as mean ± standard deviation. For each measurement set within one condition, the same sample of tissue was removed and re-inserted in a different configuration, but the electrodes remained firmly in cortical bone and were not affected by replacement of tissue.

Effect of Metal Implant:

A Synthes bone plate (6-hole, Model 245.16; West Chester, PA) was used to examine the effect of metal on impedance. Two 5mm stainless steel pins were inserted through neighboring bone plate holes (12 mm apart) to function as electrodes. Impedance measurements were taken both with and without the plate. Pins were then inserted into the bone 36 mm apart and measurements taken across bone without a plate and then with a plate and two screws located between the electrodes to mimic the "worst-case scenario". The system was flushed with saline to mimic a physiologic environment and measurements were taken in triplicate.

4.3.3 Mouse model for fracture repair

All protocols were approved by the UCSF Institutional Animal Care and Use Committee (IACUC), and this report adheres to ARRIVE Guidelines for reporting animal research[28]. Adult (10-16 weeks) male, wild-type C57BL/6 mice (22-29g) were kept in cages (≤ 5 mice/cage) with paper/cellulose bedding and easy access to food/water. Mice were monitored for signs of stress (low activity, unkempt fur, weight loss). Rodent models of fracture healing have been used since 1984[29] and are well-established as preclinical models[30,31] that provide insight into human fracture repair. We created a standardized, closed mid-diaphysis tibia fracture that was left unstabilized. Importantly, this model heals through endochondral ossification, and the timeline for healing has been previously examined in detail[31,32]. Animals were anesthetized with an intraperitoneal injection of ketamine:dexmedetomidine (1:1), and three-point bending fractures made by controlling the weight (460g) and distance (14 cm) of the force. Mice were given buprenorphine subcutaneously

immediately and 4-6 hours following surgery, then later if they displayed signs of distress. 24 mice in total were fractured and euthanized at days 4 (N=5), 8 (N=9), 14 (N=5), and 21 (N=5). Euthanasia time points were chosen to reflect stage 2 of healing (day 8 – dominated by cartilage), stage 3 (day 21 – dominated by trabecular bone), and the transition from stage 2 to 3 (day 14 – mixture of cartilage and trabecular bone)[33,34]. No samples were collected at day 28 because densely mineralized tissue is detectable by standard methods (i.e. radiography) and thus not a focus of our technology development. Following harvest, fracture calluses were isolated using a dissecting microscope. Day 4 samples could not be isolated due to lack of structural integrity at this early stage, so two tibias were left intact and processed for histology. Two day-8 mice were removed from the study because we were unable to dissect out enough tissue for an accurate measurement. Additional muscle samples were also dissected from the tibia at days 8 (N=3), 14 (N=2), and 21 (N=2) as controls. The dissected tissues (roughly spherical with 4.75 mm diameter) were placed over two 150 μm diameter gold surface electrodes spaced 0.5 mm apart, and a 150g weight was used to ensure consistent contact. 5 sets of impedance measurements were taken for each sample. Prior to each new measurement, we removed the sample, cleaned the electrodes with 70% ethanol, and replaced the sample and weight.

4.3.4 Histology

Fracture calluses were fixed immediately after measurement in 4% paraformaldehyde (pH 7.2) overnight (4°C), then decalcified in 19% EDTA (pH 7.4) for 14 days (4°C). Tissue was then put through a graded ethanol series for dehydration and embedded in paraffin. Serial 10 μm longitudinal sections were collected and stained with Hall's and Brunt's Quadruple (HBQ) stain, which stains cartilage blue and bone red.

Histomorphometric quantification of tissue composition within the heterogeneous calluses was done using stereology principles[35–37] on an Olympus CAST system with Visiopharm software. This technique correlates well with μCT for determining bone volume[38], but also enables us to quantify soft tissues in the fracture callus. Tissue identity (bone, cartilage, fibrous, marrow) was determined at 20x magnification by randomly sampling over a grid of evenly spaced points for 25% of the tissue, and total tissue volumes were calculated using Cavalieri's principle. Histomorphometry was performed on 13 of the 17 samples.

4.3.5 Data and statistical analyses

A single-factor ANOVA was used to compare the data at each frequency across different days and tissues. The Tukey-Kramer post-hoc analysis tested each pair of means for significant differences with $p < 0.05$.

To assess correlations between impedance measurements and tissue volume fractions, we performed univariate linear regression analysis. Two-tailed t-tests determined whether regression slopes were significantly different than zero. To determine predictive power of this model, we randomly split the 13 mice into two groups: one group to build a model (N=7), and one group to test (N=6). Impedance measurements for test group calluses were inputted into the model and resultant % cartilage and % trabecular bone estimates were compared against true values determined by stereology. Errors were calculated by taking the absolute difference between model and true values. This was done three times, with the mice randomly assigned each time.

4.4 Results

4.4.1 Impedance signatures differ between isolated tissue measurements

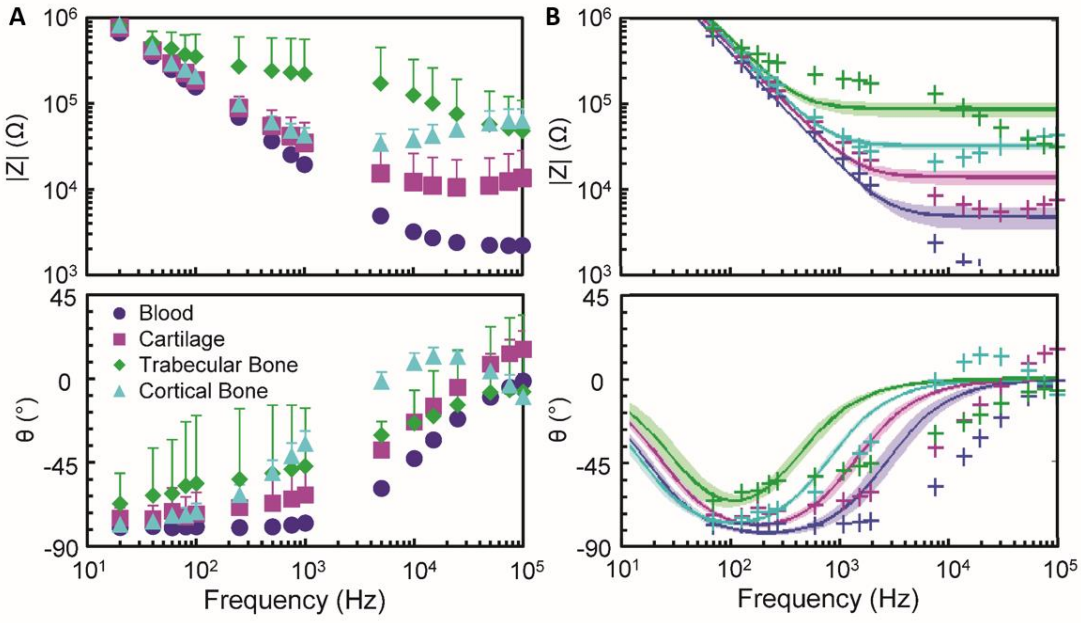

Figure 4.1 – Impedance distinguishes isolated tissues
(A) Mean |Z| and θ are plotted as a function of frequency for multiple tissues present in fracture healing (N=5 for each tissue type). Only the positive error bar is shown here for clarity in this log plot. **(B)** The cross markers indicate the averaged data values at each frequency, whereas the lines and the shaded regions indicate the estimated transfer function and the 95% fit confidence interval, respectively.

Impedance measurements of blood, cartilage, trabecular bone, and cortical bone are shown in Fig. 4.1A. |Z| increases steadily from Stage 1 tissue (blood) to Stage 4 tissue (cortical bone). However, standard deviations were substantial for trabecular bone, due to difficulty achieving reliable electrical contact *ex vivo* between electrodes and this spongy tissue. To evaluate the different curve shapes for each tissue, we fit a transfer function containing one pole and one zero (Fig. 4.1B) relating the impedance measurement (output) to the constant voltage sine wave signal (input), which changes depending on the tissue the signal travels through. This is mathematically defined as $H(s) = (s - zero) / (s - pole)$, where s is a complex frequency $\sigma + j\omega$, and σ and ω are the real and imaginary parts of s. Poles and zeros represent the roots of the denominator and numerator of the transfer function, respectively. In practice, the frequency of a pole or zero indicates an inflection

point in the frequency response. We observe that the dominant pole shifts to the right (higher frequency) and the dominant zero shifts to the left (lower frequency) as the tissues progress through healing. These differences validate the ability of EIS to distinguish tissues that make up the fracture healing process.

4.4.2 Impedance distinguishes Stage 2 and Stage 3 simulated fractures

With electrodes placed in cortical bone, the data (Fig. 4.2) indicates that impedance measurements across a fracture gap filled with cartilage are significantly different from one filled with trabecular bone. Cartilage exhibited smaller |Z| across all measured frequencies ($p < 0.002$), as well as more negative θ from 20 Hz to 1 kHz ($p < 0.05$) and less negative θ from 50 kHz to 500 kHz ($p < 0.002$). The heterogeneous mixture of cartilage and trabecular bone resulted in measurements that fell approximately halfway between the individual tissues.

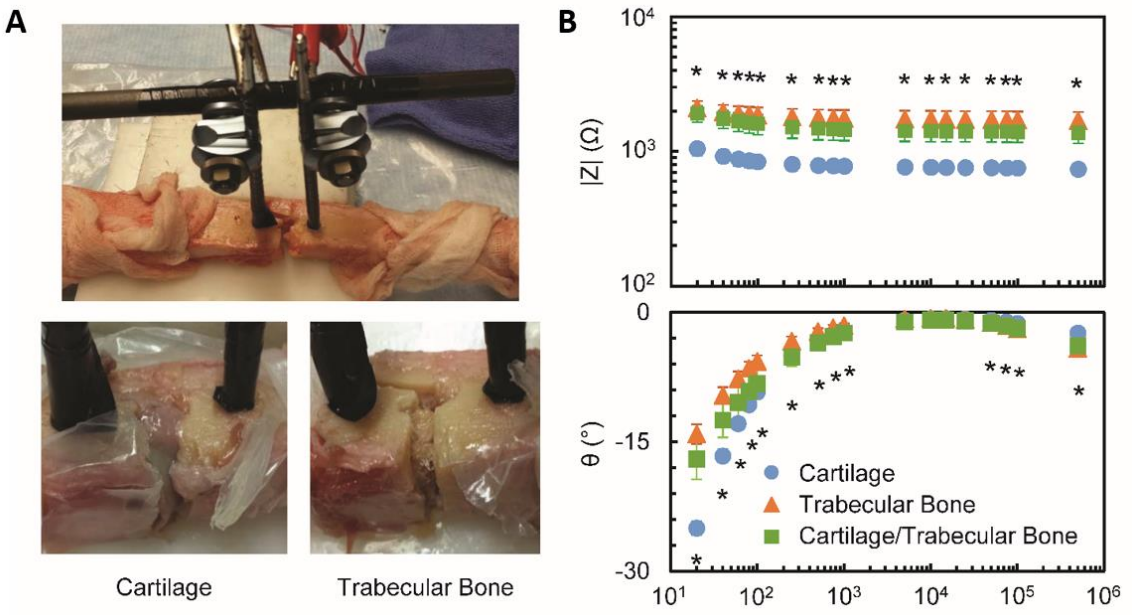

Figure 4.2 – Impedance differentiates simulated fracture stages
(A) Fractured cadaveric tibia fixed with an external fixater (top), and the fracture gap filled with cartilage (bottom left) and trabecular bone (bottom right) to simulate the 2nd and 3rd healing stages, respectively. **(B)** Plots of impedance magnitude and phase over a range of frequencies for simulated fractures press-fit with cartilage, trabecular bone, and a mixture of cartilage with trabecular bone (N=5 for each condition). As expected, |Z| of cartilage is less than that of the less conductive trabecular bone, and θ is more negative. **t-test resulted in p<0.05 between cartilage and trabecular bone*

4.4.3 Metal bone plate does not interfere with signal

To enhance clinical utility of our device, we examined whether reliable impedance measurements can be taken adjacent to metal implants in the body. As seen in Fig 4.3A, there are multiple paths in which the signal can travel. The path highlighted in blue represents the ideal path to measure the fracture callus without confounding noise from the implant. However, other paths shown depict alternate routes for the signal to travel. Our goal for this study was to elucidate which signal paths are preferred.

Impedance measurements of bone across two 12mm-spaced electrodes revealed a negligible difference across just bone (12mm-B) and across bone with a plate (12mm-BP). $|Z|$ and θ were not significantly different ($p > 0.05$) at the overwhelming majority of frequencies (left column of Fig. 4.3B). Spacing of electrodes was increased to 36 mm, and $|Z|$ across the bone only (36mm-B) was greater (as expected) compared with the 12mm measurement across the same bone (12mm-B). After addition of a bone plate and screws (36mm-BPS), $|Z|$ decreased dramatically. In this case, both $|Z|$ and θ taken with a bone plate and screws (36mm-BPS) were found to be significantly different ($p < 0.05$) from the bone-only condition (36mm-B) at nearly all measured frequencies (right column of Fig. 4.3B).

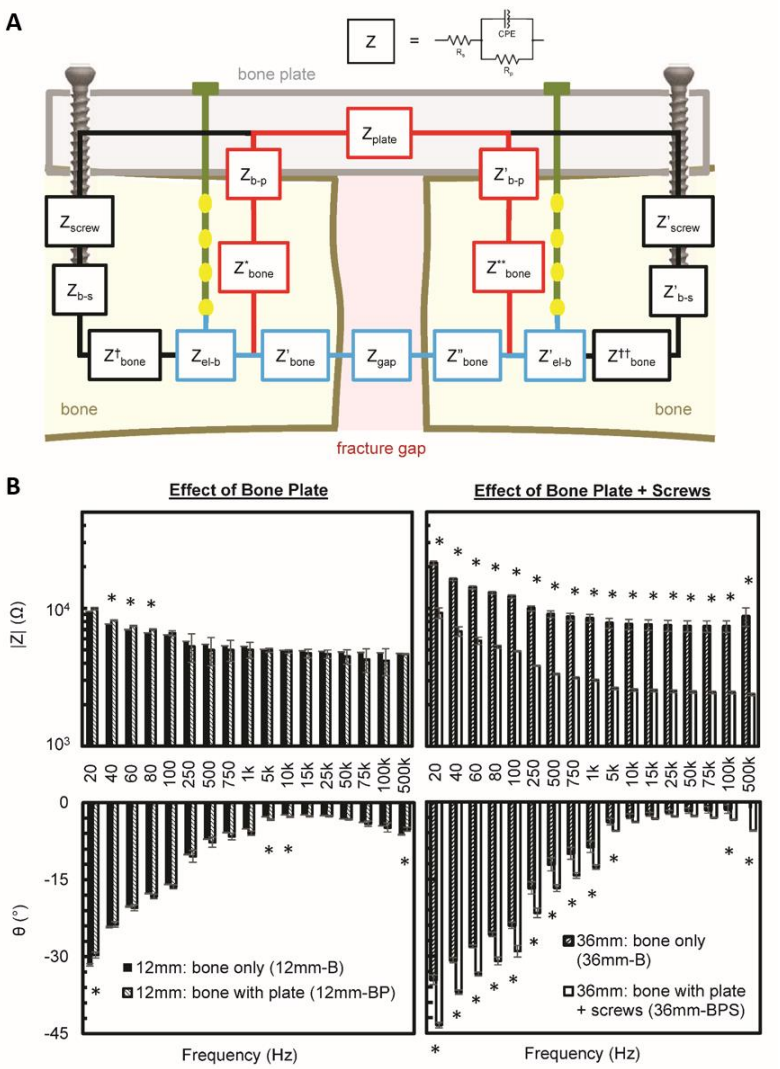

Figure 4.3 – Impact of metal hardware on impedance measurements

(A) Fracture model depicting sensors integrated in a fracture fixed with a bone plate and screws, and the multiple paths in which signal can travel between two electrodes. The blue path is the ideal path to reflect the tissue of interest within the fracture gap. Each Z component represents a Randles equivalent circuit which models an electrochemical interface (R_s = solution resistance, CPE = constant phase element, R_p = polarization resistance). **(B)** Plots of impedance magnitude and phase as a function of frequency examining the effect of a metal implant in the vicinity of the measurement electrodes (N=3 for each condition). The left column shows little difference between measurements made across bone with and without a bone plate, indicating a negligible effect from presence of a plate. The right column depicts statistically significant differences between measurements made across bone-only and bone with a plate and screws, indicating that the screws do have some effect. *$p < 0.05$

4.4.4 Impedance correlates to callus composition in mouse model

Following proof-of-concept studies in a cadaver model, we moved to a mouse model to understand EIS measurements of heterogeneous fracture calluses. Impedance was measured across calluses isolated from mice allowed to heal for 8, 14, and 21 days (Fig. 4.4); we were unable to dissect out

inflammatory tissue at day 4 due to its lack of structural integrity (Fig. 4.5). |Z| increases from day 8 to day 14 to day 21 across all measured frequencies. θ becomes less negative over healing time at lower frequencies and more negative at higher frequencies, with the inflection point occurring at 10 kHz. Standard deviations increased with later measurement days, as it was increasingly difficult to make robust electrical contact between electrodes and stiffer calluses. Despite this, ANOVA and 2-sample t-tests reveal that |Z| is significantly different from 40 Hz to 100 Hz and from 50 kHz to 1 MHz ($p \leq 0.03$), and θ is significantly different at frequencies below 1 kHz and above 100 kHz ($p \leq 0.04$). There are no discernable differences in impedance magnitude of reference muscle samples across mice and between time points ($p > 0.2$ at all measured frequencies).

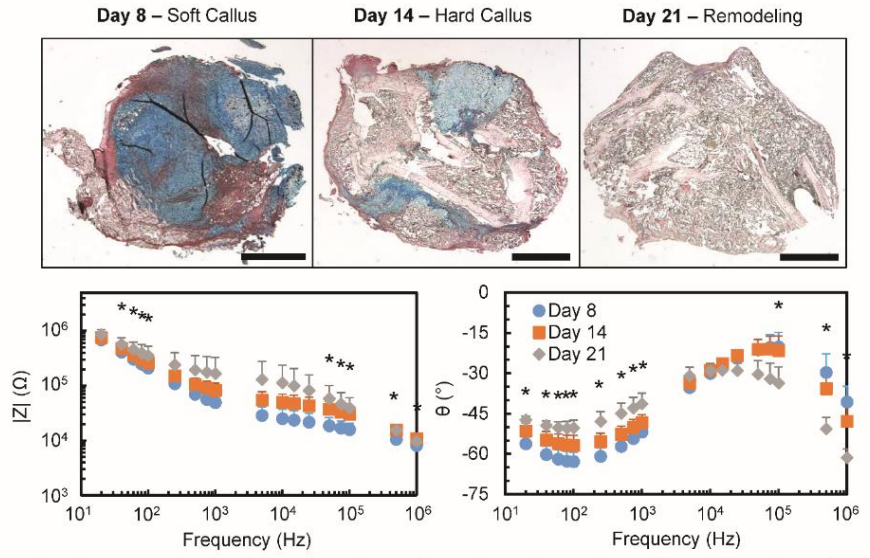

|Z|	Freq. (Hz)	40	60	80	100	50k	75k	100k	500k	500k	1M	1M
	Groups	8/21	8/21	8/21	8/21	8/21	8/21	8/21	8/14	8/21	8/14	8/21
	P-Value	=0.03	=0.03	=0.03	=0.03	=0.03	=0.02	=0.02	<0.01	<0.01	<0.01	=0.03

θ	Freq. (Hz)	20	40	60	80	100	250	500	750	1k	100k	500k	1M
	Groups	8/21	8/21	8/21	8/21	8/21	8/21	8/21	8/21	8/21	8/21	8/21	8/21
	P-Value	=0.01	<0.01	<0.01	<0.01	<0.01	=0.01	=0.02	=0.03	=0.04	=0.04	<0.01	<0.01

Figure 4.4 – Impedance of fracture calli over healing time
(A) Representative histological sections for measurement days 8, 14, and 21. Slides were stained with HBQ (cartilage stains blue and bone stains red/pink), and the scale bar is 1mm. Day 8 calluses were dominated by cartilage, day 21 calluses were dominated by trabecular bone, and day 14 calluses had a relatively even mixture of both. **(B)** Impedance magnitude and phase plotted over a range of frequencies from 20 Hz to 1 MHz for measurement days 8, 14, and 21 (N=17). Only the positive error bar is shown for clarity in this log plot. **ANOVA analysis resulted in p<0.05. The tables detail the specific groups between which there are significant differences.*

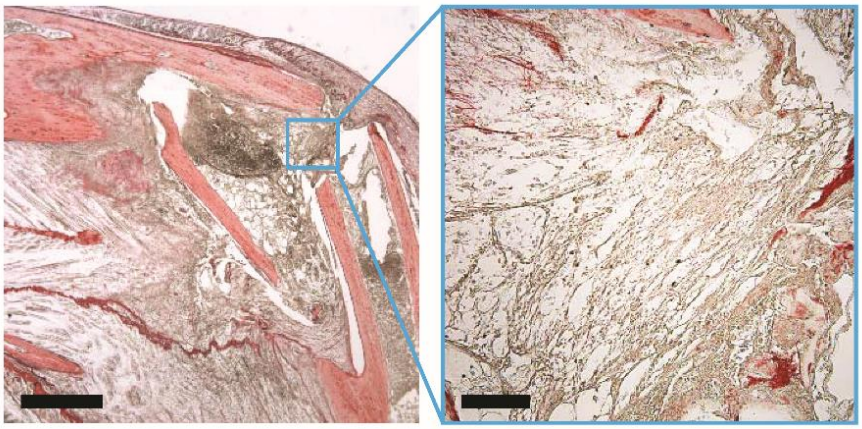

Figure 4.5 – Fracture callus of day 4 mouse
Representative histological section for measurement day 4. Slides were stained with HBQ. Scale bar on the left is 1mm and scale bar on the right is 100µm. Fracture gap at day 8 is primarily composed of granulation and fibrotic tissue.

To understand how |Z| and θ vary with changing tissue composition of fracture calluses, we performed linear regression analyses to compare them to fraction volumes of cartilage, trabecular bone, fibrous tissue, and marrow space with respect to total callus volume (Table 4.1). At all measured frequencies, |Z| has a positive relationship with % trabecular bone and % marrow space and a negative relationship with % cartilage and % fibrous tissue. The opposite relationships are found when comparing θ to these same tissue volume fractions. These correlations are most substantial at 500 kHz, with both |Z| and θ showing significant relationships with % cartilage and % trabecular bone (Fig. 4.6). At 1 MHz, θ also has a significant correlation with % cartilage (R^2 = 0.75, $p < 0.01$), % trabecular bone (R^2 = 0.68, $p < 0.01$), % fibrous tissue (R^2 = 0.41, $p = 0.02$), and % marrow space (R^2 = 0.58, $p < 0.01$). In addition, θ becomes more negative significantly with % trabecular bone below 5 kHz ($R^2 > 0.25$, $p < 0.05$) and above 100 kHz ($R^2 > 0.32$, $p < 0.05$).

Table 4.1 – Fraction of tissue types in individual calluses

Amounts of cartilage, trabecular bone, cortical bone, fibrous tissue, muscle, and marrow space presented for each callus sample as a percentage of the total callus volume.

Sample	% Cartilage	% Trabecular Bone	% Cortical Bone	% Fibrous Tissue	% Muscle	% Marrow Space
Day 8: M4	53.41	0.00	3.17	39.51	4.15	0.00
Day 8: M5	67.07	0.00	0.00	25.75	5.99	0.00
Day 8: M6	83.54	0.37	0.00	16.09	0.00	0.00
Day 8: M7	72.01	0.00	0.00	27.99	0.00	0.00
Day 14: M1	14.58	20.19	12.71	17.01	1.50	34.58
Day 14: M2	27.94	18.86	11.03	18.33	1.42	22.95
Day 14: M3	22.05	18.46	10.77	24.36	0.77	23.72
Day 14: M4	33.83	17.29	6.51	22.09	1.07	19.21
Day 21: M1	0.24	29.53	11.88	6.00	2.12	50.35
Day 21: M2	2.27	38.64	14.77	3.64	0.00	40.91
Day 21: M3	1.90	32.83	4.74	0.00	0.00	60.34
Day 21: M4	1.02	38.03	3.71	1.28	0.00	55.57
Day 21: M5	0.00	45.89	4.24	7.16	0.53	41.91
Avg ± StdDev						
Day 8	69.01 ± 12.48	0.09 ± 0.19	0.79 ± 1.59	27.34 ± 9.62	2.54 ± 3.02	0.00 ± 0.00
Day 14	24.60 ± 8.23	18.70 ± 1.20	10.26 ± 2.64	20.45 ± 3.38	1.19 ± 0.34	25.12 ± 6.61
Day 21	1.09 ± 1.00	36.984 ± 6.24	7.87 ± 5.10	3.62 ± 3.03	0.53 ± 0.92	49.82 ± 8.46

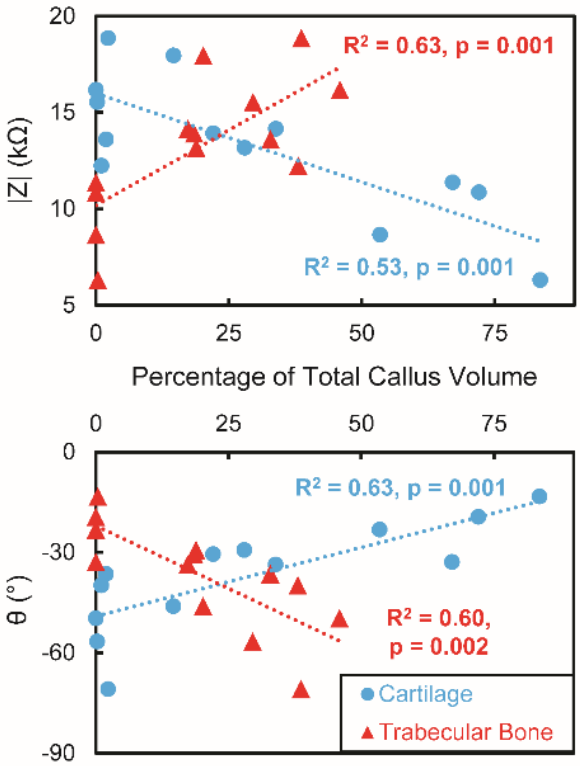

Figure 4.6 – Impedance correlates with tissue composition

Impedance magnitude and phase at 500 kHz correlated with percent cartilage and percent trabecular bone of the total callus volume (N=13). |Z| has a significant negative trend with % trabecular bone and positive trend with % cartilage, with opposite trends in θ.

Finally, we split our samples into a model group and test group to determine predictive power. Even with a reduced N of 7 callus samples, regression analyses still suggested correlations between impedance measurements and % cartilage and % trabecular bone, shown in Fig. 4.7. Errors between model-predicted values and true values averaged between 8-25% tissue volume across the three times we conducted this assessment. The model built from |Z| consistently performed better, producing 3-5% less error than the model built from θ.

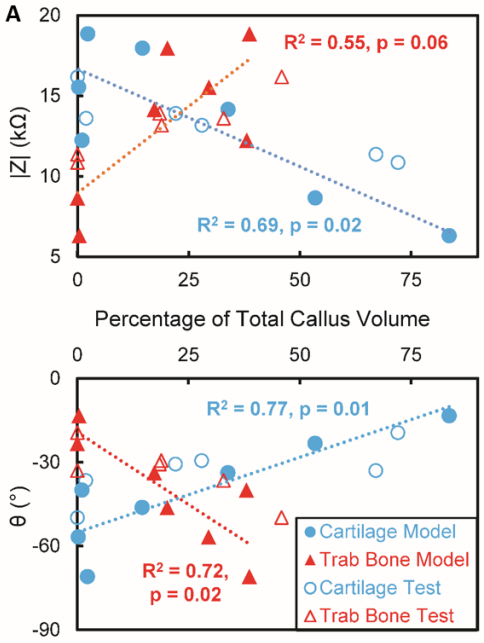

B

		|Z| Model		θ Model	
Test Mouse	Day	Error (%C)	Error (%T)	Error (%C)	Error (%T)
#1	8	23.49	11.22	25.87	13.20
#2	8	24.22	8.84	5.68	0.14
#3	14	0.81	0.73	19.90	9.11
#4	14	0.60	4.56	23.49	7.52
#5	21	23.28	11.23	32.66	16.18
#6	21	4.00	12.35	9.89	16.44
Average		12.73	8.15	19.58	10.43
Standard Dev.		12.04	4.58	10.13	6.21

Figure 4.7 – Predictive model of tissue composition
(A) Samples were split into a first group (N=7) from which to build a model and a test group (N=6). Impedance magnitude and phase at 500 kHz are plotted against percent cartilage and percent trabecular bone of the total callus volume for the model group with solid markers. These are fit with a linear model, and the trendline as well as associated R^2 and p-values are shown. The test group measurements are plotted with unfilled markers. **(B)** The error was calculated for each test mouse as the absolute difference between the true % tissue (C = Cartilage, T = Trabecular Bone) and the estimated value from both models (one created from |Z|, the other from θ). On average the models result in % tissues that are 8-25% off from the true value determined by stereology.

4.5 Discussion

Cadaver and murine *ex vivo* testing demonstrated the ability of EIS to distinguish between hematoma, cartilage, and bone tissues reflective of fracture healing stages.

4.5.1 Cadaver study: Impedance distinguishes tissues dominant in fracture healing

By measuring impedance across blood, cartilage, trabecular bone, and cortical bone, we can understand our system's ability to distinguish between relevant tissues involved in fracture repair. Measurements clearly differ between tissue types, with distinct shapes of frequency responses highlighting our capacity to objectively classify tissue types dominant in fracture healing. However, because irregularly shaped tissues were placed on flat surface electrodes, measurement variations were observed due to electrical contact issues, particularly for stiffer bone tissues. In future *in vivo* studies with well-integrated electrodes, variance is expected to decrease substantially.

Next, we tested the sensitivity of EIS to capture differences in healing stages when electrodes were drilled into bone rather than in direct contact with callus tissue. This approach also alleviates concerns regarding variation in electrode-tissue contact arising from isolated tissue measurements (above). In our simulated fracture model, we found that impedance across a fracture gap filled with cartilage (Stage 2) was significantly different from one filled with trabecular bone (Stage 3). In this model, since electrodes were inserted in higher-impedance cortical bone ends, it is important to note that measurements reflected the relatively lower-impedance tissues in the gap. We also confirmed that heterogeneous mixtures of cartilage and trabecular bone produced characteristics between the two individual tissues. While these heterogeneous mixtures were created *ex vivo* and therefore lacked biological integration, they were reasonable approximations of the pockets of cartilage and trabecular bone found in calluses transitioning from Stage 2 to 3 of healing (as seen in Fig. 4.4A, Day 14 histology). These results indicate that our system can distinguish between the cartilaginous and trabeculated bone phases of the healing process, and therefore may be able to detect when a fracture is not transitioning normally through endochondral ossification.

To determine translatability of our device to clinical settings when fractures are surgically fixed, we tested the impact of a metal bone plate and screws on impedance measurements. Our data indicates that the bone plate does not have a perceptible effect on our data, and instead shows that it is difficult for signal to pass from the bone to the plate (red path in Fig. 4.3A), likely because the plate is never fully flush against the bone. However, addition of bone screws resulted in a dramatic decrease in |Z| across the two electrodes, suggesting that they provide a lower resistance path for the signal to travel (black path in Fig 4.3A). This effect is a function of geometry – if the bone screws are far from the sensor electrodes relative to the distance between the electrodes (true in most clinical situations), our measurements should not be significantly affected and signal will travel through the ideal path directly between the electrodes (blue path in Fig. 4.3A). These results can be used to inform future design considerations.

4.5.2 Mouse study: Impedance correlates to heterogeneous callus composition

This *ex vivo* mouse study allowed us to evaluate the ability of EIS to distinguish between fracture calluses made up of a heterogeneous mix of tissues. Our results indicate an upward trend of |Z| over healing time as expected, with θ following trends derived from our cadaver model analysis. These results indicate that we may be able to detect when recovery is plateauing in the case of delayed- or non-union.

Associating specific |Z| and θ measurements to each respective fracture callus and its exact tissue composition provides us with even more detailed information. While averaging data at each time point across all study mice indicates measurement differences over the course of healing, quantitative histomorphometric analysis can account for differences in healing rates among the study mice.

Our analysis showed that for all measured frequencies, there are negative relationships between |Z| and % cartilage as well as % fibrous tissue, and positive relationships between |Z| and % trabecular bone as well as % marrow space. These correlations are expected – |Z| rises over the course of healing as more conductive tissue (cartilage) is remodeled into more resistive tissue (bone). % fibrous tissue decreases with healing time as it is replaced by trabecular bone or marrow space. θ exhibits positive relationships with % cartilage and % fibrous tissue, also as expected. Since cartilage has relatively high water content and fibrous tissues contain mostly collagen fibers with few cells, these two tissue types have a greater resistive component than capacitive component, leading θ to become less negative (more resistive) with higher percentages of these tissues. On the other hand, bone is made up of layers of mineralized matrix with low water content and marrow space is responsible for producing many kinds of cells (erythrocytes, leukocytes, and platelets). Because matrix layers and cell membranes can be modeled as capacitors, these two tissue types have a greater capacitive component than resistive component, leading θ to become more negative (more capacitive) with higher percentages of these tissues.

Our results are consistent with previous findings that describe an increase in |Z| over healing time[18–20,22,25]. However, our study provides more comprehensive information about the behavior of θ as a function of frequency and time. While |Z| reflects conductivity of tissue, θ reflects the resistive or capacitive nature, and together their frequency response curves complement each other. Thresholds for both parameters can be set to determine the stage of healing, providing more confidence in our classification. We also related impedance measurements to histomorphometry, which has not previously been shown and will enable future predictive modeling. By splitting our samples into a model group and test group, we were able to consider this potential predictive power. Errors of 8-25% tissue volume even with reduced N indicate that our model has potential for

accurate assessment of tissue composition, although additional studies will allow us to fully demonstrate predictive power of this technique. We believe this is the first quantitative evaluation of how well impedance predicts fracture tissue composition.

4.5.3 Limitations

The main limitation of this analysis was the use of dissected tissues from euthanized mice, so there was error introduced with electrode placement at the time of data collection. In addition, *ex vivo* tissue samples are not as hydrated as in an *in vivo* condition. Our experimental set-ups were flushed with saline to mimic a physiologic setting, but hydration in an *in vivo* environment differs. While the role of contact impedance may be important in this study, our results offer support for the use of EIS to track fracture healing and perform early detection of nonunion. Continued development of sensors for an *in vivo* model would permit an environment where fracture tissue can surround electrodes with reliable electrical contact. Though impedance measurements are set-up dependent (e.g. change with electrode size), we expect the relative changes in impedance due to fracture healing to be preserved from sample to sample.

4.6 Future directions and conclusion

As micro- and nanofabrication technology has evolved, minimal modifications are necessary to incorporate sensors into existing implants that feature wireless capabilities.[39] Smart implant technology developed for orthopaedics has been mainly limited to strain gauges and other mechanical measurements; we believe EIS measurements can provide more sensitive information about the earliest changes in fracture healing. Additional improvements such as arraying multiple electrodes across the fracture gap to obtain spatial information[26] could be considered. This technology has potential to be a more affordable, radiation-free method to monitor fracture healing

as compared with other techniques like X-ray and CT scans, and can be used in parallel with current standards of care.

In conclusion, we have demonstrated the feasibility of EIS for detecting fracture callus composition, highlighting its potential as a method for early detection of bone healing and fracture nonunion. Future studies will work to measure *in vivo* changes in impedance longitudinally in mice and eventually human patients to recognize patterns that are typical of "normal" and delayed fracture healing to understand the sensitivity of EIS compared to standard radiographic techniques. From the results presented in this paper, we expect |Z| to increase steadily over time until healing is achieved, at which point it will plateau. θ is expected to become less negative at lower frequencies and more negative at higher frequencies. We believe that using these measurements, as well as pole and zero values extracted from transfer function fits, will enable accurate assessment of fracture healing *in vivo*. To best demonstrate utility of this technique, future results should be correlated with biomechanics, histology, and radiography.

4.7 References

1. Lu, C., Meinberg, E., Marcucio, R. & Miclau, T. Fracture repair and bone grafting. *OKU 10 Orthop. Knowl. Update* 11–21 (2011).

2. American Academy of Orthopaedic Surgeons. *The Burden of Musculoskeletal Diseases in the United States*. 1–8 (Bone and Joint Decade, 2008).

3. Morshed, S. Current Options for Determining Fracture Union. *Adv. Med.* **2014,** 1–12 (2014).

4. Whiley, S. P. Evaluating fracture healing using digital x-ray image analysis. *Contin. Med. Educ.* **29,** 102 (2011).

5. Protopappas, V. C., Vavva, M. G., Fotiadis, D. I. & Malizos, K. N. Ultrasonic monitoring of bone fracture healing. *IEEE Trans. Ultrason. Ferroelectr. Freq. Control* **55,** 1243–1255 (2008).

6. Dickson, K. F., Katzman, S. & Paiement, G. The importance of the blood supply in the healing of tibial fractures. *Contemp. Orthop.* **30,** 489–493 (1995).

7. McKibbin, B. The Biology of Fracture Healing in Long Bones. *J. Bone Jt. Surg.* **60-B,** 150–162 (1978).

8. Frost, H. M. The biology of fracture healing: an overview for clinicians. Part I. *Clin. Orthop.* **248,** 283–293 (1989).

9. Blokhuis, T. J. *et al.* The reliability of plain radiography in experimental fracture healing. *Skeletal Radiol.* **30,** 151–156 (2001).

10. Watanabe, Y., Nishizawa, Y., Takenaka, N., Kobayashi, M. & Matsushita, T. Ability and Limitation of Radiographic Assessment of Fracture Healing in Rats. *Clin. Orthop.* **467,** 1981–1985 (2009).

11. Stoy, R. D., Foster, K. R. & Schwan, H. P. Dielectric properties of mammalian tissues from 0.1 to 100 MHz; a summary of recent data. *Phys. Med. Biol.* **27,** 501 (1982).

12. Jongschaap, H., Wytch, R., Hutchison, J. & Kulkarni, V. Electrical impedance tomography: a review of current literature. *Eur. J. Radiol.* **18,** 165–174 (1994).

13. Dean, D. A., Ramanathan, T., Machado, D. & Sundararajan, R. Electrical impedance spectroscopy study of biological tissues. *J. Electrost.* **66,** 165–177 (2008).

14. Gabriel, S., Lau, R. & Gabriel, C. The dielectric properties of biological tissues: II. Measurements in the frequency range 10 Hz to 20 GHz. *Phys Med Biol* **41,** 2251–2269 (1996).

15. Ciuchi, I., Curecheriu, L., Ciomaga, C., Sacdu, A. & Mitoseriu, L. Impedance Spectroscopy characterization of bone tissues. *J. Adv. Res. Phys.* **1,** (2010).

16. Schaur, S., Jakoby, B. & Kronreif, G. Position-dependent characterization of bone tissue with electrical impedance spectroscopy. in *IEEE Sensors* (2012).

17. Khan, M., Sirdeshmukh, S. P. S. M. A. & Javed, K. Evaluation of bone fracture in animal model using bio-electrical impedance analysis. *Perspect. Sci.* **8,** 567–569 (2016).

18. Yoshida, T. *et al.* Measurement of bone electrical impedance in fracture healing. *J. Orthop. Sci.* **14,** 320–329 (2009).

19. Hirashima, T., Kim, W. C., Kawamoto, K., Yoshida, T. & Kubo, T. Evaluating Bone Union of Distal Radius Fractures by Measuring Impedance Values. *Orthopedics* **32,** 31–33 (2009).

20. Yoshida, T., Kim, W. C., Oka, Y., Yamada, N. & Kubo, T. Assessment of distraction callus in rabbits by monitoring of the electrical impedance of bone. *Acta Orthop.* **81,** 628–633 (2010).

21. Kumaravel, S. & Sundaram, S. Monitoring of fracture healing by electrical conduction: A new diagnostic procedure. *Indian J. Orthop.* **46,** 384 (2012).

22. Gupta, K. *et al.* Changes in electrical properties of bones as a diagnostic tool for measurement of fracture healing. *Hard Tissue* **2,** 3 (2013).

23. Kulkarni, V., Hutchison, J., Ritchie, I. & Mallard, J. Impedance imaging in upper arm fractures. *J. Biomed. Eng.* **12,** 219–227 (1990).

24. Ritchie, I. & Kulkarni, V. Impedance osteography: clinical applications of a new method of imaging fractures. *J. Biomed. Eng.* **12,** 369–374 (1990).

25. Kozhevnikov, E. *et al.* Electrical impedance spectroscopy – a potential method for the study and monitoring of a bone critical-size defect healing process treated with bone tissue engineering and regenerative medicine approaches. *J Mater Chem B* **4,** 2757–2767 (2016).

26. Swisher, S. L. *et al.* Impedance sensing device enables early detection of pressure ulcers in vivo. *Nat. Commun.* **6,** 6575 (2015).

27. Lin, M. C., Herfat, S. T., Bahney, C. S., Marmor, M. & Maharbiz, M. M. Impedance spectroscopy to monitor fracture healing. in *IEEE Engineering in Medicine and Biology Conference.* 5138–5141 (2015).

28. Kilkenny, C., Browne, W. J., Cuthill, I. C., Emerson, M. & Altman, D. G. Improving Bioscience Research Reporting: The ARRIVE Guidelines for Reporting Animal Research. *PLOS Biol.* **8,** e1000412 (2010).

29. Bonnarens, F. & Einhorn, T. A. Production of a standard closed fracture in laboratory animal bone. *J. Orthop. Res.* **2,** 97–101 (1984).

30. Auer, J. A. *et al.* Refining animal models in fracture research: seeking consensus in optimising both animal welfare and scientific validity for appropriate biomedical use. *BMC Musculoskelet. Disord.* **8,** 72 (2007).

31. Thompson, Z., Miclau, T., Hu, D. & Helms, J. A. A model for intramembranous ossification during fracture healing. *J. Orthop. Res.* **20,** 1091–1098 (2002).

32. Marsell, R. & Einhorn, T. A. The biology of fracture healing. *Injury* **42,** 551–555 (2011).

33. Hiltunen, A., Vuorio, E. & Aro, H. T. A standardized experimental fracture in the mouse tibia. *J. Orthop. Res. Off. Publ. Orthop. Res. Soc.* **11,** 305–312 (1993).

34. Manigrasso, M. B. & O'Connor, J. P. Characterization of a Closed Femur Fracture Model in Mice : Journal of Orthopaedic Trauma. *J Orthop Trauma* **18,** 687–695 (2004).

35. Altunkaynak, B. Z., Altunkaynak, E., Unal, D. & Unal, B. A Novel Application for the Cavalieri Principle: A Stereological and Methodological Study. *Eurasian J. Med.* **41,** 99–101 (2009).

36. Gundersen, H. J. G. *et al.* Some new, simple and efficient stereological methods and their use in pathological research and diagnosis. *APMIS* **96,** 379–394 (1988).

37. Mey, K. H., Sørensen, M. S. & Homøe, P. Histomorphometric Estimation of Air Cell Development in Experimental Otitis Media. *The Laryngoscope* **116,** 1820–1823 (2006).

38. Müller, R. *et al.* Morphometric analysis of human bone biopsies: a quantitative structural comparison of histological sections and micro-computed tomography. *Bone* **23,** 59–66 (1998).

39. Ledet, E. H. *et al.* Implantable sensor technology: from research to clinical practice. *J. Am. Acad. Orthop. Surg.* **20,** 383–392 (2012).

Chapter 5: Development of smart bone plates to monitor fracture repair

This chapter is based largely on the following work with permission from:

(1) Monica C. Lin, Diane Hu, Frank Yang, Safa T. Herfat, Chelsea S. Bahney, Meir Marmor, Michel M. Maharbiz. Using impedance to track fracture healing rates in mice in vivo: A pilot study. in *IEEE Engineering in Medicine and Biology Conference*. 1724–1727 (2017). doi:10.1109/EMBC.2017.8037175

(2) Monica C. Lin, Diane Hu, Meir Marmor, Safa T. Herfat, Chelsea S. Bahney*, Michel M. Maharbiz*. Smart bone plates can monitor fracture healing. *bioRxiv* 366039 (2018). doi:10.1101/366039

M.C.L., M.M., S.T.H., C.S.B., and M.M.M. designed the research study, and M.C.L., D.H., C.S.B. and F.Y. performed the rodent surgeries. M.C.L. collected and analyzed the data and drafted the manuscripts, while M.M., S.T.H., C.S.B., and M.M.M. provided conceptual advice and critically revised the papers. M.C.L., M.M., S.T.H., C.S.B., and M.M.M. prepared supporting grants. The work in this chapter was funded by the National Science Foundation under grant EFRI-1240380 and the Center for Disruptive Musculoskeletal Innovations under grant IIP-1361975, and aided by a grant from the Orthopaedic Trauma Association.

5.1 Abstract

There are currently no standardized methods for monitoring fracture healing. While histological studies can clearly identify the tissues found in the four stages of repair, in practice surgeons rely on X-ray, which is only useful at later stages of healing after mineralization has occurred. As electrical impedance spectroscopy (EIS) has previously been used to distinguish tissue types

during healing, we hypothesized that microscale sensors embedded in the fracture callus could track the changing tissue with high sensitivity. Using *in vivo* mouse fracture models, we present the first evidence that microscale instrumented implants provide a route for post-operative fracture monitoring. In this study, we implanted sensors in mouse long bone fractures fixed with either external fixators or bone plates. EIS measurements taken across two electrodes implanted in the fracture gap were able to track longitudinal differences between individual mice with proper healing and mice experiencing poor healing. We additionally present an equivalent circuit model that combines the EIS data in order to classify healing states of fractures. Lastly, we show that EIS measures are strongly correlated with standard μCT measures of healing and that these correlations validate clinically-relevant operating frequencies for implementation of this technique. Data from these two models demonstrate that this technique can be translated to the clinic through integration into current fracture management strategies such as bone plating, providing physicians with quantitative information about the state of a fracture to guide clinical decision-making for patients.

5.2 Introduction

Musculoskeletal injuries are among the most disabling and costly conditions in the United States, with the total number of bone fractures ranging from 12 to 15 million per year[1]. Treatment of these fractures represents a significant burden on the U.S. healthcare system, with hospitalization costing an estimated $23.4 billion in 2004[2]. Determining when a fracture is healed is crucial to making correct clinical decisions for patients, but a survey of over 400 orthopaedic surgeons revealed that there is no consensus in defining both clinical and radiographic criteria for outcome measures[3]. Multiple studies cite the lack of standardized methods for assessing fracture union[4–6].

Radiographic imaging and clinical evaluation are the two standard methods of monitoring bone fracture healing in the clinic. Plain X-ray radiographs are often used to assess fractures, but studies

have shown that these correlate poorly with bone strength, do not define union with enough accuracy, and are unreliable for determining the stage of fracture repair. Other radiographic techniques such as computed tomography (CT), dual energy X-ray absorptiometry (DEXA), and ultrasound can offer improved diagnostic capabilities but have limited use in the clinic due to cost, high radiation dose, decreased accuracy around metal implants, or dependence on operator expertise.[7,8] New monitoring tools include mechanical assessment and serologic markers, but these technologies are still under development and tend only to be used in academic research settings[3]. In addition, mechanical tests typically rely on a patient to be weight-bearing, limiting their utility in understanding early stages of healing[9]. Using serologic biomarkers as early predictors of fracture healing offers great promise, but appropriate markers correlating to the biological progression of healing have not yet been identified[10]. As such, physical examination by a physician is still the most relied upon technique to determine progression of fracture healing. Patients are examined for local signs of infection, ability to weight-bear, localized tenderness to palpation, and extent of pain. However, patient-reported questionnaires result in imprecise assessments, and physician evaluation is subjective and depends on experience[3].

Fracture healing proceeds through a combination of two different pathways: intramembranous (direct) and endochondral (indirect) ossification[11,12]. At the onset of fracture injury, formation of a hematoma around the trauma contains the fracture debris and initiates a pro-inflammatory cascade (Stage 1)[13,14]. Following this, the primary healing pathway is largely determined by stability at the fracture site. In highly stable areas, cells originating from the endosteum and periosteum undergo intramembranous ossification to directly form osteoblasts (bone)[15,16]. However, within the fracture gap, new bone forms indirectly through endochondral ossification, where periosteal progenitor cells undergo chondrogenic differentiation to form a cartilage

intermediate (Stage 2)[15,17]. Hypertrophic maturation of chondrocytes then promotes mineralization and leads to conversion into trabecular bone (Stage 3)[18], and finally remodels into functional cortical bone (Stage 4). These four defined stages of healing are well characterized histologically[12,18,19], but early stages in particular are not detectable by standard methods of monitoring like X-ray that rely on mineralization of bone.

Monitoring fracture healing is an area of active academic research, but most work has focused around obtaining mechanical feedback correlating strain measurements to bone strength[20,21]. In this study, we utilize electrical techniques to characterize progression of fracture repair, building on previous work that has measured electrical changes in cells and tissue[22–24]. Electrically, tissue can be modelled as a combination of resistive and capacitive effects. The ion-rich intra- and extracellular matrices conduct charge and thus can be modeled as resistances, while double-layered cell membranes act as barriers to charge flow and can be modeled as capacitances or constant phase elements (CPE)[25]. Electrical impedance spectroscopy (EIS) measures the frequency-dependent combination of these components, describing opposition to the flow of electrical current through a material. Complex impedance Z can be expressed in polar form as

$$Z = |Z|e^{j\theta} \qquad (1)$$

with magnitude $|Z|$ and phase angle θ, or in Cartesian form as

$$Z = R + jX \qquad (2)$$

with resistance R and reactance X.

There is an extensive body of literature[25–28] demonstrating the use of this so-called "bioimpedance" method to quantitatively characterize cellular changes, primarily reflecting cell membrane integrity, cell volumes, and the conductivity of intra- and extracellular components[28]. Previous work has also detailed the use of impedance spectroscopy to describe many biological tissues[28–31],

including the dielectric and conductive properties of porous and dense bone[32–34]. We have also previously shown the feasibility of using EIS to distinguish tissue composition within the fracture callus using *ex vivo* model systems[35,36]. In addition, prior work has used EIS to evaluate bone fractures in *ex vivo* and *in vivo* models[37–42], but suffers from restricted detection due to noise from surrounding soft tissue, limited sensitivity due to electrode placement, and inadequate histological analysis.

Here, we present the development and testing of microscale EIS sensors designed to measure the electrical properties of the fracture callus longitudinally during healing in clinically relevant murine fracture models. To our knowledge, this is the first study to implant microscale sensors directly in the fracture gap, enabling local measurements of the changing fracture callus. We first validated the ability of our sensors to distinguish between healing and non-healing fractures in an external fixator model, where tibia defects were stabilized using a miniaturized Ilizarov external fixator. We then applied this technique to a bone plate model, where femur fractures were stabilized internally with a bone plate. Using the translationally relevant bone plate model where electrodes are embedded within fracture gaps, we find that the frequency spectra of impedance measurements are robustly correlated with quantified measures of bone volume and bone mineral density. Furthermore, this data demonstrates the use of EIS as a simple and low-cost method to provide clinically relevant information over the course of fracture healing, which can be readily integrated into clinical flows for fracture management, such as bone plates. With the global orthopaedic devices market expected to reach $41.2 billion by 2019[43], we believe there is vast potential for a smart implant and present this study as validation of EIS for integration into fracture management.

5.3 Methods

5.3.1 Study design

Our goal for this study was to assess the feasibility of EIS as a quantitative tool to monitor fracture healing. From previous studies, we hypothesized that EIS measurements would correlate well with biological indicators of healing, such as callus composition, X-ray radiographs, and μCT indices (i.e. bone mineral density). We conducted a controlled laboratory experiment in a murine fracture model, stabilizing fractures with an external fixator or bone plate and inserting custom sensors in the fracture gap. Euthanasia time points were selected to provide information about callus composition over the course of healing.

5.3.2 Impedance measurement system

Two-point impedance measurements were taken at the following frequencies (Hz): 20, 100, 1k, 5k, 10k, 15k, 25k, 50k, 75k, 100k, 250k, 500k, 750k, 1M. Impedance magnitude (|Z|) and phase (θ) were recorded from an Agilent E4980AL Precision LCR Meter with a 100 mV sine wave output signal, and converted to electrical resistance (R) and reactance (X). 100 mV was chosen to be below the threshold for electrolysis of water, and as high as necessary to obtain good signal-to-noise ratio. At each measurement time point, data was averaged over three sets of measurements taken for each sample, with each set involving 5 impedance measurements at the 14 frequencies listed above.

5.3.3 Sensor development

External Fixator Model:

250 μm diameter sensor pins were fabricated using an FR4 (a glass-reinforced epoxy laminate material) substrate with electroless nickel immersion gold (ENIG) plated electrodes (127 μm diameter) spaced 500 μm apart (PCB Universe, Vancouver, WA). Smaller sensors were then made

for a subsequent study to minimize disruption of healing. 25.4 μm diameter platinum (Pt) wires insulated with 1.27 μm isonel (A-M Systems, Sequim, WA) were used to create sensors small enough for implantation in a fracture model involving the mouse tibia, which is approximately 1 mm in diameter. Two wires were cut to roughly 50 mm in length, and recording sites were exposed by burning off short 175 μm sections of insulation in the center of each wire using a CO_2 laser. The two wires were offset so the electrodes were spaced 0.5 mm apart, then twisted together to form a single sensor. The wires were coiled on either side of the electrodes to allow for strain relief.

Bone Plate Model:

Flexible sensors were fabricated on 115 μm thick polyimide (AltaFlex, Santa Clara, CA) to be affixed to the bone plate. Epo-Tek H20E silver (Ag) epoxy (Epoxy Technology, Inc., Billerica, MA) was used to conductively adhere 25.4 μm diameter Pt wires to ENIG-plated pads on the polyimide sensor board. These Pt wires were attached at the center of the bone plate to serve as electrodes directly in the fracture gap. A long serpentine cable extended from the proximal end of the plate, leading to a set of connection pads that interfaced with our measurement instrumentation. The entire sensor was then coated with 6-15 μm of Parylene-C at room temperature through a chemical vapor deposition process using an SCS Labcoter® 2 Parylene Deposition System (Specialty Coating Systems, Indianapolis, IN) as an insulator and for biocompatibility. A sharp razor blade was used to cut off the ends of the Pt wires to expose recording sites (700 μm^2) spaced 0.5 mm. Medical-grade Epo-Tek 353ND epoxy was used to attach the two Pt wires and to secure the polyimide board to the proximal half of the bone plate.

Prior to implantation, fixation instrumentation was autoclaved and sensors were sterilized by immersing in 70% EtOH under ultraviolet light for at least 1 hour.

5.3.4 Mouse models of fracture repair

Approval was obtained from the University of California, San Francisco (UCSF) Institutional Animal Care and Use Committee (IACUC) prior to performing these mouse studies, and this report adheres to ARRIVE Guidelines for reporting animal research[44]. Rodent models of fracture repair have been used since 1984[45] and are well-established as preclinical models that provide insight into human fracture healing[46]. Mice were housed in cages (≤5 mice/cage) with paper/cellulose bedding and easy access to food and water, and were monitored for signs of stress (low activity, unkempt fur, weight loss). For both models below, mice were anesthetized with an intraperitoneal (IP) injection of ketamine:dexmedetomidine (1:1) for surgery, and revived with an IP injection of atipamezole. For pain relief, buprenorphine was injected subcutaneously immediately following surgery, and subsequently at four and twenty four hours post-surgery per the IACUC protocol. Mice were given a prophylactic dose of enrofloxacin antibiotic following surgery and an additional dose on the subsequent two days.

External Fixator Model:

Fractures were made in the mid-diaphyses of wild-type C57BL/6J mice (male, 22-29g, 12-16 weeks old) and stabilized using custom-designed external fixators. The healing timeline for this model has been previously examined in detail[47]. Sensors were carefully placed in the fracture gap, with skin sutured closed around the ends of the sensors, leaving wire ends available for connection to measurement instrumentation. Mice were anesthetized twice weekly using isoflurane mixed with oxygen to track healing progression with impedance measurements on days 0, 4, 7, 11, 14, 18, 21, 25, and 28. A thin, rigid acrylic sheath was placed over the external fixator to protect the sensor in between measurements. Eleven mice were implanted with 250 μm sensor pins in two different models of post-injury tissue changes – a 2 mm defect was created by an osteotomy (N=5)

and a 0.5 mm defect was created by slight distraction of the proximal and distal bone ends (N=6). A 1 V sine wave output signal was used for this study. Mice were euthanized at days 7 (N=4), 14 (N=4), and 28 (N=3) for histology to reflect varying degrees of healing. Six mice were implanted with thin 56 μm Pt wire sensors in a 0.5 mm defect; 1 mouse was found dead on day 4 and taken out of the study. Mice were euthanized at day 28 for histology to allow for healing to progress to a late enough time point to diagnose proper healing or lack of healing.

Bone Plate Model:

Ten wild-type C57BL/6J mice (male, 24-33g, 12-20 weeks old) had their right femurs stabilized with Titanium bone plates (RISystem, Davos, Switzerland), and defects (<0.25 mm wide) were made with a single cut of a Gigly saw in the mid-diaphysis. The progression of healing with this model has been previously examined in detail[48,49]. Two 700 μm^2 electrodes spaced 0.5 mm apart were centered in the fracture gap. Surgery was performed on eight additional mice, placing a bone plate and sensor but without making a fracture, to serve as controls. In these mice, the two electrodes were placed beside the bone and the surrounding muscle was sutured over it. While infection was not a major issue, the mice had a tendency to chew or otherwise damage the connector outside the animal. To prevent this, mice were singly housed and a stretchable serpentine cable was tunneled subcutaneously up the back of each mouse, with a small incision made between the shoulder blades as an exit point. Connection pads at this location allowed for connection to measurement instrumentation. The muscle and skin was then sutured closed over the stabilized fracture. To monitor the progression of healing, mice were anesthetized with isoflurane mixed with oxygen three times each week for measurements on days 0, 2, 5, 7, 9, 12, 14, 16, 19, 21, 23, and 26. Mice were euthanized at day 12 (N=4) and day 26 (N=6 fractured, N=8 control) for histology and μCT; these two time points were chosen to reflect the transition from stage 2-3 (day 12 –

mixture of cartilage and trabecular bone) and stage 3-4 (day 26 – dominated by trabecular bone, beginning to remodel). 8 mice were taken out of the study (N=1 fracture at day 12, N=1 fracture at day 26, N=6 control at day 26) because their sensors broke at the serpentine junction due to excessive movement by the animal, as seen in radiographic images and confirmed during dissection.

5.3.5 Radiography

Fluoroscopy images were taken using a Hologic Fluoroscan Premier Encore 60000 C-Arm Imaging System at every measurement time point. Following euthanasia, the femur specimens were harvested and fixed overnight before being transferred to 70% ethanol for scanning. X-ray radiography was performed using a Scanco μCT 50 high-resolution specimen scanner (Scanco Medical AG, Bassersdorf, Switzerland). Specimens were imaged with X-ray energy set to 55 kVp and 109 μA. Orthogonal images were taken first with the plate intact and then again after removing the plate and screws. Orthogonal images of the bones with the plate removed were scored by five orthopaedic surgeons (single-blind assessment) using the modified Radiographic Union Scale in Tibia (RUST) fractures, with each cortex being assigned a number from 1 to 4 (1 = no callus, 2 = callus present, 3 = bridging callus, 4 = remodeled with no visible fracture line) [50]. The anterior cortex was excluded as the sensor typically occluded its view on an X-ray, so total values for each specimen could range from 3 to 12 by adding up the scores on the remaining three cortices. Surgeons were also asked to clinically diagnose the fractures as union (U), nonunion (NU), or suspected nonunion (SNU).

Microcomputed X-ray tomography (μCT) was performed with the entire specimen scanned at an isotropic resolution of 10 μm, with an X-ray tube potential of 55 kVp and X-ray intensity of 109 μA. Integration time was set at 500 milliseconds per projection. After scanning, 3D microstructural

image data was reconstructed using Scanco cone-beam reconstruction algorithm. Density calibration of the scanner was performed using a hydroxyapatite calibration phantom provided by the manufacturer. Structural indices were calculated using Scanco evaluation software (version 6.0; Scanco Medical AG). Using this software, the fracture callus was manually delineated from surrounding tissue at its cortical surface and bone morphology was assessed in the region between the central surgical screws (single-blind assessment). The callus tissue was isolated from preexisting bone by performing manual delineation to exclude the original diaphyseal cortex and its intramedullary space. The bone volume was segmented with a lower threshold of 240 grayscale units and image noise was reduced using a Gaussian filter set at a sigma and support of 0.8 and 1, respectively. Three-dimensional microstructural indices reported include bone volume (BV), total volume (TV), bone mineral density (BMD), trabecular number, trabecular thickness, and trabecular separation. Surface rendered, three-dimensional images were generated using Scanco Ray v4.0 software.

5.3.6 Histology

Samples were fixed immediately after dissection in 4% paraformaldehyde (pH 7.2) overnight at 4°C, then decalcified in Cal-Ex for 48 hours at room temperature after completion of μCT scans. Samples were then processed through serial ethanol dilutions and xylene dehydration, embedded in paraffin, and serial 10 μm sections were collected and stained with Hall's and Brunt's Quadruple (HBQ) stain, which stains cartilage tissue blue and bone red.

5.3.7 Equivalent circuit model

The equivalent circuit models the double-layer impedance at the electrode-electrolyte surface as a constant phase element (CPE_{dl}) in series with the tissue component, and places a capacitor (C_p) in parallel to reflect the parasitic capacitance due to coupling along the two long wire traces leading

from the electrodes to the connector. The tissue component is comprised of a resistor (R_t) and capacitor (C_t) in parallel, in series with another resistor ($R2_t$). R_t represents the ionic intracellular environment, $R2_t$ represents the ionic extracellular environment, and C_t represents the double layer cell membranes. In our model, we held C_p constant at 25 μF, extracted from high-frequency measurements taken with our sensors immersed in Phosphate Buffered Saline (PBS) prior to implantation. The impedance of CPE_{dl} is calculated as

$$Z_{CPE} = 1/Q(j\omega)^{\alpha} \qquad (2)$$

where Q is the numerical value of admittance ($1/|Z|$) at $\omega = 1$ rad/s, ω is the angular frequency, and α is a constant from 0 to 1 (1 representing a perfect capacitor). We held α constant at 0.5, based on low-frequency measurements of our sensors in PBS. From a study characterizing an osseous implant using EIS[51], we hypothesized that the changing impedance in our study would be most reflected in $R2_t$. We thus fit R_t and C_t at an initial time point (day 2) and constrained it at that value over time. We used a custom MATLAB script to fit our data at each time point to this model, interpolating 10 steps in between each time point to guide the mathematical solution and avoid jumping to non-physical values. Extracted $R2_t$ values were normalized as a ratio to day 2.

5.3.8 Statistical analysis

Longitudinal impedance data was normalized to the 2nd measurement time point to allow the injury to stabilize. Univariate linear regression analyses were performed to compare end-point impedance measurements to a number of μCT indices (bone volume/total volume, bone mineral density, trabecular number, trabecular thickness, and trabecular separation). Two-tailed *t*-tests determined whether regression slopes were significantly different than zero, and significance was set at $p < 0.05$.

5.4 Results

5.4.1 Impedance distinguishes fractures vs. critical-sized defects

As a proof-of-concept study to measure impedance of a changing fracture callus over the course of healing, we implanted small sensors into broken tibias stabilized in an external fixator model (Fig. 5.1A). This enabled us to quickly validate our technique using commercially-fabricated sensors protected by the large metal construct of the Ilizarov device that secured the leg. We began by implanting 250 μm diameter FR4 (a glass-reinforced epoxy laminate material) sensor pins (Fig. 5.1B-D) into 0.5 mm (N=6) and 2 mm (N=5) defects to determine if we could distinguish EIS trends between previously established healing versus non-healing fracture models[52–54]. EIS measurements were taken twice a week over a frequency range from 20 Hz to 1 MHz with mice sacrificed on days 7, 14, and 28. Mice with 0.5 mm defect sizes showed evidence of healing with a heterogeneous fracture callus composed primarily of cartilage and new trabecular bone 14 days post-injury (Fig. 5.2A). However, mice with 2 mm defect sizes contained only undifferentiated fibrous tissue within the fracture gap, demonstrative of poor healing at the same time point (Fig. 5.2B). Histology images have been false-colored to aid in interpretation of tissue composition, and original histology images are provided in Fig. S5.1A-B. Electrical resistance (R) over the number of days post-fracture is shown in Fig. 5.2C. Linear regression analyses indicate that there is a significant positive relationship between R and time in the mice with 0.5 mm defects ($p < 0.0001$), while there is no correlative relationship between R and time in the mice with 2 mm defects. By day 28, histology for the 0.5 mm defects show new bone formation, while 2 mm critical-sized defects result in an atrophic nonunion with complete absence of bony bridging.

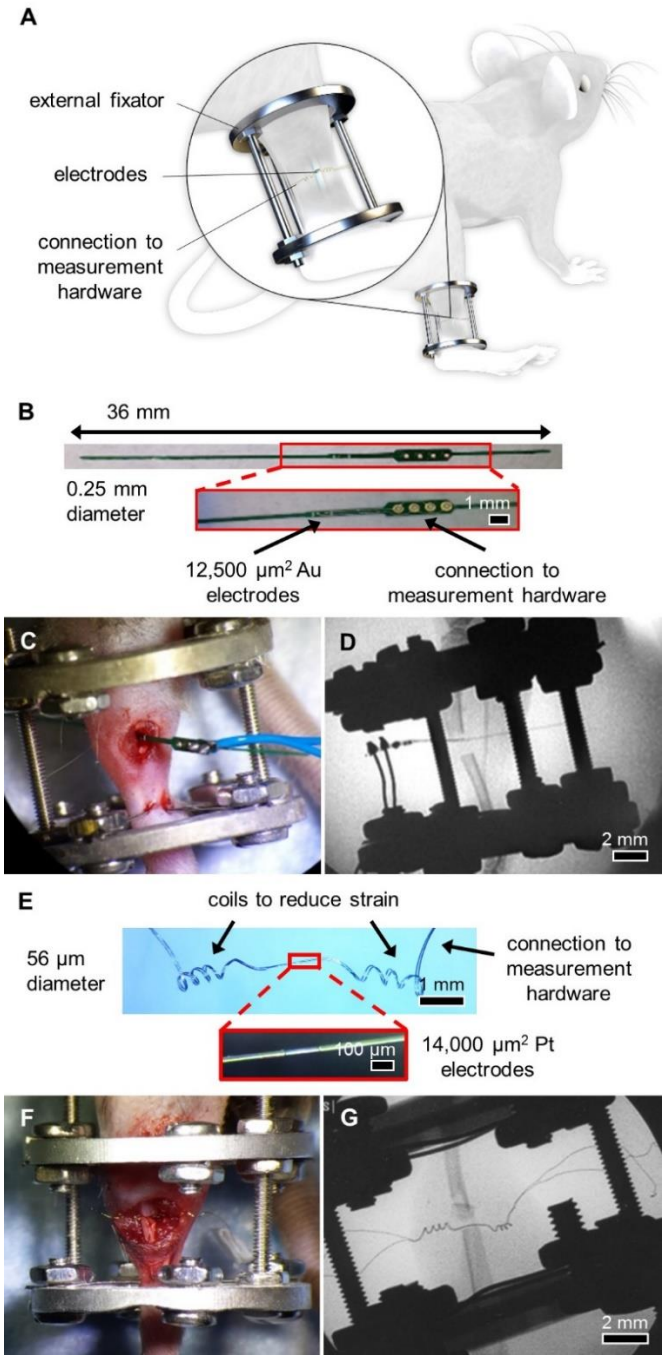

Figure 5.1 – System overview and sensors for an external fixator model

(A) System overview of sensor embedded in mouse tibia fracture, where the injury is stabilized with an external fixator. **(B)** 0.25 mm diameter sensor fabricated on an FR4 substrate, with gold (Au) surface electrodes and large vias outside the leg to connect to measurement hardware. Sensors were implanted in externally-fixed mice tibias with 0.5 mm and 2 mm defects. **(C)** Photograph of open surgery performed to implant 0.25 mm sensor in the external fixator model. Surgical site was closed following sensor placement. **(D)** Fluoroscopy image of implanted 0.25 mm sensor in a 2 mm defect. **(E)** 56 µm diameter sensor assembled using platinum (Pt) wire, with recording sites exposed by a CO_2 laser and coils added to provide strain relief. **(F)** Photograph of open surgery performed to implant 56 µm sensor in the external fixator model. Surgical site was closed following sensor placement. **(G)** Fluoroscopy image of implanted 56 µm sensor in a 0.5 mm defect.

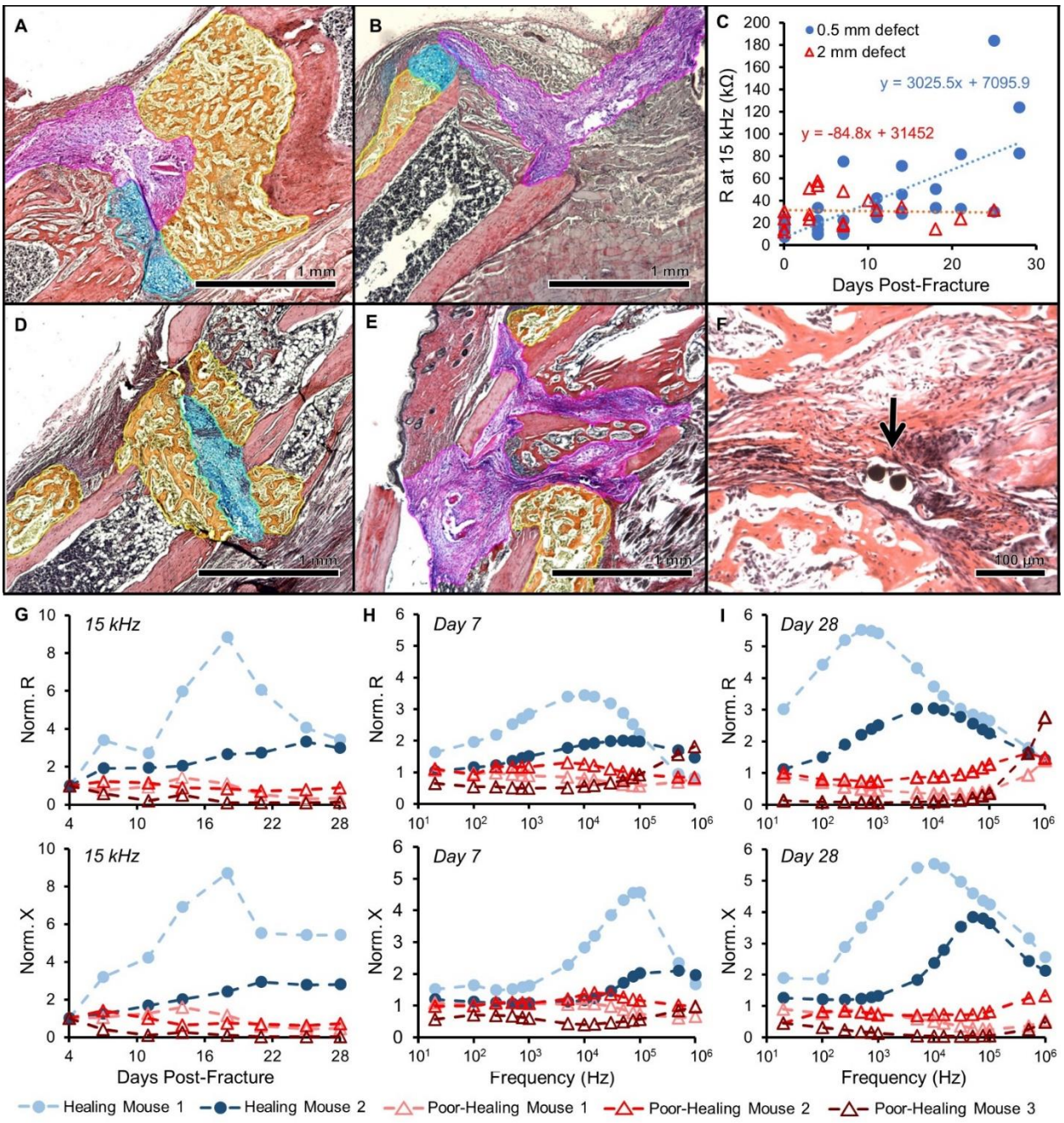

Figure 5.2 – Impedance data distinguishes healing and poorly healing tibia fractures in an external fixator model

Histology sections in this image are stained with Hall's and Brunt's Quadruple (HBQ) stain and false-colored to aid interpretation of tissue composition. Blue = cartilage, yellow = trabecular bone, and purple = fibrous/amorphous tissue. Original red color = cortical bone, black/white area = bone marrow. **(A)** Representative histology section for an externally-fixed 0.5 mm defect at 14 days post-fracture; the fracture gap is clearly bridged by cartilage and new trabecular bone. **(B)** Representative histology section for an externally-fixed 2 mm critical-sized defect at 14 days post-fracture; the fracture gap is dominated by fibrous tissue. **(C)** Electrical resistance (R) at 15 kHz measured with a 250 µm sensor is plotted over days post-fracture for measurements taken in mice with 0.5 mm (N=6) and 2 mm (N=5) defects. Linear regression analyses determined that there is a significant positive relationship in mice with 0.5 mm

defects ($p < 0.0001$), while there is no correlative relationship in mice with 2 mm defects. **(D)** Representative histology section for a healing mouse at 28 days post-fracture; the fracture gap is clearly bridged by cartilage and new trabecular bone. **(E)** Representative histology section for a poor-healing mouse at 28 days post-fracture; the fracture gap contains an overabundance of fibrous tissue. **(F)** Black arrow points to 56 μm sensors fully embedded in fracture tissue. **(G)** Electrical resistance (R) and reactance (X) normalized as a ratio to day 4 plotted over the course of fracture healing at 15 kHz. Normalized R and X both rise steadily over healing time in the healing mice, with stagnant values observed in the poor-healing mice. **(H)** Normalized R and X as a ratio to day 4 plotted over a range of frequencies at day 7 post-fracture. **(I)** Normalized R and X as a ratio to day 4 plotted over a range of frequencies at day 28 post-fracture. Marked shifts in frequency response from day 7 were observed in the healing mice, with limited change occurring in the poor-healing mice.

5.4.2 Microscale sensors track changes in frequency response

One of the limitations of the sensor utilized for the initial validation study was that we consistently noted fibrous tissue surrounding the sensor even out to 28 days post-injury. We hypothesized that this may be due to the large size of the sensor relative to the tibia defect. Consequently, we designed and built significantly smaller electrodes (56 μm diameter platinum) for implantation, measuring roughly an order of magnitude thinner than the original FR4 sensors[55].

Using these 56 μm diameter platinum (Pt) wire electrodes (Fig. 5.1E) implanted within fractures stabilized in the same external fixator model (Fig. 5.1F-G) with 0.5 mm defects, we again measured EIS from 20 Hz to 1 MHz twice per week out to 28 days post-injury in five mice. In two of the mice, histology showed clear signs of healing, with a robust callus present between the two bone ends (Fig. 5.2D). However, the other three mice displayed poor signs of healing, with their fracture gaps dominated by an overabundance of fibrous tissue (Fig 5.2E, original histology in Fig. S5.1C-D). To analyze EIS data as it correlated to histological evidence of healing, electrical resistance (R) and reactance (X) were normalized as a ratio to the first time point after surgery (day 4). This was done to account for the initial perturbation of surgery, variation between sensors and samples, and to enable comparison between multiple mice. Based on all EIS plots, we found the largest spread between measurement days at 15 kHz, indicating that this is the most functional frequency for detecting differences in fracture healing (Fig. 5.2G). This falls within the frequency

range that can be identified as the beta dispersion, which is associated with the polarization of cell membranes, proteins, and other macromolecules[28]. At this frequency, normalized R increases with progression of fracture repair in the healing mice, but stalls in the poor-healing mice as expected. Normalized X rises above 1 over time in healing mice, and below 1 over time in poor-healing mice. Fig. 5.2H-I illustrates how normalized R and X as functions of frequency differ for healing and poor-healing mice from an early time point (day 7) to a late time point (day 28). The healing mice exhibit clear changes in their frequency response in both parameters relative to day 4, especially in the frequency range of 10^3 to 10^5 Hz. Comparatively, non-healing mice show relatively flat frequency responses relative to their initial day 4 behavior. The influence of callus formation on the frequency response of impedance measurements enables the clear differentiation between well-healing and poor-healing mice.

In the poor-healing mice, a large amount of fibrous tissue was noted and we hypothesized this was due to excess movement of the sensor relative to the fractured bone ends. By comparing fluoroscopy images taken immediately after surgery and on day 28 before euthanasia, we can determine whether or not the sensor shifted over time. In the two healing mice, day 28 X-rays showed the sensor remained unchanged and in the same location as on day 0. However, in the three poor-healing mice, the coils flanking the exposed electrodes were no longer present on the day 28 X-rays, a clear indication that the sensor moved from its original position. Yet this thin and flexible nature of the sensors also allowed them to be preserved throughout the histology process, enabling us to visualize and confirm the specific tissue surrounding the sensor (Fig. 5.2F).

5.4.3 Impedance discriminates range of fracture states

To extend the utility of our monitoring technique to a more clinically relevant fixation procedure, we designed and built sensors for integration with a bone plate model. Bone plates are commonly

used for patients with traumatic fractures that require surgical intervention with internal fixation and provide a platform from which to integrate much shorter sensors that will thus experience significantly less movement compared to the external fixator model. We designed small sensors using a flexible polyimide sensor board that could be affixed to the proximal half of commercially available murine bone plates and 25 μm-diameter platinum wires attached at the center to serve as electrodes within the fracture gap (Fig. 5.3A-B). A long, serpentine cable extended from the proximal end of the plate and was tunneled subcutaneously to the shoulder blades, leading to a set of connection pads that interfaced with our measurement instrumentation. To test our "smart" bone plate, an open surgery was performed to affix the plate to the mouse femur and the sensor wire was inserted into a reproducible (<0.25 mm) fracture gap (Fig. 5.3C-D). Surgery was also performed on control mice using the same procedure but without fracturing the bone; in this case, the sensor was placed beside the bone and muscle was sutured over it. 2-point impedance measurements were taken from 20 Hz to 1 MHz between two 700 μm^2 electrodes three times per week (Fig. S5.2), with mice euthanized at 12 (N=3 fracture) or 26 (N=5 fracture, N=2 control) days post-surgery for histology and micro-Computed Tomography (μCT) analysis.

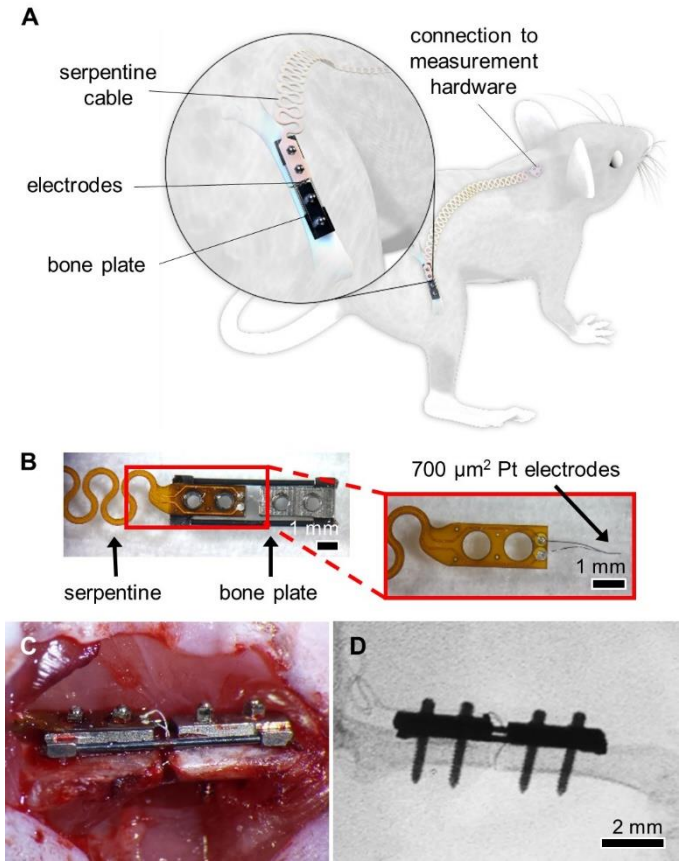

Figure 5.3 – System overview and sensor for a bone plate model
(A) System overview of sensor embedded in mouse femur fracture, where the injury is stabilized with a bone plate. **(B)** Sensors fabricated on a polyimide substrate with 700 μm^2 platinum (Pt) electrodes spaced 0.5 mm apart. Sensors were affixed to the proximal half of the bone plate, with a long flexible cable extending off the proximal end. The serpentine pattern repeated for the length of the cable, ending in two vias that served as connectors that link to the measurement hardware. **(C)** Photograph of open surgery performed to implant a bone plate and affixed sensor to stabilize a femur fracture. Surgical site was closed following sensor placement. **(D)** Fluoroscopy image of implanted Pt sensor in the fracture gap.

The mice experienced varied degrees of healing over the course of the study. Some fractures healed very well, with complete bony bridging seen by histology (Fig. 5.4A), X-ray (Fig. 5.4C), and μCT (Fig. 5.4D). While all samples showed evidence of a healing response, in some cases a bony callus did not bridge the fractured bone ends (Fig. 5.4E); this could also be seen to some extent in X-ray (Fig. 5.4G) and μCT (Fig. 5.4H). Original histology images are provided in Fig. S5.3. We were again able to define the exact tissues immediately surrounding the sensor in each sample, regardless of the global callus composition. In Fig. 5.4B, we see that the sensor is completely

embedded in new bone, while in Fig. 5.4F, the sensor is at the boundary between new bone and fibrous tissue. Representative histology images for each sample are shown in Fig. 5.5 to indicate resultant healing state (original images in Fig. S5.4), and the complete set of X-ray and μCT images are provided in Fig. S5.5. In the control mice, the sensor stayed between the unfractured bone and surrounding muscle tissue, but there was evidence of fibrous tissue surrounding it (Fig. 5.5I, Fig. S5.6).

The electrical resistance (R) at 15 kHz is plotted over time in Fig. 5.4I, and the electrical reactance (X) at 100 kHz is plotted over time in Fig. 5.4J, normalized as a ratio to day 2. These frequencies were found to reflect significant biological information, as discussed in later analysis. Data markers and lines were colored according to degree of healing – shades of red for mice sacrificed at day 12 (F1, F2, and F3), shades of blue for mice sacrificed at day 26 that healed well (F4, F5, and F6), shades of purple for mice sacrificed at day 26 that healed poorly (F7 and F8), and shades of brown for control mice sacrificed at day 26 (C1 and C2). Samples like F4 and F5 that clearly healed with their sensors well-embedded in new bone exhibited R and X values that grew steadily over time. Conversely, samples like F7 and F8 that had a mix of new bone and fibrous tissue in the fracture gap exhibited R and X values that did not rise as high, indicating stagnant healing. Measurements in the control samples remained relatively flat over time with small deviations due to the minor fibrotic response, as expected. By examining the normalized R and X values at specific frequencies over healing time, we can begin to discriminate between clearly healed samples and those with mixed healing.

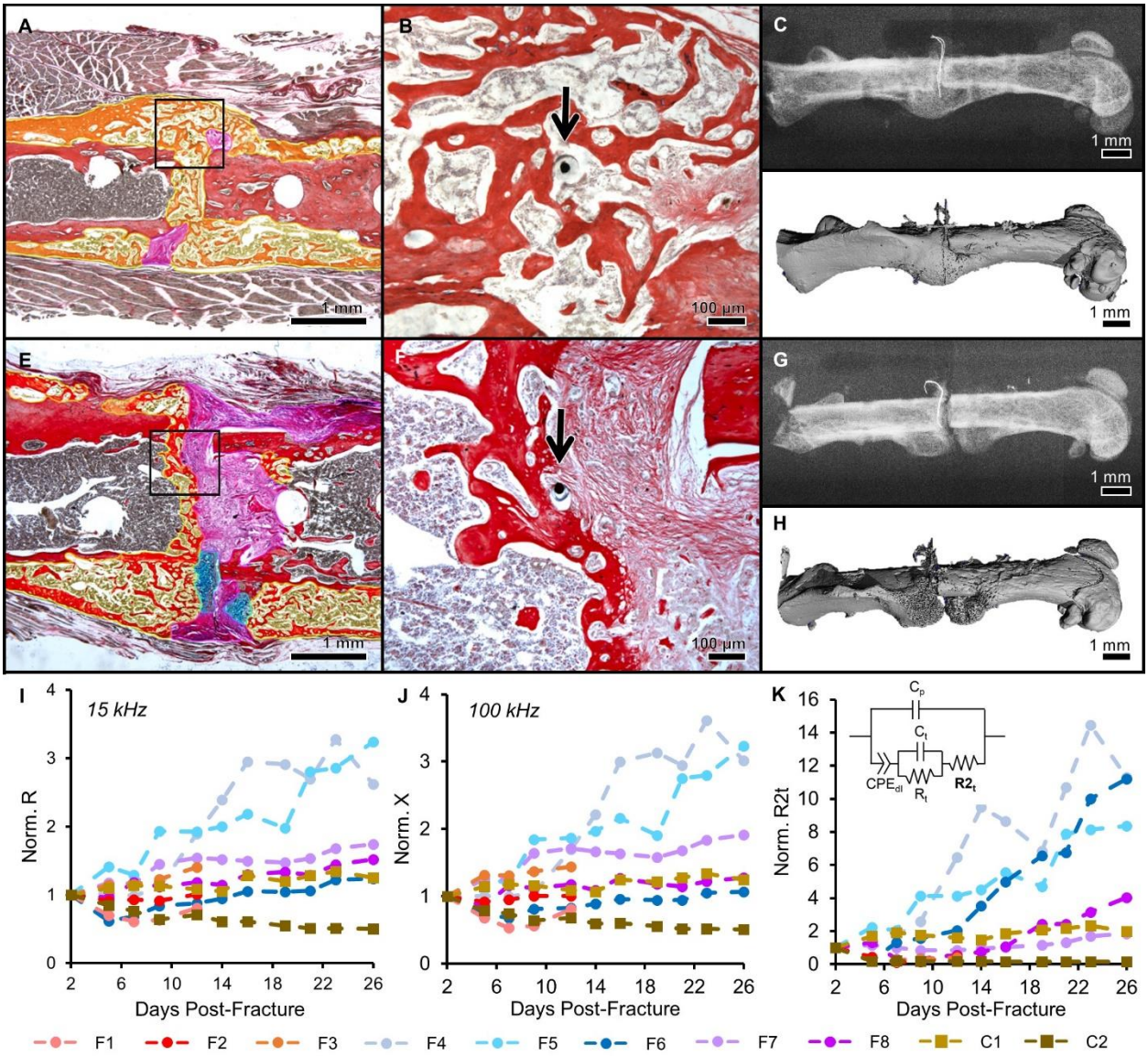

Figure 5.4 – Impedance data distinguished femur fractures completely healed from those with varied healing in a bone plate model

Histology sections are stained and false-colored like in Fig. 2. **(A)** Representative histology section of a well-healed mouse at day 26; a large bony callus has formed that completely bridges the two fracture ends. Black box outlines position of the high-magnification image in (B). **(B)** High magnification image of (A) with black arrow pointing to the electrode fully-integrated in new trabecular bone. **(C)** X-ray radiograph of well-healed fracture on day 26. **(D)** Surface rendered, three-dimensional µCT image of well-healed fracture on day 26. **(E)** Representative histology section of a mouse with mixed healing at day 26; the fracture callus includes cartilage, fibrous tissue, as well as trabecular bone. Black box outlines position of the high-magnification image in (F). **(F)** High magnification image of (E) with black arrow pointing to the electrode fully-embedded in the callus. It is surrounded by a mixture of new trabecular bone and fibrous tissue. **(G)** X-ray radiograph of fracture with mixed healing on day 26. **(H)** Surface rendered, three-dimensional µCT image of fracture with mixed healing on day 26. **(I)** R (normalized as a ratio to day 2) at 15 kHz plotted as a function of days post-fracture. Data markers and lines are colored according to degree of healing – shades of red for mice sacrificed at day 12 (F1, F2, and F3), shades of blue for mice sacrificed at day 26 that healed well (F4, F5, and F6), shades of purple for mice sacrificed at day 26 that healed poorly (F7 and F8), and shades of brown for control mice sacrificed at day 26 (C1 and C2). Normalized R clearly rises at a faster rate in the two mice

with complete bony calluses, F4 and F5. **(J)** X (normalized as a ratio to day 2) at 100 kHz plotted as a function of days post-fracture. Normalized X clearly rises at a faster rate in the two mice with complete bony calluses, F4 and F5. **(K)** Impedance data at all measured frequencies is fit to an equivalent circuit model (inset), and the $R2_t$ parameter is extracted, normalized as a ratio to day 2, and plotted as a function of days post-fracture. This analysis is able to clearly distinguish the samples that are classified as union by orthopedic surgeons (F4, F5, and F6 in Table 5.1).

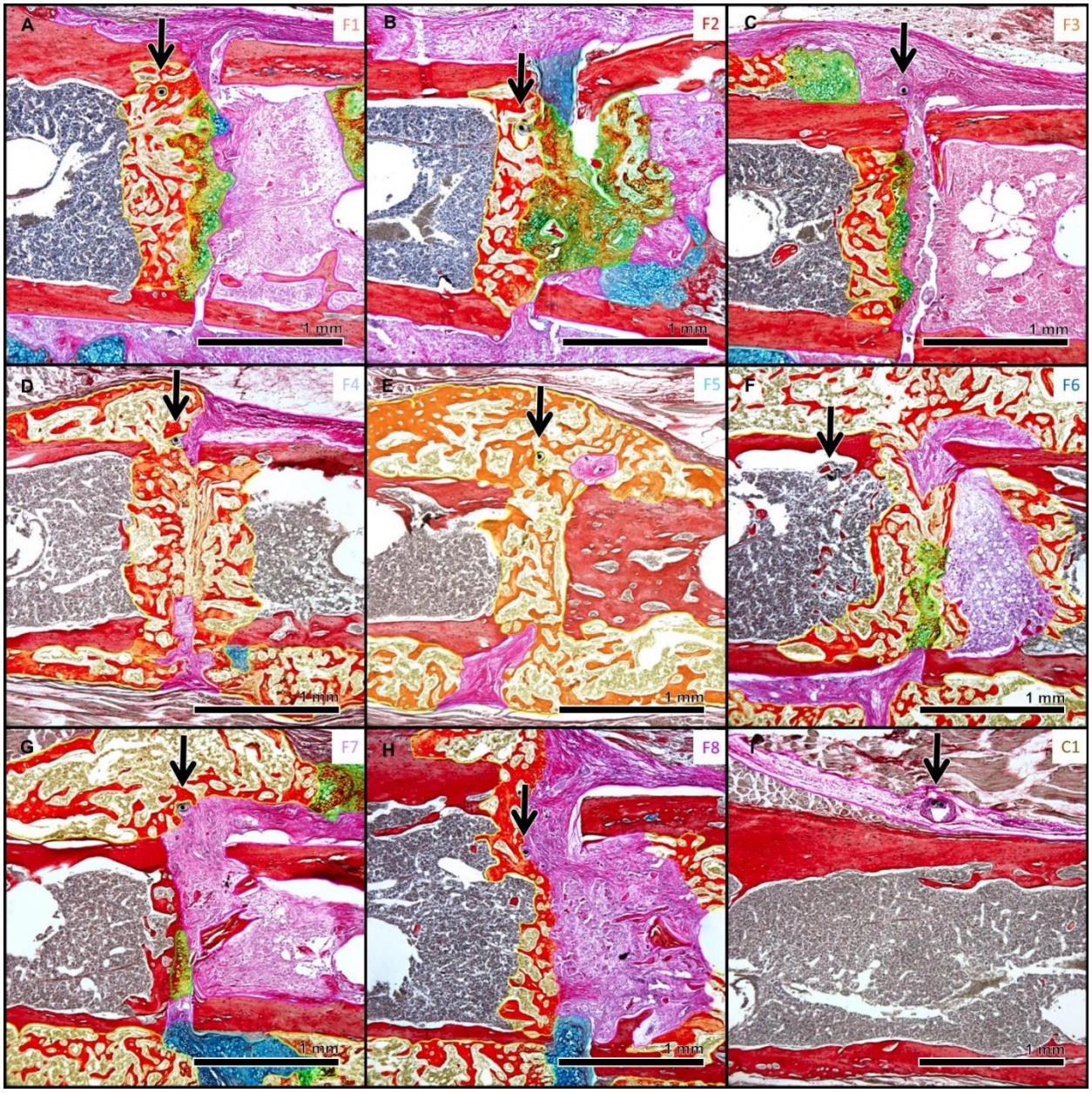

Figure 5.5 – Histology sections for all bone plate model mice

Histology sections are stained and false-colored like in Fig. 2. Green = cartilage converting to bone. Black arrows point to sensors embedded in the fracture callus. Sample labels (upper right corner) are colored to match the graphs in Fig. 4I-K. **(A-C)** Histology sections for mice sacrificed at day 12. **(D-F)** Histology sections for mice sacrificed at day 26 with fracture calluses composed almost entirely of new trabecular bone. **(G-H)** Histology sections of mice sacrificed at day 26 that experienced mixed healing. **(I)** Representative histology section of a control mouse, where the sensors are embedded in a small amount of fibrous tissue.

5.4.4 Model-driven fit of data robustly classifies healing trends

In order to determine how the data best tracked healing, we fit the resistance and reactance data at all measured frequencies to an equivalent circuit model of biological tissue. This enabled us to extract the dominant electrical properties that explain the differences in healing that we observe. The equivalent circuit models the double-layer impedance at the electrode-electrolyte surface as a constant phase element (CPE_{dl}) in series with the tissue component, and places a capacitor (C_p) in parallel to reflect the parasitic capacitance due to coupling along the two long wire traces leading from the electrodes to the connector. The tissue component is comprised of a resistor (R_t) and capacitor (C_t) in parallel, in series with another resistor ($R2_t$) (Fig. 5.4K). R_t represents the ionic intracellular environment, $R2_t$ represents the ionic extracellular environment, and C_t represents the double-layer cell membranes. In our model, we held C_p constant at 25 μF, extracted from high-frequency measurements taken with our sensors immersed in Phosphate Buffered Saline (PBS) prior to implantation. The impedance CPE_{dl} is calculated as

$$Z_{CPE} = 1/Q(j\omega)^{\alpha} \qquad (5.1)$$

where Q is the numerical value of admittance ($1/|Z|$) at $\omega = 1$ rad/s, ω is the angular frequency, and α is a constant from 0 to 1 (1 representing a perfect capacitor). We held α constant at 0.5, based on low-frequency measurements of our sensors in PBS. From a study characterizing an osseous implant using EIS[51], we hypothesized that the changing impedance in our study would be most reflected in $R2_t$. We thus fit R_t and C_t at an initial time point (day 2) and constrained it at that value over time. We used a custom MATLAB script to fit our data at each time point to this equivalent circuit model, interpolating 10 steps in between each time point to guide the mathematical solution and avoid jumping to non-physical values. Goodness of fits graphs are provided in Fig. S5.7. By normalizing $R2_t$, shown in Fig. 5.4K, we find that this parameter accurately recapitulates healing

state. The best healed samples (F4, F5, and F6) rise clearly above the samples that experienced more varied healing.

5.4.5 Impedance correlates with μCT measures of healing

To understand how clinicians would characterize healing using standard classification techniques, we had five orthopaedic surgeons score the final X-rays for each sample using the modified Radiographic Union Scale for Tibial (RUST) fractures[50]. Each cortex is assigned a value from 1 to 4: 1 if there is no callus present, 2 if there is callus present, 3 for bridging callus, and 4 for remodeled bone where the fracture line is no longer visible. Our data excludes the anterior cortex as the sensor typically occludes the full view on an X-ray, so the total possible score ranges from 3 to 12. Each X-ray was also categorized as a union (U), nonunion (NU), or suspected nonunion (SNU); the summarized data is presented in Table 5.1 (raw data available in Table S5.1). In clearly healed cases like F4, F5, and F6, there is strong agreement between surgeons in total RUST score as evidenced by low standard deviations, and all surgeons categorized these three fractures as fully united. This corroborates our impedance data, as the $R2_t$ parameter extracted from the model-driven fit also classified these three samples as well-healed. However, surgeon evaluation varied for ambiguous cases, with a wider spread in total RUST score as well as disagreement in how to categorize a fracture, substantiating the lack of a standard for assessing fracture healing by X-ray.

Table 5.1 – Clinician-rated RUST scores for fracture X-rays

Total RUST scores for each sample were averaged amongst five orthopaedic surgeons and presented as mean ± standard deviation. The maximum score subtracted by the minimum score for each sample was calculated to show the largest difference between surgeon evaluations. The number of surgeons who categorized each sample as union (U), nonunion (NU), or suspected nonunion (SNU) are also provided. In clearly healed cases (F4,F5,F6) there is strong agreement between clinicians, but results vary for ambiguous cases.

	Total RUST Score	Max -	Categorization (# of Surgeons)		
Sample	(Mean ± Std. Dev.)	Min	U	NU	SNU
F1	4.8 ± 1.10	3	1	1	3
F2	4.8 ± 1.10	3		2	3
F3	6 ± 1	2		1	4
F4	8.4 ± 0.55	1	5		
F5	8.8 ± 0.84	2	5		
F6	9 ± 0	0	5		
F7	9 ± 0	0	2		3
F8	7 ± 1	2	1	3	1

In the clinic, computed tomography (CT) scans can be requested to confirm or reject suspected delayed or nonunion cases. While CT sees limited use in the clinic due to its high costs, it does enable quantitative measures that reflect biological and structural measures of healing. We quantified a number of microstructural indices from micro-computed tomography (μCT) scans of our samples to determine their degree of correlation with EIS. Preexisting bone was excluded in our analysis to only examine mineralized tissue within the fracture callus, and bone volume (BV), total volume (TV), bone mineral density (BMD), trabecular number, trabecular thickness, and trabecular separation were quantified (Table S5.2). Following linear regression analyses, we find that normalized resistance (R) significantly correlates with the ratio of bone volume to total volume (BV/TV), BMD, trabecular number, and trabecular thickness (Fig. 5.6A-D). These correlations peak at 15 kHz, with normalized R rising with increasing BV/TV ($R^2 = 0.7555$, $p < 0.01$) and BMD ($R^2 = 0.7925$, $p < 0.01$). In addition, normalized R at 15 kHz also has a positive relationship with trabecular number ($R^2 = 0.5641$, $p = 0.03$) and trabecular thickness ($R^2 = 0.6417$, $p = 0.02$), but has no correlation with trabecular separation ($R^2 = 0.3599$, $p = 0.12$). Similar relationships are found by comparing normalized reactance (X) to these μCT indices.

Importantly, by plotting the associated R^2 and p values at every measured frequency for each pair of variables, we can pinpoint the specific frequency ranges in which impedance provides valuable information about healing. As seen in Fig. 5.6E, normalized R is significantly correlated to BV/TV from 10 kHz to 250 kHz ($R^2 > 0.5$, $p \leq 0.04$), with a peak at 15 kHz. In Fig. 5.6F, we see that normalized X is significantly correlated to BV/TV at a higher set of frequencies – 50 kHz to 1 MHz ($R^2 > 0.55$, $p < 0.03$), with a peak at 100 kHz. Analogous graphs for the other μCT indices are shown in Fig. S5.8. Normalized R is significantly correlated with BMD from 10 kHz to 250 kHz ($R^2 > 0.55$, $p < 0.03$), with trabecular number from 15 kHz to 100 kHz ($R^2 \geq 0.5$, $p < 0.05$), and with trabecular thickness from 5 kHz to 100 kHz ($R^2 > 0.45$, $p < 0.05$). Normalized X is significantly correlated with BMD from 50 kHz to 100 kHz ($R^2 \geq 0.6$, $p \leq 0.02$), and with trabecular thickness at from 25 kHz to 100 kHz ($R^2 > 0.55$, $p \leq 0.03$). These results are also summarized in Table S5.3. This regression analyses not only determines that EIS correlates to clinically-relevant measures of bone healing that would otherwise require expensive μCT evaluation, but also pinpoints the specific frequency ranges at which this is most significant.

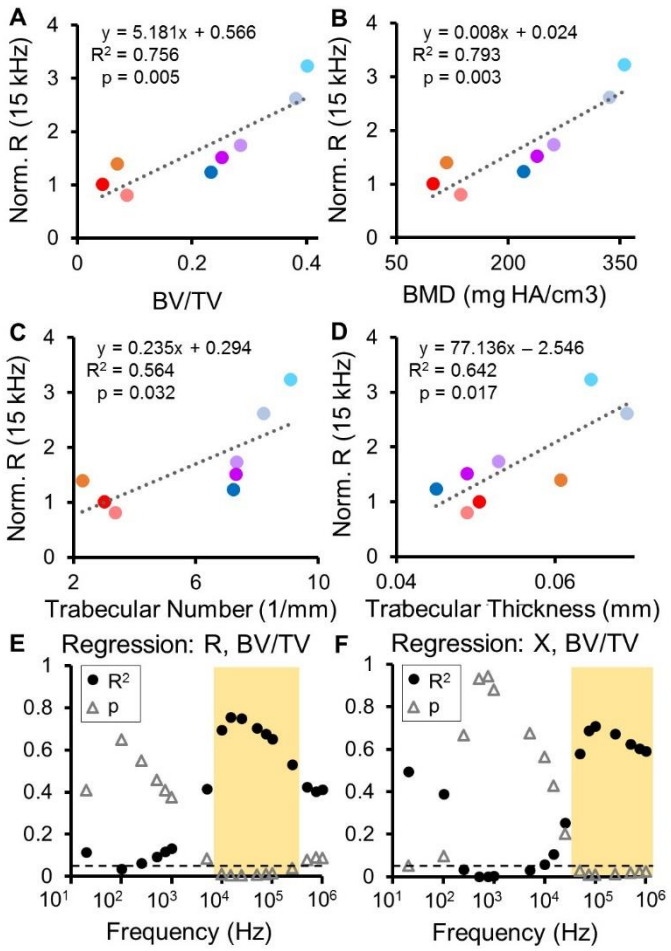

Figure 5.6 – Regression analyses comparing normalized impedance data to µCT indices
(A-D) Normalized R at 15 kHz is significantly correlated to the ratio of bone volume to total volume (BV/TV), bone mineral density (BMD), trabecular number, and trabecular thickness. Individual markers are colored to match the corresponding samples in Fig. 4I-K. **(E-F)** Resultant R^2 and p-values from regression analyses between normalized R and BV/TV as well as normalized X and BV/TV plotted as a function of frequency. Significance is set at $p < 0.05$ (below dashed line). Significant relationships between R and BV/TV occur from 10 kHz to 250 kHz, and significant relationships between X and BV/TV occur from 50 kHz to 1 MHz.

5.5 Discussion

Our study aimed to validate the use of EIS to develop smart fracture fixation instrumentation, with the goal of arming physicians with quantitative information about the state of fracture repair in patients. While previous research has been done utilizing impedance to evaluate bone fractures, other groups have used surface electrodes on the outside of the leg or pins drilled in the proximal and distal ends of the bone. As a result, EIS measurements in these studies reflect a global

assessment with low specificity to the changing fracture callus, as signal must also travel through the muscle and skin surrounding the injured bone. To our knowledge, our study is the first to design and fabricate microscale sensors that can be implanted directly in the fracture gap intra-operatively. This enabled longitudinal EIS measurements to be taken specifically in the calli of individual mice with fractures stabilized using either external fixators or bone plates *in vivo*.

In this paper, we demonstrate the utility of EIS to track differences between fractures healing well and those healing poorly in two clinically-relevant models, laying the foundation for use of this technique to detect fracture nonunion or other complications. Beginning with an external fixator model that utilized two defect sizes, we studied the ability of EIS to distinguish between two substantially different healing pathways. The 2 mm osteotomy resulted in a critical-sized defect with no substantial indications of healing, as the fracture gap was dominated by amorphous granulation and fibrous tissue. Electrical resistance (R) did not change over time in these mice because the electrodes were consistently exposed to this amorphous mixture of fibrous tissue. In contrast, the 0.5 mm distraction resulted in an increase in R as the fracture gap included cartilage and new bone over the course of 28 days. While these results show a clear difference between impedance measurements in fractures with varied healing responses due to different defect sizes, this study was limited in that the sensor itself appeared to generate a fibrotic response.

By using a smaller, flexible sensor assembled using thin platinum wire, we were able to track EIS throughout the time course of fracture healing with decreased disruption to the healing process in both an external fixator model and bone plate model. From these two surgical models, a range of healing responses was produced from atrophic nonunion to full bridging. To understand the correlation of EIS measurements with healing, we also assessed these fractures with the full range of standard clinical and laboratory techniques, including histology, X-ray with assigned RUST

scores, and μCT. Due to the small size of our sensors, histology could confirm not only the tissue composition across the entire fracture gap, but also identify the exact tissue the sensor was embedded in. While motion of the sensor in some samples likely contributed to atrophic nonunion, histological evidence showed that our microscale sensors were well integrated within the fracture tissue and when appropriately immobilized, did not prevent complete bony bridging between fractured bone ends. Full integration of our sensors within fracture calli was critical for taking local measurements of healing tissue over time in individual mice without disturbing the repair process.

We found that impedance between mice that healed well and those that healed poorly deviated quickly, with electrical resistance (R) and reactance (X) rising at a faster rate in well-healed fractures. This indicates that impedance may be able to rapidly identify stalled healing as compared to a traditional technique such as X-ray, which is only able to detect mineralized tissue at late healing stages. Resistance reflects the ability of a material to conduct charge – a highly conductive material will exhibit a small resistance, while a less conductive material will have a larger resistance. As the dominant tissue in a fracture callus transitions from highly conductive blood and cartilage to less conductive trabecular and cortical bone, our sensors confirm that R rises rapidly over time in mice that exhibited a clear healing response. Reactance describes effects that store energy such as charge separation across cell membranes (which act as barriers to charge flow and look capacitive). Highly cellular tissues have a higher capacity for energy storage and thus a larger X, particularly at higher frequencies. Because bone is comprised of multiple matrix layers that can be modeled as capacitors and marrow is highly cellular, we see a sharp rise in X in the mice with bridging calli, in contrast to more moderate changes in mice with poor healing. Both R and X stayed roughly flat in the control samples, in which no fracture was made, with minor deviations over time due to a small fibrous tissue response encapsulating the sensor. We also see that the

greatest spread in R and X across days occurs in the 1 kHz to 100 kHz frequency range, and formation of a robust callus influences the frequency response of the measurement. This reveals the importance of spectroscopic measurements, which enable us to precisely track where changes arise in the frequency range over healing time. These results align with previous work in cadaveric and *ex vivo* mouse models[35,36] that describe resistive components increasing over fracture healing time (blood to cartilage to bone), and reactive components rising as cartilage converts to bone. This assessment is corroborated by EIS data collected in both the external fixator and bone plate models, signifying the consistency of this technique in two different fracture fixation schemes.

By fitting our data to an equivalent circuit model, we were able to combine the effects of resistance and reactance changes at all measured frequencies and determine robust measures of trends over time. By simplifying the complex physical components and processes present in healing fractures to electrical components that suitably approximate tissue[26,51], our analysis found that the $R2_t$ term describing the extracellular environment was able to clearly separate the mice with bony bridging from those without. One of the mice, F6, developed an extremely large callus with a lot of new trabecular bone as well as a pocket of amorphous tissue. This is a unique case in which the fracture was clinically considered healed (Table 5.1), but still had unexpected fibrous tissue within the gap. While the R and X values for this sample were grouped with mice that had varied healing, fitting to our equivalent circuit model was able to pull out all the fractures that would be clinically categorized as unions. Although the model is an approximation of the biology occurring between the two electrodes in the fracture gap, it allowed us to obtain robust measures of change which employed all of the impedance data in a combined fashion to help explain the differences in healing that we observed. With validation from a larger clinical trial, this work could be used as a platform

to create prognostic tools in the clinic to predict and differentiate proper healing and delayed or nonunion.

In mice with clearly healed fractures, all techniques showed strong agreement in classifying the fractures as united. However, in cases with a more heterogeneous healing response, there was no consensus among the five surgeons, with up to 3 points difference in the total RUST score. Notably, there were two cases that were categorized as “union”, “nonunion”, and “suspected nonunion” depending on the surgeon being asked. This further emphasizes the need for an objective method to quantify the degree of repair in a healing fracture, as interpretation of X-ray can vary amongst surgeons, potentially due to factors like medical training, experience, etc. In order to correlate EIS data to more accurate measures of healing, we performed μCT. Additional quantitative data derived from analyzing μCT revealed the sensitivity of EIS measurements to relevant parameters of healing, including BV/TV, BMD, trabecular number, and trabecular thickness. Our regression analyses show that both normalized R and X have strong positive relationships with these four μCT indices within specific frequency ranges. These correlations peak in significance at 15 kHz for R and at 100 kHz for X, reflecting the primary frequency of interest to understand mineralization of the fracture callus. As we’ve described, R and X rise as cartilage is converted to bone within a fracture callus. As this healing progresses, the total amount of mineralized bone as a ratio of the total callus volume will also rise. Furthermore, bone mineral density rises correspondingly as chondrocytes become mineralized and then convert to bone. Likewise, as fractures transition from a solid cartilage callus to trabecular bone, we expect trabecular number and thickness to increase. Our impedance measurements are able to track these changes with a high degree of sensitivity, providing valuable information that would otherwise require the extra expense and radiation exposure associated with a CT scan.

5.6 Clinical application and conclusion

While mice provided a well-established model of fracture healing that closely mimics the same process in humans, one of the biggest challenges was designing small, wired implants within tight size constraints. Since the tibia and femur bones in a mouse measure approximately 1-1.5 mm in diameter, this study implanted only the electrodes at the fracture site, with additional instrumentation to take impedance measurements located outside the animal. The flexibility of metal wires at this small size (25 to 60 μm diameter) permitted movement of some sensors, which we hypothesize occurred due to soft tissue movement near the fracture or callus formation effectively pushing the sensor. While we observed negligible changes in inter-electrode distance, future designs in a larger model should aim to eliminate potential fluctuations, possibly by using stiffer electrodes. In addition, while smaller sensors improved integration in the fracture tissue, they had higher impedance and thus possibly reduced the signal-to-noise ratio (SNR) of our measurements. Future designs could increase electrode surface area while restricting overall size to limit this effect. Translating this technology to patients will involve development of electronics to integrate wireless data transfer, which would also enable more frequent measurements. For patients already undergoing surgery to stabilize a fracture with instrumentation, a sensor could be added intra-operatively as a simple addition to standard surgical hardware to provide the patient and physician with quantitative information on the state of fracture healing. This would provide detailed information to physicians and patients about the healing trends over time at much higher temporal resolution than currently available via conventional follow-up appointments spaced weeks apart. Furthermore, EIS holds promise for early detection of fracture nonunion, which currently can take over 6 months to diagnose, as it is more sensitive to the early stages of hematoma and cartilage than traditional techniques and can thus more quickly identify stalled healing.

In this paper, we have presented complete histologic, radiographic, and μCT analyses with our data to show that our local EIS measurements can evaluate the fracture callus with high sensitivity. Use of both external fixators and bone plates demonstrates the value of EIS in different models with different rates and progression of healing, with even the smallest of fixation implants providing a convenient platform for adding sensors and instrumentation. This establishes EIS as a technology that is amenable to miniaturization and can thus be translated and easily integrated into current fracture management strategies in the clinic. Our study lays the groundwork for instrumented implants, which could be used during surgical intervention to provide physicians with additional quantitative information during post-operative monitoring and help guide clinical care decisions.

5.7 Supplemental figures

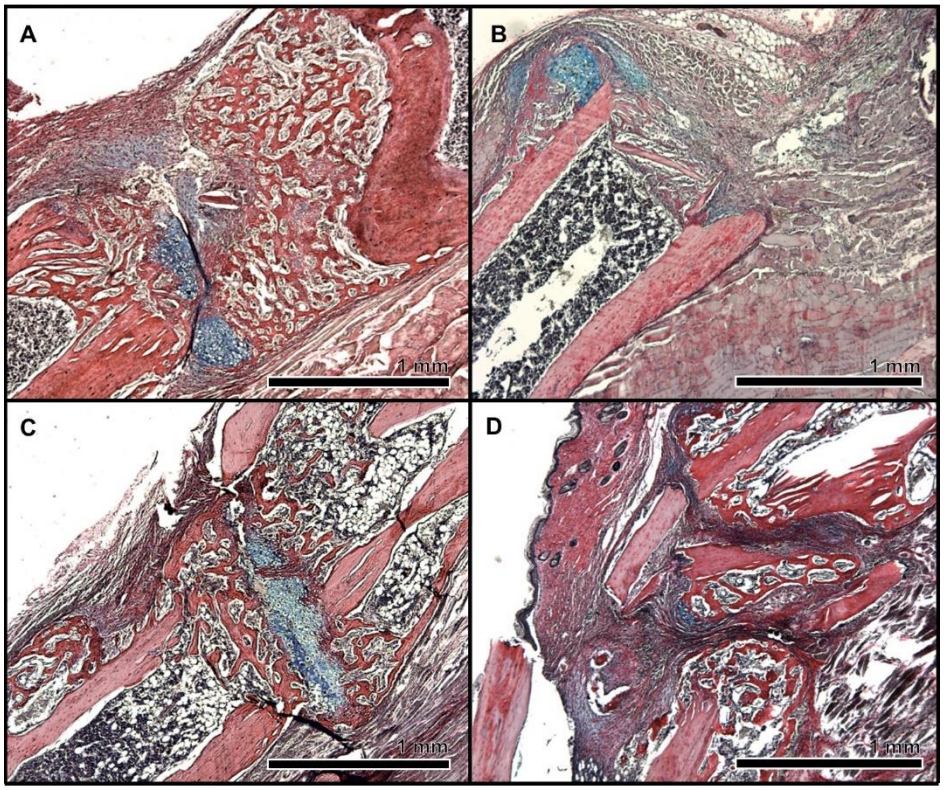

Figure S5.1 – Original histology images of external fixator model samples (Fig. 5.2A-B,D-E)
Histology sections are stained with HBQ (blue = cartilage, red = bone). **(A)** Original image of the histology section in Fig. 5.2A of an externally-fixed 0.5 mm defect at 14 days post-fracture. **(B)** Original image of the histology section in Fig. 5.2B of an externally-fixed 2 mm defect at 14 days post-fracture. **(C)** Original image of the histology section in Fig. 5.2D of an externally-fixed well-healed mouse at day 28. **(D)** Original image of the histology section in Fig. 5.2E of an externally-fixed poor-healed mouse at day 28.

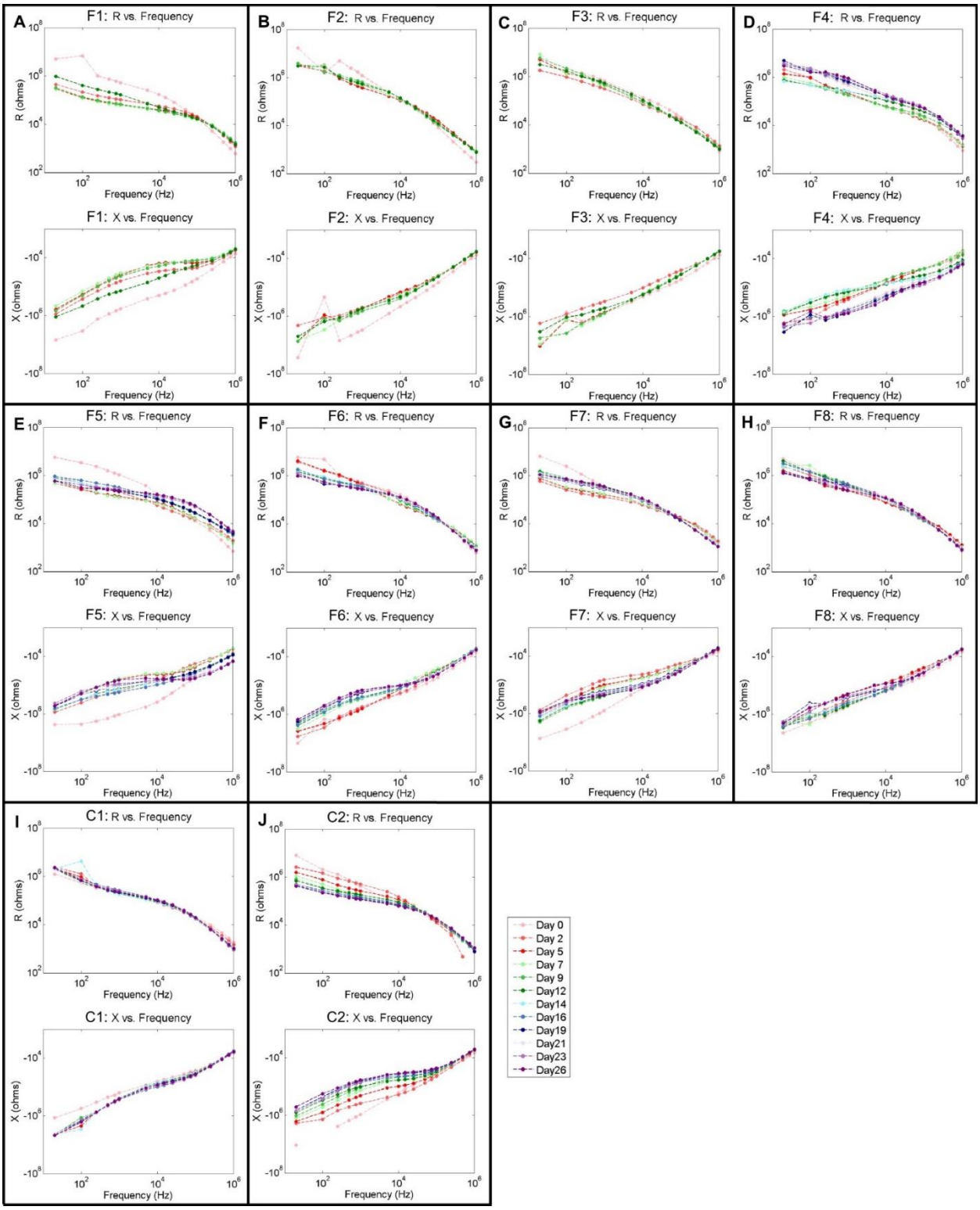

Figure S5.2 – Frequency response over time in all bone plate model mice

(A-C) Electrical resistance (R) and reactance (X) plotted as a function of frequency for each measurement day in mice sacrificed on day 12. **(D-F)** R and X plotted as a function of frequency for each measurement day in mice sacrificed on day 26 with calluses composed nearly completely of new trabecular bone. **(G-H)** R and X plotted as a function of

frequency for each measurement day in mice sacrificed on day 26 that experienced mixed healing. **(I-J)** R and X plotted as a function of frequency for each measurement day for control mice.

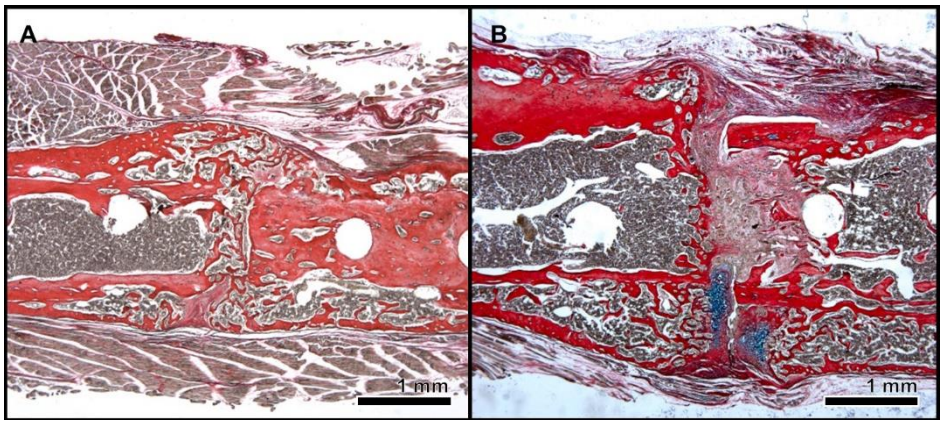

Figure S5.3 – Original histology images of well-healed and mixed-healed bone plate model samples (Fig. 5.4A,E)

Histology sections are stained with HBQ (blue = cartilage, red = bone). **(A)** Original image of the histology section in Fig. 5.4A of a fracture fixed with a bone plate at 26 days post-fracture that was well-healed. **(B)** Original image of the histology section in Fig. 5.4E of a fracture fixed with a bone plate at 26 days post-fracture that had a mixed healing response.

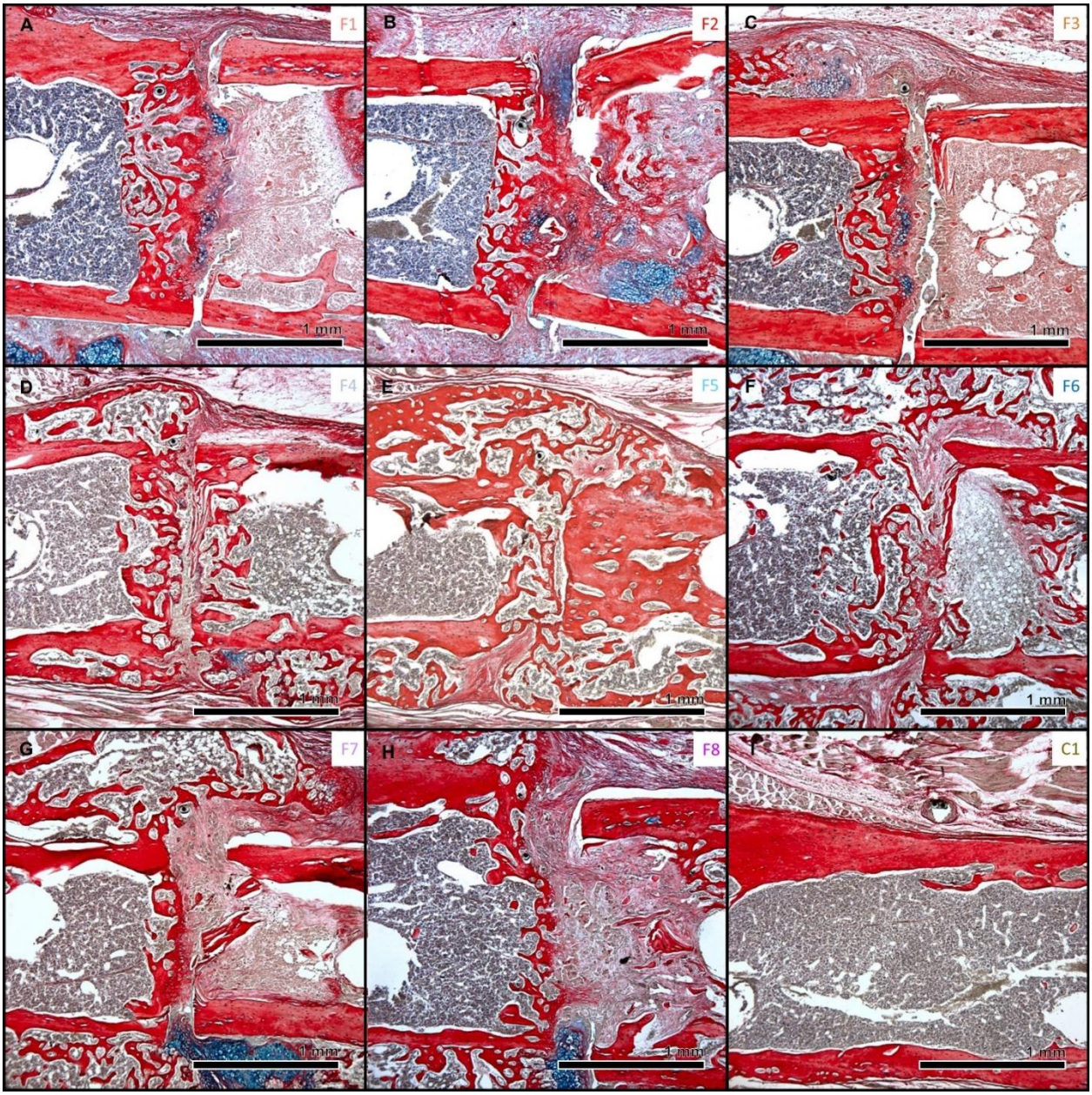

Figure S5.4 – Original histology images of all bone plate model samples (Fig. 5.5)
Histology sections in this figure are stained with HBQ (blue = cartilage, red = bone). **(A-C)** Original images of the histology sections in Fig. 5.5A-C of mice sacrificed on day 12. **(D-F)** Original images of the histology sections in Fig. 5.5D-F of mice sacrificed on day 26 with calluses composed nearly completely of new trabecular bone. **(G-H)** Original images of the histology sections in Fig. 5.5G-H of mice sacrificed on day 26 that experienced mixed healing. **(I)** Original image of the histology section in Fig. 5.5I of a control mouse on day 26.

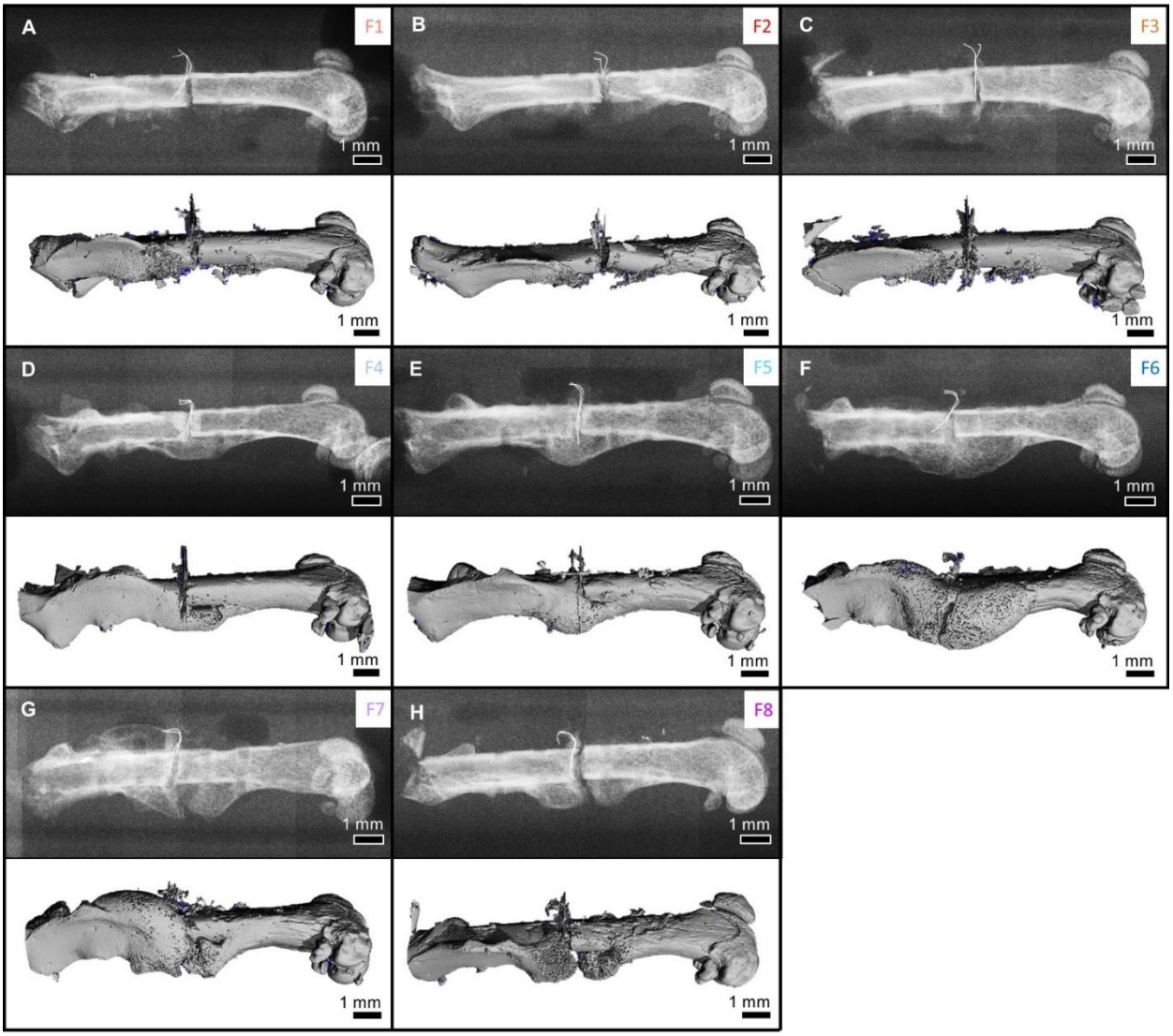

Figure S5.5 – X-ray and µCT images of all bone plate model fracture samples
(A-C) X-ray and µCT images of femurs from mice sacrificed on day 12. **(D-F)** X-ray and µCT images of femurs from mice sacrificed on day 26 with calluses composed nearly completely of new trabecular bone. **(G-H)** X-ray and µCT images of femurs from mice sacrificed on day 26 that experienced mixed healing.

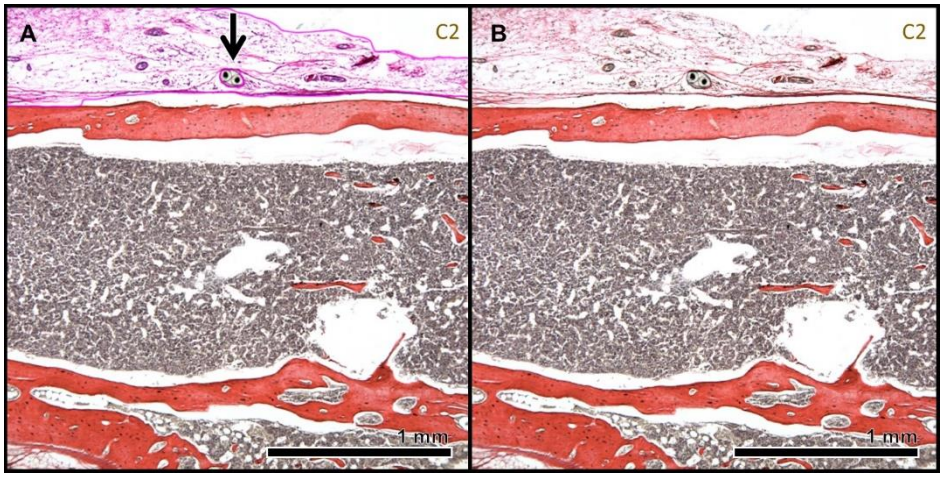

Figure S5.6 – Histology image for control mouse

Histology sections in this figure are stained with HBQ (blue = cartilage, red = bone). **(A)** Histology section is false-colored to aid interpretation of tissue composition. Purple = fibrous/amorphous tissue. Original red color = cortical bone, black/white area = bone marrow. Black arrow points to sensors embedded in fibrous tissue next to the unfractured bone. **(B)** Original histology section from (A).

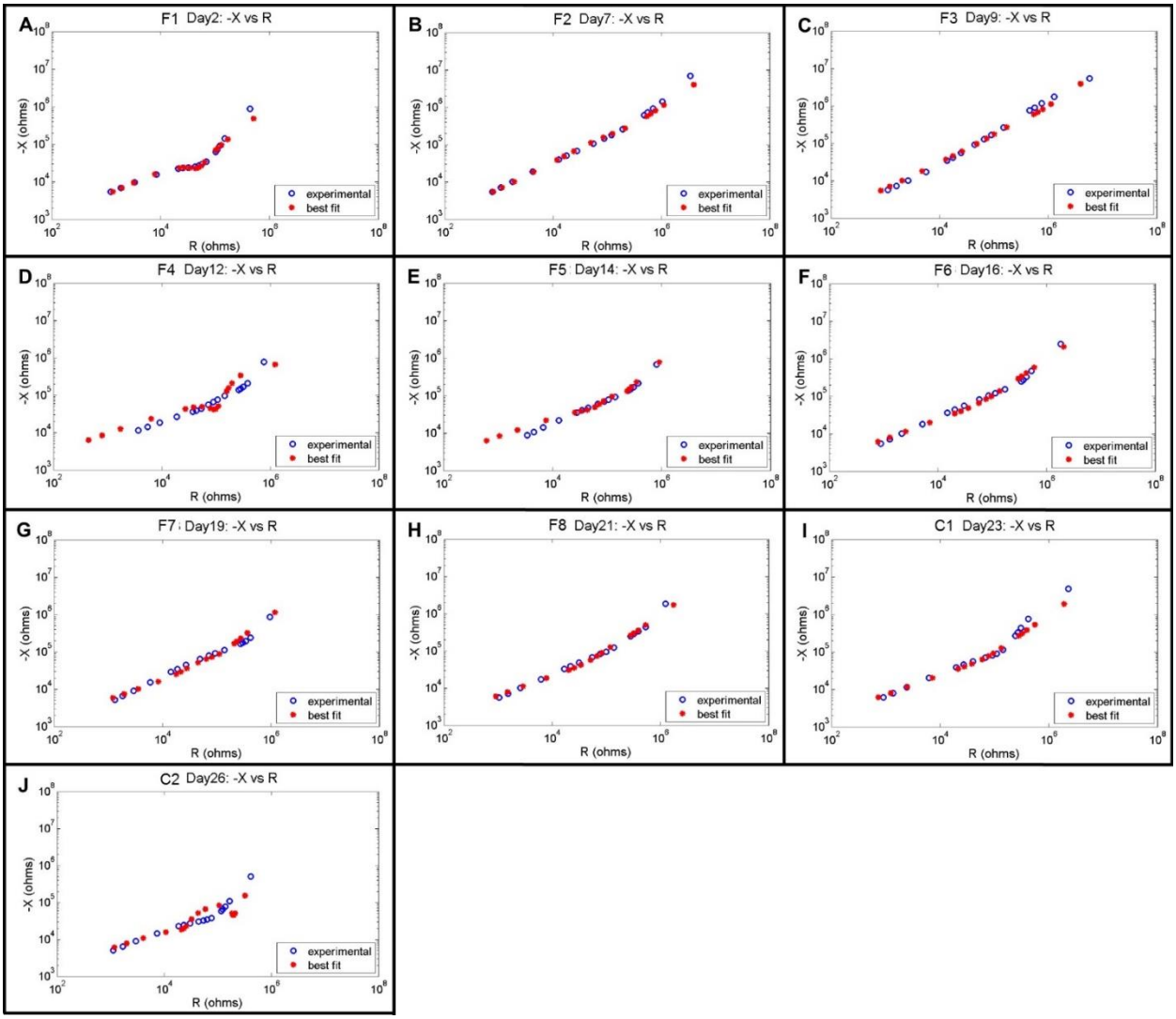

Figure S5.7 – Goodness of fits for data fit to equivalent circuit model

Representative set of graphs depicting the experimental values and best fit values derived from the equivalent circuit model of electrical reactance plotted over electrical resistance.

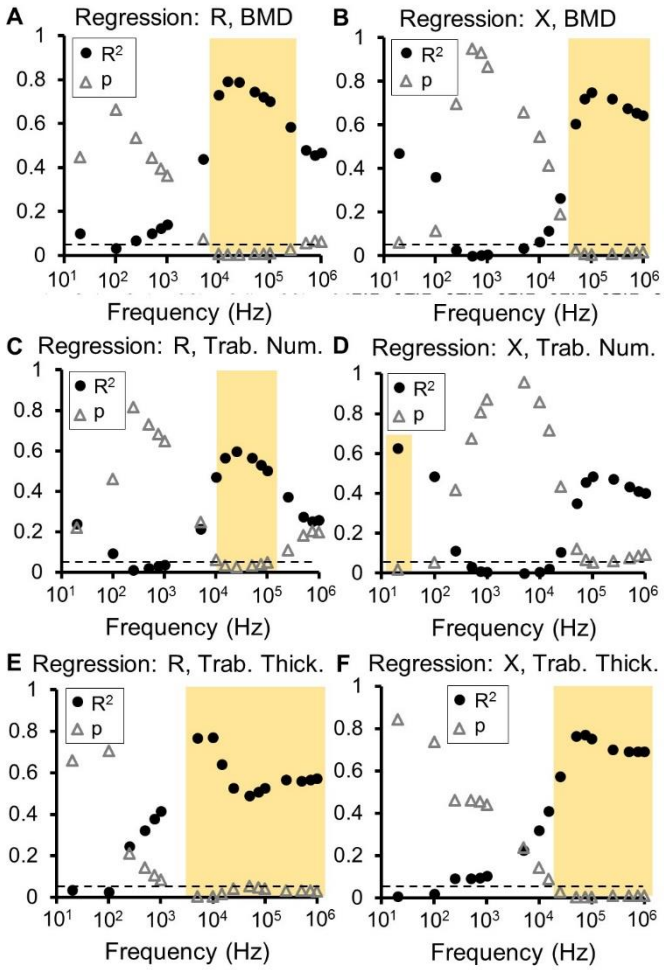

Figure S5.8 – Clinically-relevant frequencies of operation with significant correlation between impedance data and μCT

Resultant R^2 and p values from regression analyses comparing normalized R and X with bone mineral density (BMD), trabecular number, and trabecular thickness. Significance is set at $p < 0.05$ (below dashed line).

Table S5.1 – Modified RUST scores of bone plate model samples

Five surgeons scored each cortex (excluding the anterior cortex) from 1 to 4: 1 = no callus, 2 = callus present, 3 = bridging callus, 4 = remodeled with no visible fracture line. Scores from the three cortices for each sample were added to generate a total score between 3 and 12. Each surgeon also clinically categorized each sample as union (U), nonunion (NU), or suspected nonunion (SNU).

	Surgeon 1					Surgeon 2				
Sample	**Cortex 1**	**Cortex 2**	**Cortex 3**	**Total**	**Category**	**Cortex 1**	**Cortex 2**	**Cortex 3**	**Total**	**Category**
F1	1	2	2	5	NU	2	1	2	5	SNU
F2	2	2	2	6	NU	2	1	2	5	SNU
F3	3	2	2	7	SNU	2	1	2	5	SNU
F4	3	2	3	8	U	3	3	3	9	U
F5	3	2	3	8	U	3	3	3	9	U
F6	3	3	3	9	SNU	3	3	3	9	SNU
F7	2	2	2	6	NU	2	2	2	6	NU
F8	3	3	3	9	U	3	3	3	9	U

	Surgeon 3					Surgeon 4				
Sample	**Cortex 1**	**Cortex 2**	**Cortex 3**	**Total**	**Category**	**Cortex 1**	**Cortex 2**	**Cortex 3**	**Total**	**Category**
F1	1	1	1	3	NU	1	2	2	5	SNU
F2	1	1	1	3	NU	2	1	2	5	SNU
F3	2	1	2	5	NU	2	2	2	6	SNU
F4	3	2	3	8	U	3	3	3	9	U
F5	3	2	3	8	U	3	3	3	9	U
F6	3	3	3	9	U	3	3	3	9	SNU
F7	3	3	2	8	NU	2	3	2	7	SNU
F8	3	3	3	9	U	3	3	3	9	U

	Surgeon 5				
Sample	**Cortex 1**	**Cortex 2**	**Cortex 3**	**Total**	**Category**
F1	2	2	2	6	SNU
F2	2	1	2	5	SNU
F3	2	3	2	7	SNU
F4	3	2	3	8	U
F5	3	4	3	10	U
F6	3	3	3	9	U
F7	3	2	3	8	U
F8	3	3	3	9	U

Table S5.2 – Quantified µCT indices for bone plate model samples

The cortical surface and bone morphology for each sample was assessed from µCT scans in the region between the central surgical screws, and a number of three-dimensional microstructural indices are reported here.

Mouse	Day	Bone Volume (BV)	Total Volume (TV)	BV/TV	Bone Mineral Density (BMD)	Trabecular Number	Trabecular Thickness	Trabecular Separation
F1	12	0.2129	2.4666	0.0863	135.8959	3.3514	0.0489	0.3197
F2	12	0.1029	2.3747	0.0433	99.1292	2.9957	0.0504	0.3456
F3	12	0.1831	2.6416	0.0693	116.7744	2.2935	0.0607	0.4634
F4	26	1.7574	4.6154	0.3808	335.406	8.2039	0.069	0.1146
F5	26	2.38	5.9458	0.4003	355.0899	9.0805	0.0645	0.1023
F6	26	3.8163	16.4001	0.2327	219.9742	7.226	0.045	0.134
F7	26	2.6295	9.2405	0.2846	260.3964	7.3311	0.0528	0.1405
F8	26	1.8757	7.4606	0.2514	237.9708	7.302	0.0489	0.1401

Table S5.3 – Resulting R^2 and p values from regression analyses comparing impedance to quantified µCT indices

Regression analyses was performed to compare normalized electrical resistance (R) and reactance (X) to each of the reported µCT indices. The resultant R^2 and p values associated with each relationship are provided with 2 significant digits. If the p-value is listed as 0.00, this indicates a value less than 0.01. Significance is set as $p < 0.05$, with significant p-values underlined.

Normalized Resistance (R)																		
	Freq (Hz)	**20**	**100**	**250**	**500**	**750**	**1k**	**5k**	**10k**	**15k**	**25k**	**50k**	**75k**	**100k**	**250k**	**500k**	**750k**	**1M**
BV/TV	R^2	0.12	0.04	0.06	0.09	0.12	0.13	0.41	0.69	0.76	0.75	0.70	0.68	0.65	0.53	0.43	0.40	0.41
	p	0.41	0.65	0.55	0.46	0.41	0.38	0.09	0.01	0.01	0.01	0.01	0.01	0.02	0.04	0.08	0.09	0.09
BMD	R^2	0.10	0.03	0.07	0.10	0.12	0.14	0.44	0.73	0.79	0.79	0.75	0.72	0.70	0.58	0.48	0.46	0.47
	p	0.45	0.66	0.53	0.45	0.39	0.36	0.07	0.01	0.00	0.00	0.01	0.01	0.01	0.03	0.06	0.07	0.06
Trab. Num.	R^2	0.24	0.09	0.01	0.02	0.03	0.04	0.21	0.47	0.56	0.60	0.56	0.53	0.50	0.37	0.27	0.25	0.26
	p	0.22	0.46	0.82	0.73	0.68	0.65	0.25	0.06	0.03	0.02	0.03	0.04	0.05	0.11	0.18	0.21	0.20
Trab. Thick.	R^2	0.03	0.03	0.25	0.32	0.38	0.41	0.77	0.77	0.64	0.53	0.49	0.51	0.53	0.57	0.56	0.57	0.57
	p	0.66	0.71	0.21	0.14	0.10	0.09	0.00	0.00	0.02	0.04	0.05	0.05	0.04	0.03	0.03	0.03	0.03
Trab. Sep.	R^2	0.24	0.09	0.01	0.01	0.02	0.02	0.13	0.29	0.36	0.40	0.39	0.37	0.35	0.27	0.20	0.18	0.18
	p	0.22	0.48	0.84	0.78	0.74	0.71	0.39	0.17	0.12	0.09	0.10	0.11	0.12	0.19	0.27	0.30	0.29
Normalized Reactance (X)																		
	Freq (Hz)	**20**	**100**	**250**	**500**	**750**	**1k**	**5k**	**10k**	**15k**	**25k**	**50k**	**75k**	**100k**	**250k**	**500k**	**750k**	**1M**
BV/TV	R^2	0.50	0.39	0.03	0.00	0.00	0.00	0.03	0.06	0.11	0.25	0.58	0.69	0.71	0.67	0.63	0.60	0.59
	p	0.05	0.10	0.67	0.93	0.94	0.88	0.68	0.56	0.43	0.20	0.03	0.01	0.01	0.01	0.02	0.02	0.03
BMD	R^2	0.47	0.36	0.03	0.00	0.00	0.01	0.03	0.06	0.11	0.26	0.60	0.72	0.75	0.72	0.68	0.65	0.64
	p	0.06	0.11	0.70	0.95	0.93	0.87	0.66	0.55	0.41	0.19	0.02	0.01	0.01	0.01	0.01	0.02	0.02
Trab. Num.	R^2	0.63	0.49	0.11	0.03	0.01	0.00	0.00	0.01	0.02	0.11	0.35	0.46	0.49	0.47	0.43	0.41	0.40
	p	0.02	0.06	0.42	0.68	0.81	0.87	0.96	0.86	0.72	0.43	0.12	0.07	0.05	0.06	0.08	0.09	0.09
Trab. Thick.	R^2	0.01	0.02	0.09	0.09	0.10	0.10	0.22	0.32	0.41	0.57	0.76	0.77	0.75	0.70	0.69	0.69	0.69
	p	0.84	0.74	0.46	0.46	0.46	0.44	0.24	0.14	0.09	0.03	0.00	0.00	0.01	0.01	0.01	0.01	0.01
Trab. Sep.	R^2	0.64	0.42	0.11	0.03	0.01	0.00	0.00	0.00	0.01	0.06	0.21	0.28	0.30	0.31	0.28	0.27	0.27
	p	0.02	0.08	0.43	0.70	0.83	0.89	0.96	0.90	0.80	0.57	0.25	0.18	0.16	0.16	0.17	0.18	0.19

5.8 References

1. The Bone and Joint Initiative. Fracture Trends. *The Burden of Musculoskeletal Diseases in the United States* Available at: http://www.boneandjointburden.org/2014-report/via23/fracture-trends. (Accessed: 29th May 2018)

2. American Academy of Orthopaedic Surgeons. *The Burden of Musculoskeletal Diseases in the United States*. 1–8 (Bone and Joint Decade, 2008).

3. Morshed, S. Current Options for Determining Fracture Union. *Adv. Med.* **2014,** 1–12 (2014).

4. Bhandari, M., Fong, K., Sprague, S., Williams, D. & Petrisor, B. Variability in the Definition and Perceived Causes of Delayed Unions and Nonunions: A Cross-Sectional, Multinational Survey of Orthopaedic Surgeons. *JBJS* **94,** e109 (2012).

5. Corrales, L. A., Morshed, S., Bhandari, M. & Miclau, T. Variability in the Assessment of Fracture-Healing in Orthopaedic Trauma Studies. *J. Bone Joint Surg. Am.* **90,** 1862–1868 (2008).

6. Vannabouathong, C., Sprague, S. & Bhandari, M. Guidelines for fracture healing assessments in clinical trials. Part I: Definitions and endpoint committees. *Injury* **42,** 314–316 (2011).

7. Whiley, S. P. Evaluating fracture healing using digital x-ray image analysis. *Contin. Med. Educ.* **29,** 102 (2011).

8. Protopappas, V. C., Vavva, M. G., Fotiadis, D. I. & Malizos, K. N. Ultrasonic monitoring of bone fracture healing. *IEEE Trans. Ultrason. Ferroelectr. Freq. Control* **55,** 1243–1255 (2008).

9. Claes, L. E. & Heigele, C. A. Magnitudes of local stress and strain along bony surfaces predict the course and type of fracture healing. *J. Biomech.* **32,** 255–266 (1999).

10. Pountos, I., Georgouli, T., Pneumaticos, S. & Giannoudis, P. V. Fracture non-union: Can biomarkers predict outcome? *Injury* **44,** 1725–1732 (2013).

11. Bahney, C. S., Hu, D. P., Miclau, T. & Marcucio, R. S. The multifaceted role of the vasculature in endochondral fracture repair. *Bone Res.* **6,** 4 (2015).

12. Schindeler, A., McDonald, M. M., Bokko, P. & Little, D. G. Bone remodeling during fracture repair: The cellular picture. *Semin. Cell Dev. Biol.* **19,** 459–466 (2008).

13. Grundnes, O. & Reikerås, O. The importance of the hematoma for fracture healing in rats. *Acta Orthop. Scand.* **64,** 340–342 (1993).

14. Kolar, P. *et al.* The Early Fracture Hematoma and Its Potential Role in Fracture Healing. *Tissue Eng. Part B Rev.* **16,** 427–434 (2010).

15. Colnot, C. Skeletal Cell Fate Decisions Within Periosteum and Bone Marrow During Bone Regeneration. *J. Bone Miner. Res.* **24,** 274–282 (2009).

16. Ozaki, A., Tsunoda, M., Kinoshita, S. & Saura, R. Role of fracture hematoma and periosteum during fracture healing in rats: interaction of fracture hematoma and the periosteum in the initial step of the healing process. *J. Orthop. Sci.* **5,** 64–70 (2000).

17. Murao, H., Yamamoto, K., Matsuda, S. & Akiyama, H. Periosteal cells are a major source of soft callus in bone fracture. *J. Bone Miner. Metab.* **31,** 390–398 (2013).

18. Hu, D. P. *et al.* Cartilage to bone transformation during fracture healing is coordinated by the invading vasculature and induction of the core pluripotency genes. *Development* **144,** 221–234 (2017).

19. Wong, S. A. *et al.* Microenvironmental Regulation of Chondrocyte Plasticity in Endochondral Repair—A New Frontier for Developmental Engineering. *Front. Bioeng. Biotechnol.* **6,** (2018).

20. Fyhrie, D. P. *et al.* Effect of Fatiguing Exercise on Longitudinal Bone Strain as Related to Stress Fracture in Humans. *Ann. Biomed. Eng.* **26,** 660–665 (1998).

21. Borchani, W., Aono, K., Lajnef, N. & Chakrabartty, S. Monitoring of Postoperative Bone Healing Using Smart Trauma-Fixation Device With Integrated Self-Powered Piezo-Floating-Gate Sensors. *IEEE Trans. Biomed. Eng.* **63,** 1463–1472 (2016).

22. Kell, D. B., Markx, G. H., Davey, C. L. & Todd, R. W. Real-time monitoring of cellular biomass: Methods and applications. *TrAC Trends Anal. Chem.* **9,** 190–194 (1990).

23. Patel, P. & Markx, G. H. Dielectric measurement of cell death. *Enzyme Microb. Technol.* **43,** 463–470 (2008).

24. McGilvray, K. C. *et al.* Implantable microelectromechanical sensors for diagnostic monitoring and post-surgical prediction of bone fracture healing. *J. Orthop. Res.* **33,** 1439–1446 (2015).

25. Markx, G. H. & Davey, C. L. The dielectric properties of biological cells at radiofrequencies: applications in biotechnology. *Enzyme Microb. Technol.* **25,** 161–171 (1999).

26. S. Grimnes & O.G. Martinsen. *Bioimpedance and Bioelectricity Basics*. (Elsevier, 2015). doi:10.1016/C2012-0-06951-7

27. Rigaud, B., Morucci, J. P. & Chauveau, N. Bioelectrical impedance techniques in medicine. Part I: Bioimpedance measurement. Second section: impedance spectrometry. *Crit. Rev. Biomed. Eng.* **24,** 257–351 (1996).

28. Dean, D. A., Ramanathan, T., Machado, D. & Sundararajan, R. Electrical impedance spectroscopy study of biological tissues. *J. Electrost.* **66,** 165–177 (2008).

29. Stoy, R. D., Foster, K. R. & Schwan, H. P. Dielectric properties of mammalian tissues from 0.1 to 100 MHz; a summary of recent data. *Phys. Med. Biol.* **27,** 501 (1982).

30. Jongschaap, H., Wytch, R., Hutchison, J. & Kulkarni, V. Electrical impedance tomography: a review of current literature. *Eur. J. Radiol.* **18,** 165–174 (1994).

31. Gabriel, S., Lau, R. & Gabriel, C. The dielectric properties of biological tissues: II. Measurements in the frequency range 10 Hz to 20 GHz. *Phys Med Biol* **41,** 2251–2269 (1996).

32. Bonifasi-Lista, C. & Cherkaev, E. Electrical impedance spectroscopy as a potential tool for recovering bone porosity. *Phys. Med. Biol.* **54,** 3063–3082 (2009).

33. Ciuchi, I., Curecheriu, L., Ciomaga, C., Sacdu, A. & Mitoseriu, L. Impedance Spectroscopy characterization of bone tissues. *J. Adv. Res. Phys.* **1,** (2010).

34. Schaur, S., Jakoby, B. & Kronreif, G. Position-dependent characterization of bone tissue with electrical impedance spectroscopy. in *Position-dependent characterization of bone tissue with electrical impedance spectroscopy* (IEEE Sensors, 2012).

35. Lin, M. C., Herfat, S. T., Bahney, C. S., Marmor, M. & Maharbiz, M. M. Impedance spectroscopy to monitor fracture healing. in *IEEE Engineering in Medicine and Biology Conference*. 5138–5141 (2015).

36. Lin, M. C. *et al.* New opportunities for fracture healing detection: Impedance spectroscopy measurements correlate to tissue composition in fractures. *J. Orthop. Res.* **35,** 2620–2629

37. Hirashima, T., Kim, W. C., Kawamoto, K., Yoshida, T. & Kubo, T. Evaluating Bone Union of Distal Radius Fractures by Measuring Impedance Values. *Orthopedics* **32,** 31–33 (2009).

38. Yamada, N. *et al.* Analysis of increase in bone electrical impedance in fracture healing. in (55th Annual Meeting of the Orthopaedic Research Society, 2009).

39. Yoshida, T., Kim, W. C., Oka, Y., Yamada, N. & Kubo, T. Assessment of distraction callus in rabbits by monitoring of the electrical impedance of bone. *Acta Orthop.* **81,** 628–633 (2010).

40. Kumaravel, S. & Sundaram, S. Monitoring of fracture healing by electrical conduction: A new diagnostic procedure. *Indian J. Orthop.* **46,** 384 (2012).

41. Kozhevnikov, E. *et al.* Electrical impedance spectroscopy – a potential method for the study and monitoring of a bone critical-size defect healing process treated with bone tissue engineering and regenerative medicine approaches. *J Mater Chem B* **4,** 2757–2767 (2016).

42. Gupta, K. *et al.* Changes in electrical properties of bones as a diagnostic tool for measurement of fracture healing. *Hard Tissue* **2,** 3 (2013).

43. Kamran Zamanian & Dylan Freeze. *US Orthopedic Trauma Device Market To Exceed 8 Billion By 2020*. (iData Research).

44. Kilkenny, C., Browne, W. J., Cuthill, I. C., Emerson, M. & Altman, D. G. Improving Bioscience Research Reporting: The ARRIVE Guidelines for Reporting Animal Research. *PLOS Biol* **8,** e1000412 (2010).

45. Bonnarens, F. & Einhorn, T. A. Production of a standard closed fracture in laboratory animal bone. *J. Orthop. Res.* **2,** 97–101 (1984).

46. Auer, J. A. *et al.* Refining animal models in fracture research: seeking consensus in optimising both animal welfare and scientific validity for appropriate biomedical use. *BMC Musculoskelet. Disord.* **8,** 72 (2007).

47. Thompson, Z., Miclau, T., Hu, D. & Helms, J. A. A model for intramembranous ossification during fracture healing. *J. Orthop. Res.* **20,** 1091–1098 (2002).

48. Matthys, R. & Perren, S. M. Internal fixator for use in the mouse. *Injury* **40,** S103–S109 (2009).

49. Steck, R. *et al.* Influence of internal fixator flexibility on murine fracture healing as characterized by mechanical testing and microCT imaging. *J. Orthop. Res.* **29,** 1245–1250

50. Litrenta, J. *et al.* Determination of Radiographic Healing: An Assessment of Consistency Using RUST and Modified RUST in Metadiaphyseal Fractures. *J. Orthop. Trauma* **29,** 516–520 (2015).

51. Fox, W. C. & Miller, M. A. Osseous implant for studies of biomaterials using an in vivo electrochemical transducer. *J. Biomed. Mater. Res.* **27,** 763–773

52. Bahney, C. S. *et al.* Stem Cell–Derived Endochondral Cartilage Stimulates Bone Healing by Tissue Transformation. *J. Bone Miner. Res.* **29,** 1269–1282

53. Yu, Y., Bahney, C., Hu, D., Marcucio, R. S. & Miclau, T. Creating rigidly stabilized fractures for assessing intramembranous ossification, distraction osteogenesis, or healing of critical sized defects. *J. Vis. Exp. JoVE* (2012). doi:10.3791/3552

54. Le, A. X., Miclau, T., Hu, D. & Helms, J. A. Molecular aspects of healing in stabilized and non-stabilized fractures. *J. Orthop. Res.* **19,** 78–84

55. Lin, M. C. *et al.* Using impedance to track fracture healing rates in mice in vivo: A pilot study. in *IEEE Engineering in Medicine and Biology Conference.* 1724–1727. (2017) doi:10.1109/EMBC.2017.8037175

Chapter 6: Conclusions

With smart medical devices on the rise, patients and physicians alike are being empowered to approach healthcare decisions with more quantitative data. New sensing modalities and platforms are providing low-cost vital signs monitoring even outside of the hospital. In addition, new assessment tools can enable more efficient management of clinical trial patients and increase retention by reducing clinic visits. Continuous monitoring has the potential to provide accurate, objective feedback on clinically-relevant concerns such as disease progression and intervention efficacy. This thesis discussed the use of impedance spectroscopy in healthcare, as direct electrical measurements have a number of clinical applications and can offer advantages over traditional physical monitoring methods.

Chapters 2 and 3 discussed the development of an impedance measurement system for monitoring surface wounds, using a flexible electrode array to map out areas of the skin. This work involved taking EIS measurements across an array to detect and monitor pressure ulcers in a rat model and reported the early findings of a clinical trial. Other applications in excisional wounds were also briefly explored, which could extend to diagnosis and tracking of injuries including lacerations or burns. This array was also adapted for use as a non-invasive device to diagnose a parasitic disease in Cameroon. Point-of-care diagnostics are incredibly critical for developing nations, and the miniaturization of electronics and portability of this system lends itself to these kinds of applications.

Chapters 4 and 5 covered research utilizing the same impedance spectroscopy technology but instead applying it below the surface, specifically to monitor bone fractures. EIS measurements were first shown to differentiate between individual tissues dominant in the fracture healing process, and further demonstrated to correlate with tissue composition of heterogeneous fracture

calli. This was then optimized for an *in vivo* model, miniaturizing the electrodes and sensing system for implantation in mice. This work showed that impedance can be integrated into existing fracture fixation techniques including external fixation using an external fixator as well as internal fixation using a bone plate.

Taken together, these results established the feasibility of EIS to directly track a number of clinical conditions. Future work to optimize ease-of-use for clinicians as well as improve portability by incorporating wireless data transfer can continue to move this technology towards commercialization and eventually use in healthcare settings. These smart sensors and instrumented implants can provide physicians with additional quantitative information at much higher temporal resolution than currently available and offer more objective data to guide clinical decisions for patients.

Publishing Agreement

It is the policy of the University to encourage the distribution of all theses, dissertations, and manuscripts. Copies of all UCSF theses, dissertations, and manuscripts will be routed to the library via the Graduate Division. The library will make all theses, dissertations, and manuscripts accessible to the public and will preserve these to the best of their abilities, in perpetuity.

Please sign the following statement:

I hereby grant permission to the Graduate Division of the University of California, San Francisco to release copies of my thesis, dissertation, or manuscript to the Campus Library to provide access and preservation, in whole or in part, in perpetuity.

Monica Lin

Author Signature

10/04/2018

Date